Wavelet Analysis of the Arrival Directions of Ultra High Energy Cosmic Rays at the Pierre Auger Observatory

von

Matthias Plum

Diplomarbeit in Physik

vorgelegt der
Fakultät für Mathematik, Informatik und Naturwissenschaften
der
Rheinisch-Westfälischen Technischen Hochschule Aachen

im Oktober des Jahres 2011

angefertigt am

III. Physikalischen Institut A

Erstgutachter und Betreuer

Prof. Dr. Thomas Hebbeker
III. Physikalisches Institut A
RWTH Aachen

Zweitgutachter

Prof. Dr. Martin Erdmann
III. Physikalisches Institut A
RWTH Aachen

Contents

1 Introduction **1**

2 Cosmic rays **3**

2.1 Energy spectrum 3

2.2 Origin of cosmic rays 4

2.2.1 Acceleration 4

2.2.2 Anisotropy 6

2.3 Cosmic ray induced extensive air showers 7

2.3.1 Hadronic component 7

2.3.2 Electromagnetic component 8

2.3.3 Muonic component 8

2.3.4 Neutrino component 8

3 The Pierre Auger Observatory **9**

3.1 Detector 9

3.1.1 Surface detector 9

3.1.2 Fluorescence detector 13

3.1.3 Enhancements 13

4 Wavelet analysis **15**

4.1 Introduction of wavelets 15

4.2 1-dim analysis 15

4.3 Spherical analysis 17

4.3.1 Multipole expansion 18

4.3.2 Healpix software 18

4.4 Wavelet shape 19

4.4.1 Needlet 19

4.4.2 Needlet and Healpix parameters 23

5 Study of UHECRs arrival direction on simulated data samples with the needlet analysis 25

5.1 Monte Carlo simulation on an ideal detector 25

5.1.1 Power estimation 27

5.1.2 Threshold method 29

5.1.3 Significance test 32

5.1.4 Comparison of needlet analysis to a multipole analysis 34

5.2 Anisotropy search in Monte Carlo data 36

5.2.1 Auger exposure 36

5.2.2 Large scale structures test 37

5.2.3 Point source test 44

6 Applying the anisotropy study on the arrival directions of UHECRs measured by the Pierre Auger Observatory 51

6.1 Local effects 51

6.1.1 Atmospheric condition correction 51

6.1.2 Geomagnetic field effect 52

6.1.3 Data selection 54

6.2 Applying the needlet analysis on the data taken by the Pierre Auger Observatory 55

6.2.1 Data sample with uncorrected energy estimator 55

6.2.2 Data sample with corrected energy estimator 60

6.2.3 Data sample with corrected energy estimator and an additional minimal energy cut of 10 EeV 65

7 Summary and outlook 69

A Appendix 71

A.1 List of abbreviations 71

A.2 Needlet kernel function 72

References 75

List of figures 81

List of tables 83

Acknowledgements 85

1. Introduction

Cosmic rays have been the subject of scientific investigation for about one century. Great progress was made by physicists around the world in understanding the universe and the processes on astronomical scale, like the measurement of the predicted cosmic microwave background. Astroparticle physics in the highest energy range is a great opportunity to investigate the fundamental questions about the universe.
The interactions of cosmic rays with the atmosphere induce particle cascades, which can be measured by ground based detectors. These secondary particle cascades can be used to determine the arrival direction and the energy of the primary cosmic ray particle. The largest earthbound cosmic ray detector is the Pierre Auger Observatory in Argentina.
The acceleration of cosmic rays to ultra high energy is not fully understand, but their are known possible source candidates. Due to the fact, that charged cosmic rays are deflected by the galactic and the extragalactic magnetic field, their arrival directions are for the most part distributed isotropically. However, particles with ultra high energy are less deflected by magnetic fields and could still point back to their sources. It is of great interest to identify sources of ultra high energy cosmic rays.
The wavelet analysis is a filter method invented in the 1980s to amplify local structures and signals in geophysics. Today there are many applications of wavelets in a various kinds of research topics, like medicine, data compression, geophysics and meteorology. In the last few years the spherical wavelet analysis became more popular in analyzing astrophysical data, e.g. in anisotropy studies of the cosmic microwave background.
In this thesis a spherical wavelet analysis is performed with the 'needlet' wavelet on an event based data set of the arrival direction of ultra high energy cosmic rays measured by the Pierre Auger Observatory. The needlet analysis is presented and their performance is shown in Monte Carlo simulations on various scenarios. The goal is to determine if there are regions in the sky where ultra high energy cosmic rays are distributed anisotropically. The data sample is corrected for local effects, which might induce a false anisotropic signal. The final result will be tested for compability with an isotropic scenario to determine the significance of the result.

2. Cosmic rays

Victor Hess studied the changes of ionizing radiation in the atmosphere with balloon flights in 1912. He measured that the ionization rate in the atmosphere is decreasing up to an altitude of 1 km above the ground. However, above 1 km the ionization rate is increasing with higher altitude. He expected the decreasing of the ionization rate, because it was believed, that the ionization was caused by natural radioactivity from decays of unstable isotopes inside the Earth [Hes12]. The measurement was a clear evidence that there are sources of ionizing radiation outside the Earth's atmosphere. He postulated that there are cosmic rays hitting the atmosphere and cause the increase of the ionization rate.
In 1938 Pierre Victor Auger measured cosmic rays in coincidence at distant locations in the swiss alps at a height of about 3500 m and deducted the existence of extended cosmic ray showers, that are caused by the interaction of a primary cosmic ray particle with a nucleus of the atmosphere [AEM+39].
Today it is known that the atmosphere of the earth is continuously hit by cosmic rays. The energy and the composition of these cosmic rays for low energies were measured since the beginning of the last century in various experiments.
The charged part of these particles consist to 98% of ionized nuclei, which consist of 87% protons, 12% helium and 1% heavier nuclei [Lon11]. The remaining 2% of charged cosmic rays consists of electrons. The neutral part of these incoming particles consists of neutrinos, photons and neutrons. The range of neutrons is at energies of about EeV great enough to reach the Earth before decaying [MTKM07].

2.1 Energy spectrum

The measured energy spectrum of the cosmic rays on earth can be described as the particle flux I depending on the energy E:

$$\frac{dI}{dE} \propto E^{-\gamma}\,, \tag{2.1}$$

where γ is the spectral index of the energy spectrum. The spectral index in the low energy part starting from 10^{11} eV is measured to be 2.7. At energies of about $3 \cdot 10^{15}$ eV the spectral index γ changes to 3.1, which is often being referred to as the 'knee' of the spectrum. The flux of cosmic rays at this point is around 1 particle/m^2/year. At energies around $3 \cdot 10^{18}$ eV the spectral index changes back to a value of 2.6. This point of discontinuity of the energy spectrum is often being referred to as the 'ankle', where the flux has decreased to 1 particle/km^2/year (for

details see [BEH09]). For energies above $6 \cdot 10^{19}$ eV Greisen, Zatsepin and Kuzmin predicted a cut-off of the cosmic ray flux (GZK cut-off). At this energy, primary particles start interacting with the photons of the cosmic microwave background (CMB), so the particle flux decreases rapidly [AP08]. At energies of about 10^{20} eV the flux falls to a value of 1 particle/km^2/century.
The 'knee' and the 'ankle' can be a hint of changes of the acceleration mechanisms at the sources, an effect of cosmic ray propagation or an energy dependent change in the hadronic composition [BEH09]. The energy spectrum measured by various experiments is shown in figure 2.1. The altitude of interaction of primary cosmic rays with the atmosphere is typically in a height of 20 km. Direct measurements with satellite born and balloon experiments are limited to primary energies up to 10^{15} eV, due to the limitation of the detector size. Alternatively, secondary particles can be measured in ground experiments, that yield information on the primary particle. Therefore, huge detection areas on the surface of the Earth allow access to energies up to 10^{21} eV.

2.2 Origin of cosmic rays

The origin of ultra high energy cosmic rays (UHECR) is still an unsolved mystery. However, there are several theories how the acceleration of the particles to that great energies can take place.

2.2.1 Acceleration

The first order Fermi acceleration or shock acceleration assumes, that particles are accelerated in shock waves of supernovae remnants. A particle flying through the shock front will, in the particle rest frame, experiences all magnetic disturbances moving towards it. Therefore, any scattering the particle undergoes will be a head-on collision. Particles can pass through the shock front for multiple times, while it gets every time another energy gain. The energy gain by this acceleration can be calculated as

$$\Delta E \propto \beta_s \,, \tag{2.2}$$

where β_s is the shock front velocity. The maximal acceleration energy by diffuse shock acceleration of supernovae remnants [BEH09] can be estimated as

$$E_{max} \cong 10^{18}\,\mathrm{eV} \cdot Z \cdot \beta_s \left(\frac{R}{\mathrm{kpc}}\right)\left(\frac{B}{\mu\mathrm{G}}\right) , \tag{2.3}$$

where E_{max} is the maximum energy of the particle, Z the charge of the cosmic ray, R the size of the source region in kpc (1pc $= 30.856776 \cdot 10^{15}$m) and B the magnetic field strength at the source in μG. This relation is shown in figure 2.2.
In the second order Fermi acceleration the particles can be gradually accelerated by a series of elastic scatterings in moving interstellar clouds [Fer49]. In that scenario a particle can have head-on collisions with a magnetic irregularity(hot gas cloud) moving towards it. The energy gain by this acceleration is

$$\Delta E \propto \beta^2 \,, \tag{2.4}$$

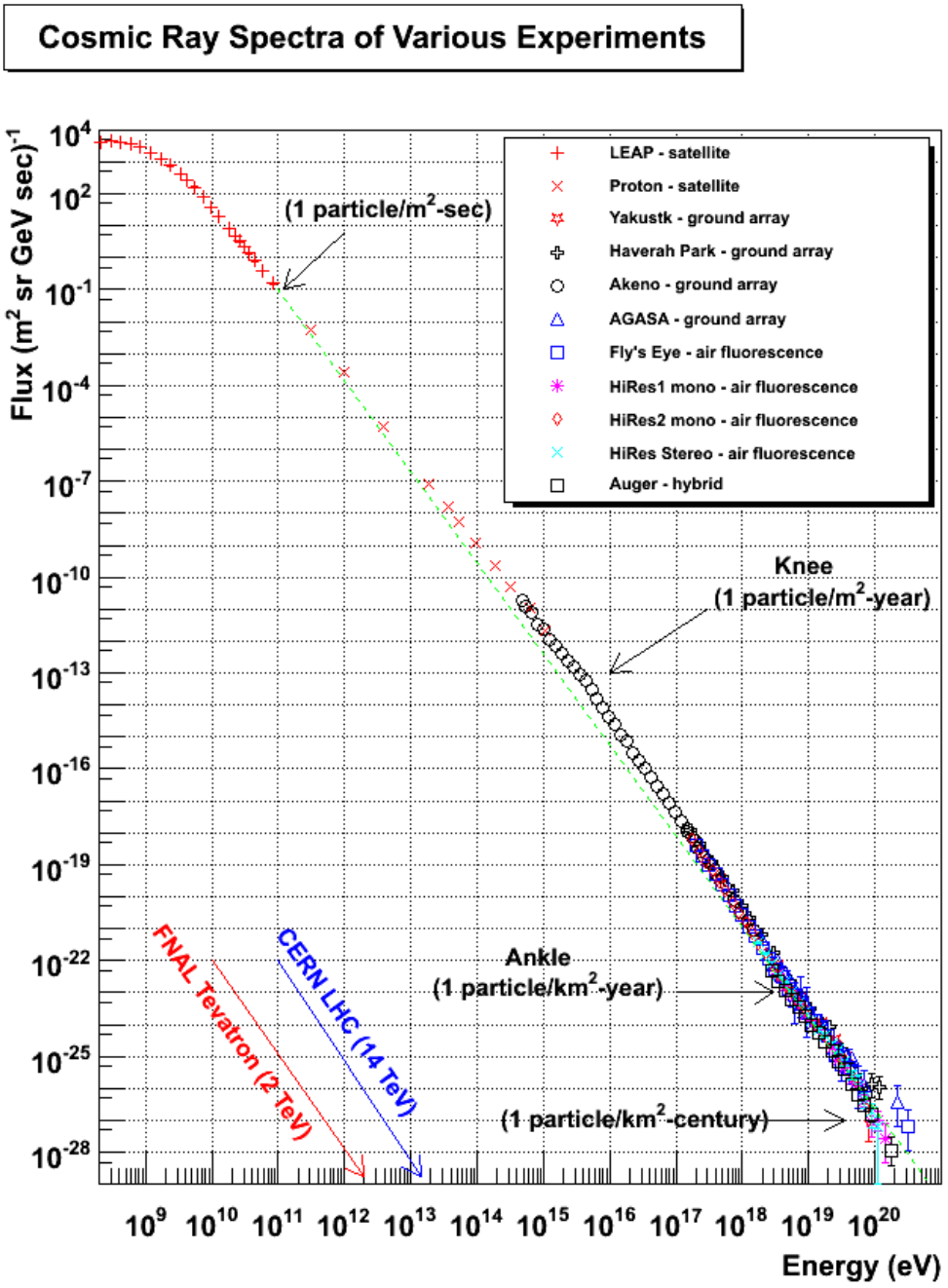

Figure 2.1: Cosmic ray energy spectrum measured by various experiments [Han]. The flux of the cosmic rays against the energy of the particles shows the power law behavior of the spectrum. The positions of the features 'knee' and 'ankle' are shown. At these points the value of the power law index changes.

where β is the velocity of the cloud. This acceleration can lead to a power law energy spectrum. However, the energy gain is small and the process is inefficient. First order Fermi acceleration in supernovae shock fronts leads to a power law with spectral index of 2 [RBRD08]. Above that energy theory predicts, that relativistic

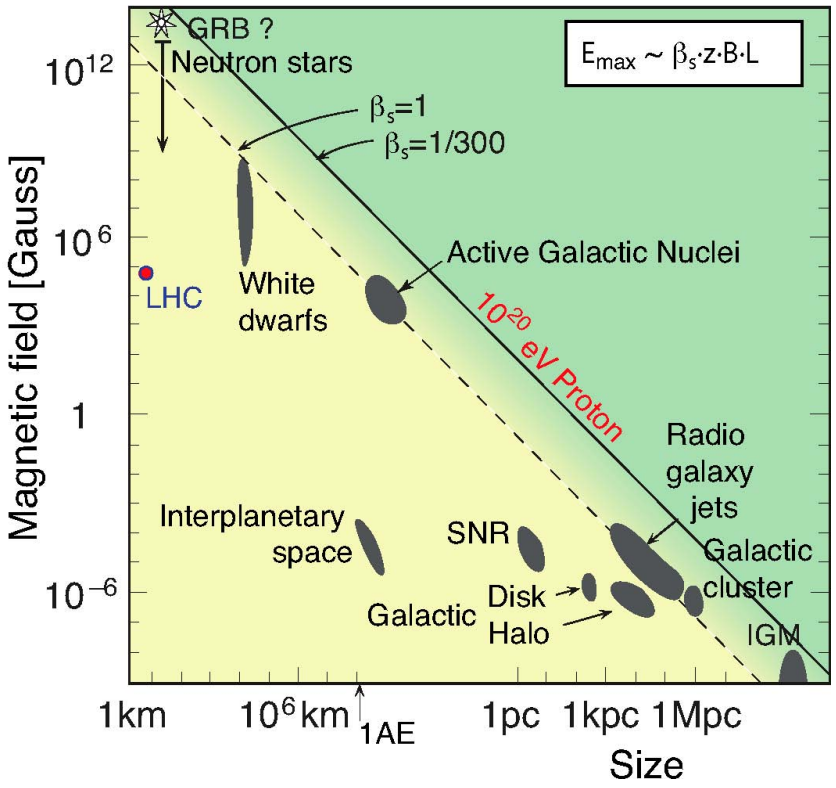

Figure 2.2: Hillas Plot of astrophysical objects in which cosmic rays could be accelerated [Lab]. The magnetic field strength against the size of the source region is shown.

jets of a supermassive black hole in active galactic nuclei (AGN) or gamma ray bursts (GRB) can accelerate cosmic rays up to energies of about 10^{19} eV. Cosmic rays with higher energy can be accelerated in accretion-shock waves of black holes or be the decay product of dark matter annihilation. So the acceleration process is not entirely understood and still in focus of current investigations.

2.2.2 Anisotropy

The arrival directions of UHECRs seem to be isotropic distributed. As most particles of the cosmic rays are charged, they are deflected by galactic and extragalactic magnetic fields. The simplest description of deflection can be described as the Lamour radius r_L [BEH09], which is given by

$$r_L = 1.08\,\mathrm{pc}\frac{E/\mathrm{PeV}}{Z \cdot (B/\mu\mathrm{G})}\,, \tag{2.5}$$

where Z is the charge of the cosmic ray, E the energy of the particle and B the magnetic field strength in μG . Therefore, the directional information originally carried by the particles may be lost. This also depends on the distance of the source as well as the strength and topology of the magnetic fields the cosmic ray is exposed to. However, the magnetic deflection is energy dependent, so the highest UHECRs should still point backward to their source regions. Unfortunately, only little is

known about the topology of the magnetic field in the extragalactic and galactic fields. The Auger collaboration has measured that there is a hint for a correlation of the highest measured events with known AGNs [ASP07].

2.3 Cosmic ray induced extensive air showers

A cosmic ray particle hits the atmosphere of the Earth and reacts in most cases with a nucleus of a nitrogen or oxygen atom of the atmosphere. This first interaction forms a multitude of secondary particles, which themselves interact with atmospheric components and initiate a cascade. Therefore, it is necessary to investigate and understand the properties of extensive air showers (EASs). EASs consist of a hadronic, an electromagnetic, a muonic and a neutrino component. A scheme of this cascade with its components is shown in the left side in figure 2.3.

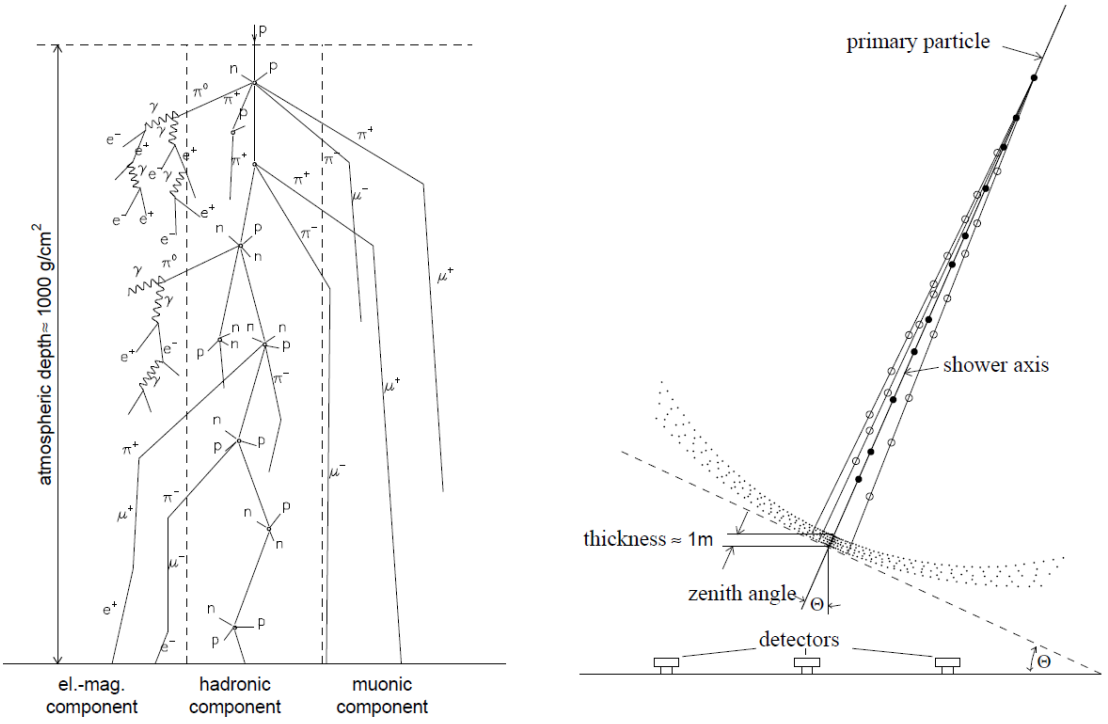

Figure 2.3: Left: Schematic view of the extensive air shower components. Right: Geometrical shape of an extensive air shower [All75].

Depending on the energy and the type of the primary particle the air shower particles form a disc with a thickness of a few meters, which is shown in the right side in figure 2.3. The lateral diameter of an EAS can reach up to some kilometers.

2.3.1 Hadronic component

A hadronic particle colliding with an atmospheric nuclei initiates a hadronic cascade via inelastic scattering. This hadronic cascade produces secondary particles. Most

likely this secondary particles consist of pions, kaons, protons and neutrons. Charged pions, protons and neutrons are subject to further hadronic interaction. Charged pions decay into muons and neutrinos, whereas the neutral pion decays into two photons, which can start an electromagnetic cascade.

2.3.2 Electromagnetic component

The electromagnetic component of an air shower is most likely induced by the decay of a neutral pion into two photons. These photons produce e^+e^--pairs that create more photons by bremsstrahlung. This photons can also start to produce e^+e^--pairs. Therefore, an electromagnetic cascade is created until the energy of the secondary particles is not sufficient for pair production. The electromagnetic cascade can also be initiated by a primary photon, electron or positron. The photo-electric effect, the Compton effect and the ionization effect of electromagnetic particles can be neglected with respect to the high energies necessary for the cascade development [RS98].

2.3.3 Muonic component

The main part of the secondary particles that reach the surface of the Earth consists of muons. Muons are created by decaying pions and kaons. The main production channels are shown in table 2.1. Due to the less deflection in the atmosphere compared to electrons, muons spread only little and allow to reconstruct the arrival direction of the primary particle. This is very valuable for ground based detector arrays.

$$\begin{array}{ll} \pi^+ & \rightarrow \mu^+ + \nu_\mu \\ \pi^- & \rightarrow \mu^- + \bar{\nu}_\mu \\ K^+ & \rightarrow \mu^+ + \nu_\mu \\ K^- & \rightarrow \mu^- + \bar{\nu}_\mu \\ K^\pm & \rightarrow \pi^\pm + \pi_0 \end{array}$$

Table 2.1: Muon production and decay of charged mesons.

2.3.4 Neutrino component

In an air shower neutrinos are produced by the decay of muons and pions (see table 2.1). They play an inferior role in EAS measurement, due to their very low interaction cross section, thus providing only small statistics. However, the neutrino as primary cosmic ray conserves its directional information, because it is not affected by magnetic fields. Therefore, observing a primary neutrino is of great value for astrophysics.

3. The Pierre Auger Observatory

The Pierre Auger Observatory is located in the Pampa Amarilla, near Malargüe in the province of Mendoza, Argentina. It is an air shower experiment dedicated to the measurement of extensive air showers as being initiated by ultra high energy cosmic rays. The detector is sensitive to particles with energies ranging from 10^{18} eV to 10^{21} eV.

3.1 Detector

The Pierre Auger Observatory is a hybrid detector, which means that it consist of two detector components. A surface detector array over an area of 3000 km^2 and four fluorescence detector buildings constructed around the array. The hybrid approach is the detection of the same particle at ground and the observation of associated fluorescence light generated in the atmosphere above the ground. Figure 3.1 shows the detector array and the telescope stations.

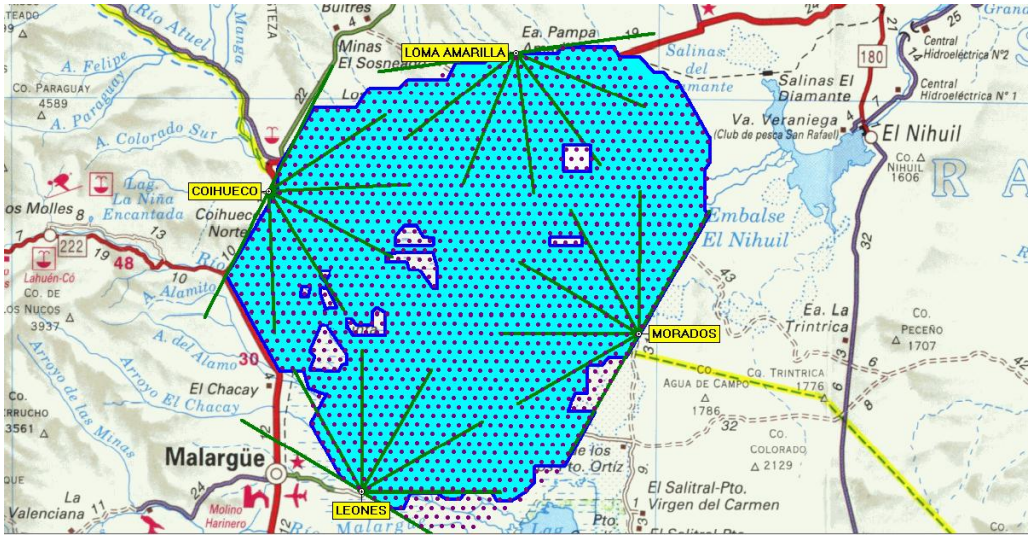

Figure 3.1: The Pierre Auger Observatory[Piea]. The picture shows the surface detector array (small dots) over an area of 3000 km^2 and four fluorescence detector buildings located around the array.

3.1.1 Surface detector

The 'Surface Detector' (SD) consists of 1600 water Cherenkov detector stations, which are uniformly distributed on a hexagonal grid with a pitch of 1500 m. Each

station is powered by a solar panel and a battery system and the data is transferred via a wireless communication system(shown in figure 3.2). Each station is filled with 10 tons of pure water and equipped with three photomultiplier tubes (PMTs). The inner surface of the station is encased with a reflecting layer called Tyvek. The time information for the PMT signals is provided by a GPS receiver. In figure 3.3 an

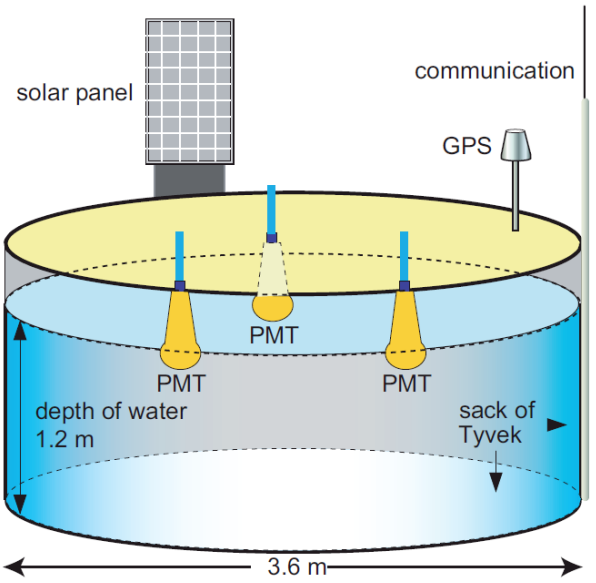

Figure 3.2: Scheme of a SD station [Dem09]. The power is provided by a solar panel and a battery system. The data is transferred via a wireless communication system. Each station is filled with 10 tons of pure water and equipped with three PMTs. The inner surface of the station is encased with a reflecting layer called Tyvek. The time information for the PMT signals is provided by a GPS receiver.

example for one SD station is shown. The SD stations are mostly sensitive to the muonic components of an EAS. One advantage of the SD is, that the array achieves an uptime of nearly 100%. The trigger efficiency above an energy of $E \geq 3\,\mathrm{EeV}$ for the typical zenith angle cut $\theta > \theta_{max} = 60°$ is close to 100%. In figure 3.4 a typical SD event is shown. In the simplest case of shower direction reconstruction, the shower front can be assumed as plane with a flat SD array and a particle velocity close to the speed of light (see figure 3.5). The time difference Δt_i between the measured arrival time t_i at station i and the expected arrival time considering the distance of the station from the shower core can be written as

$$\Delta t_i = t_i - \left(T_0 - \frac{u(x_i - x_{core}) + v(y_i - y_{core})}{c} \right) , \tag{3.1}$$

where T_0 is the arrival time of the shower core at ground and $u = sin\theta\, cos\phi$ and $v = sin\theta\, sin\phi$ are the direction (co-)sines. x_i and y_i denote the coordinates of the station i. The coordinates of the shower core position are x_{core} and y_{core}. The angles are the local coordinates zenith θ and azimuth ϕ. The shower core position is determined by the barycenter of all triggered stations, weighted by the square root

Figure 3.3: Picture of a surface detector station [Plu].

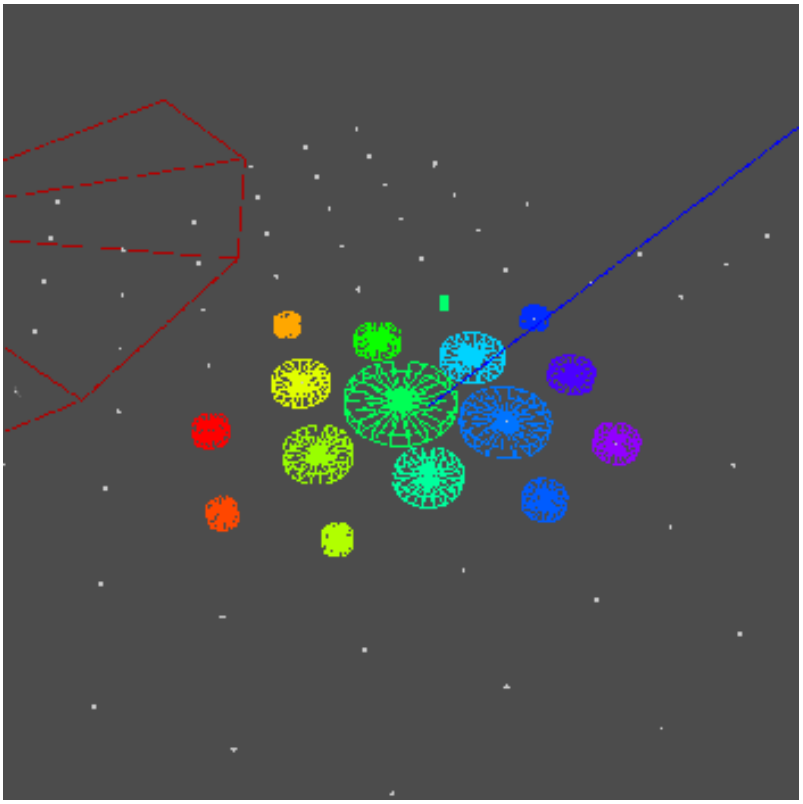

Figure 3.4: Event display of a SD event, where the color code contains the timing information and the size of the station corresponds to the PMT signal strength [Pieb].

of each station signal [PP03]. With this informations, the angles can be extracted

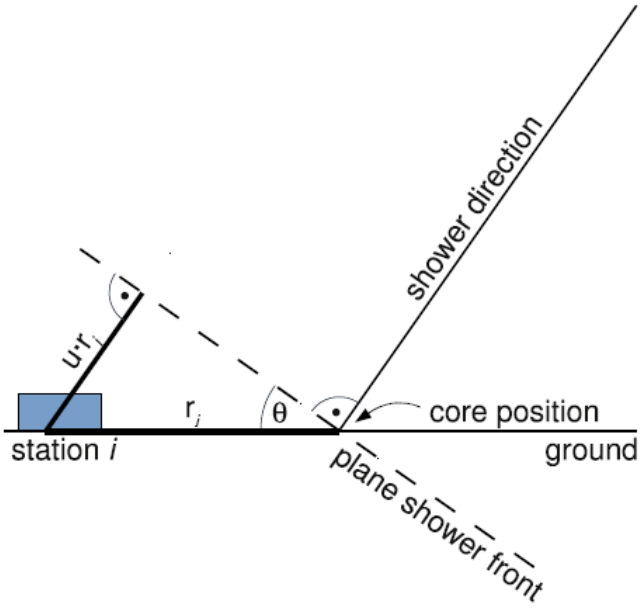

Figure 3.5: Schematic of the angular reconstruction of SD assuming a plane shower front [Gri11].

from equation 3.1, by minimization of

$$\chi^2 = \sum_i \frac{(\Delta t_i)^2}{\sigma_{t_i}^2}\,, \tag{3.2}$$

where $\sigma_{t_i}^2$ is the uncertainty of the measured arrival time t_i at station i.In this way the shower direction of an air shower can be reconstructed with a resolution of $\approx 1°$.

The uncertainties of shower to shower fluctuations of the shower energy estimator can be minimized if a characteristic signal is measured at a shower core distance of $\geq 500\,\mathrm{m}$ [HMHH71]. The optimum distance for the SD shower energy estimator of the Pierre Auger Observatory with a distance of 1500 m between the stations has been found to be at $\approx 1000\,\mathrm{m}$, which is called the $S(1000)$ value [DNW05]. The signal strength in the individual stations and their distances to the shower core are used to fit the value of $S(1000)$ with the following equation

$$S(r) = S(1000)\left(\frac{r}{1000\,\mathrm{m}}\right)^{\beta}\left(1+\frac{r}{1000\,\mathrm{m}}\right)^{\beta}\,. \tag{3.3}$$

$S(r)$ is the signal measured in a SD station at a shower core distance r with the parameter β(see [DNW05]). The energy measurement of SD events is cross calibrated with a calorimetric fluorescence light measurement of the fluorescence detector, for details see [Gri11].

3.1.2 Fluorescence detector

The 'Fluorescence Detector' (FD) consists of four telescope buildings each with 6 telescopes to cover the sky above the surface detector array. The FD telescopes measure the ultraviolet fluorescence light emitted by an air shower and can measure the shower development in the atmosphere. A scheme of a FD telescope is shown in figure 3.6. The light track of an air shower is measured with a PMT camera, that consists of 440 pixels located on the focal surface of the telescope mirrors [AP10]. The FD measurement is a calorimetric measurement of the energy by recording the

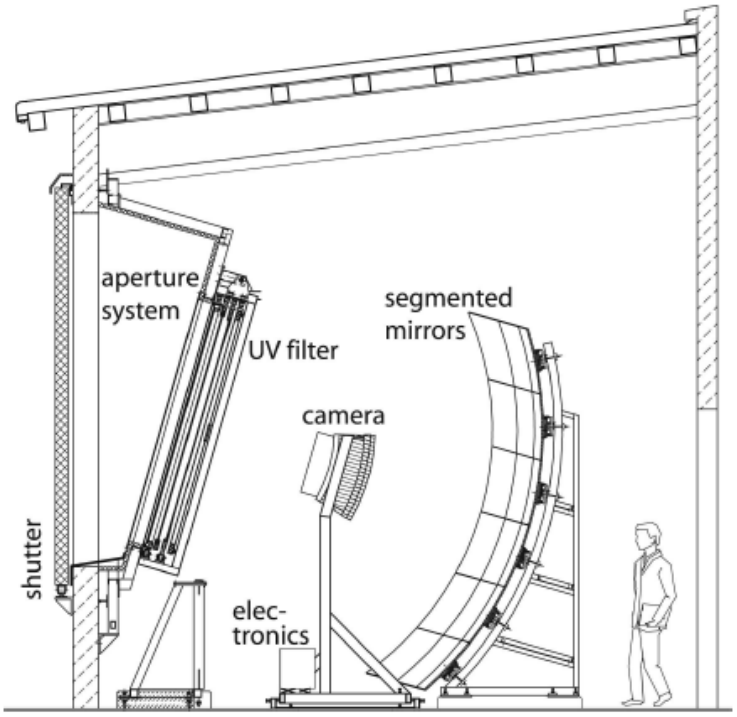

Figure 3.6: Schema of the fluorescence detector [AP10]

the amount of produced light. Due to the small amount of light of an air shower, the FD telescopes can only measure EAS in moonless clear nights, which is limiting the duty cycle to around 13%. The reconstructed shower direction has a resolution of 0.6° (for details see [AP10]). In figure 3.7 an event display of an EAS is shown. This event is seen by all four telescope stations and has also a SD reconstruction. It is a good example for the hybrid detection of cosmic rays.

3.1.3 Enhancements

In the last few years the Pierre Auger Observatory was expanded with three further detector components to measure cosmic rays.
One of this enhancements are the 'High Elevated Auger Telescopes' (HEAT). HEAT is located at the Coihueco telescope site and consists of three Auger telescopes, that

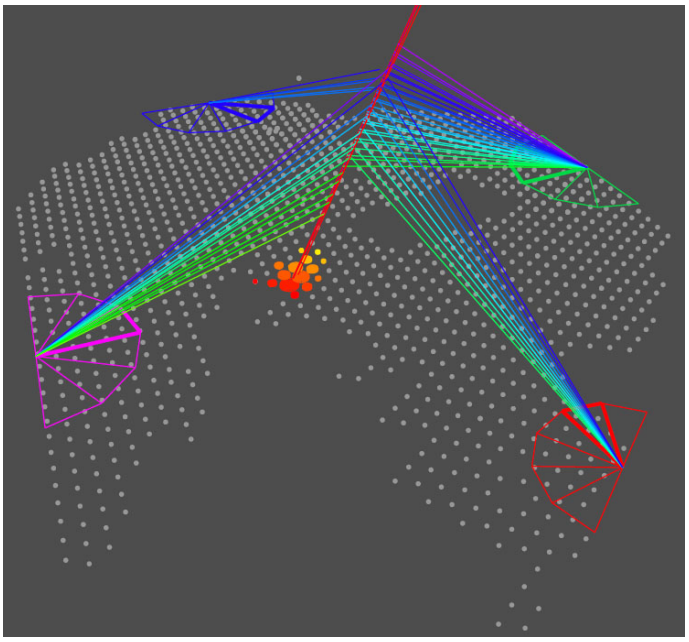

Figure 3.7: A multi fluorescence detector event, seen by all four FD telescopes and SD reconstruction [Piec].

are 30° tilted upward in comparison to the standard Auger telescopes. These telescopes can measure low energy air showers in close distance. It expands the lower energy range of the Pierre Auger Observatory to an energy of around 10^{17} eV.
As a further extension the 'Auger Muon detectors and Infill for the Ground Array' (AMIGA) is also located close to the Coihueco site. In a limited region within the regular grid stations additional SD stations are deployed with a smaller spacing of 750 m and partly even 433 m. The infill array should provide the basis for air shower detections at lower energy. The second part of AMIGA consist of muon detectors, that are buried close to selected SD stations. The increased attenuation in the earth shields the electromagnetic component of the air shower and so only the muonic component is measured. This measurement is expected to provide an improved understanding of the different components in the lateral distribution of the secondary particles of air showers.
Another extension for the Pierre Auger Observatory is the 'Auger Engineering Radio Array' (AERA). Air showers also produce a radio signals, which are caused by synchrotron radiation, while the secondary particles propagates through the magnetic field of the Earth. The goal of the radio detector is to track the shower development like FD, though with a duty cycle of around 100%. AERA is still under development und will consist of an array of 150 antennas.

4. Wavelet analysis

In the doctoral thesis "Large Scale Anisotropy Studies of Ultra High Energy Cosmic Rays Using Data Taken with the Surface Detector of the Pierre Auger Observatory" of Marius Grigat [Gri11], the principles of wavelet analysis was introduced in the Pierre Auger Collaboration. This thesis continuous the approach and the goal to search for significant anisotropy in the arrival directions of UHECRs. This anisotropy can be found as point sources or large scale structures. Wavelets are suitable functions for such kind of analysis. In this chapter wavelets and their applications for anisotropy studies are introduced and the analysis technique is illustrated on examples.

4.1 Introduction of wavelets

The expression 'Wavelets' derives from the French word 'ondelette', which means little wave and was created in the 1980s in geophysics by Jean Morlet and Alex Grossmann. Wavelets are mathematical functions, which are used to analyze data on large scale as well as on small scales. There are many different wavelet types as well in 1-dim as in the spherical domain. In contrast to period functions, like sinus or cosinus, which are the bases of Fourier analysis, wavelets are localized in frequency domain as well as in time domain. That make them useful to filter noisy data for local signals. The given analysis task affects the decision to choose the wavelet type and scale. It is possible to decompose data into their wavelet coefficient and transform them back, which is very useful in data compression. This is referred to as the continuous and the discrete wavelet-transformation [Bré02]. Today the application possibilities for wavelets spread in various topics of scientific and commercial areas, like medicine, meteorologic, geophysics and astrophysics.

4.2 1-dim analysis

This section describes the principles of wavelets and wavelet transforms. The analysis technique is based on the article "A Practical Guide to Wavelet Analysis" [TC98]. This analysis technique convolutes the signal distribution and a mother-wavelet to reconstruct the position of a localized signal.
A simple application example of this technique is the reconstruction of the position of a Gaussian signal in a one-dimensional case, which is shown in figure 4.1. A Gaussian signal distribution is placed in one-dimensional space. The used mother-wavelet, in this case is the 1-dim Mexican hat

$$\psi_{MH}(x) = \frac{1}{\sqrt{|a|}} \left(1 - \frac{x^2}{a^2}\right) e^{\frac{-x^2}{2a^2}} , \tag{4.1}$$

is converted into a bin distribution, which is shown as the blue curve in figure 4.1.

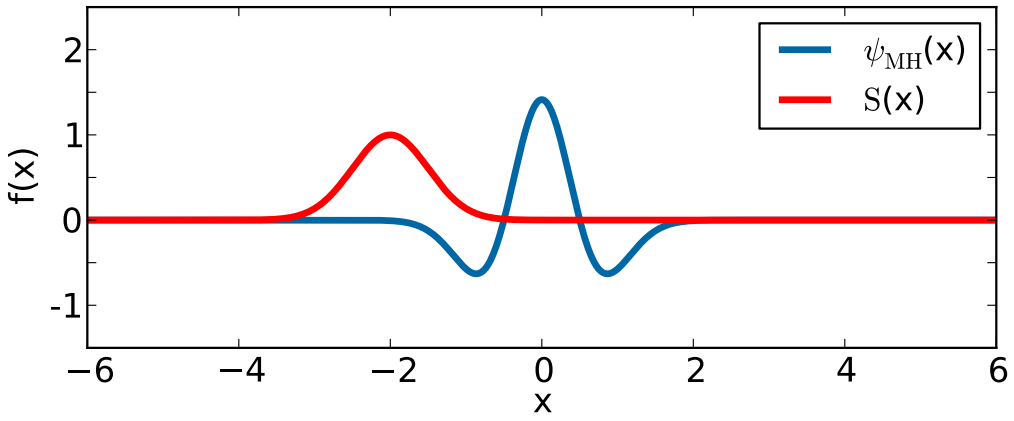

Figure 4.1: 1-dim analysis example with a Gaussian signal $S(x)$ in red and the Mexican hat wavelet $\psi_{MH}(x)$ in blue.

To apply the analysis the Fast Fourier transform (FFT) is used, which is a fast version of the Discrete Fourier Transform (DFT). The Fourier Transform of signal and wavelet are given by

$$X_j = \sum_{k=0}^{N-1} S_k e^{-\frac{2\pi i}{N} jk} \tag{4.2}$$

and

$$\psi_j = \sum_{k=0}^{N-1} \psi_{MH_k} e^{-\frac{2\pi i}{N} jk} \,, \tag{4.3}$$

with i the imaginary unit and N the number of bins of the distribution. The distribution values are given by $X_j = X_(\nu_j)$, $S_k = S(x_k)$, $\psi_j = \psi(\nu_j)$ and $\psi_{MH_k} = \psi_{MH}(x_k)$. The FFT of the signal $X(\nu)$ and the wavelet $\psi(\nu)$ are convoluted in the frequency domain, which can be calculated by

$$P_j = X_j \cdot \psi_j \,, \tag{4.4}$$

where the value correspond to $P_j = P_(\nu_j)$. The absolute value of the convolution is shown in figure 4.2 as the purple curve. The result of the convolution $P(\nu)$ is transformed backward into the spatial domain with the inverse Fast Fourier transformation (iFFT), which is given by into the spatial domain with the inverse Fast Fourier transformation (iFFT), which is given by

$$P_k = \sum_{j=0}^{N-1} P_j e^{\frac{2\pi i}{N} kj} \,, \tag{4.5}$$

where the value correspond to $P_k = P(x_k)$. The result of this technique is shown in figure 4.3. The amplitude $P(x)$ is given in the arbitrary unit 'Power'. One can clearly see the peak position of the Gaussian signal. The resulting power amplitude

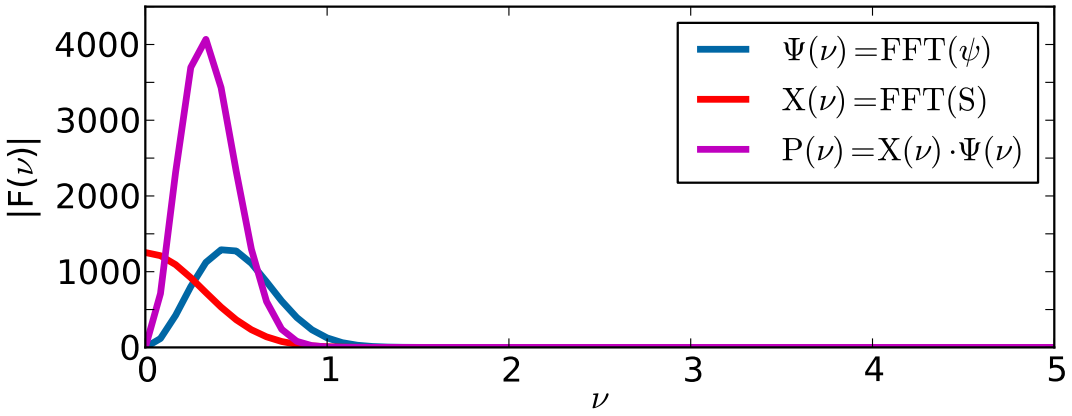

Figure 4.2: FFT of Gaussian signal $X(\nu)$ in red, the Mexican hat wavelet $\psi(\nu)$ in blue and the result of the convolution $P(\nu)$ in magenta.

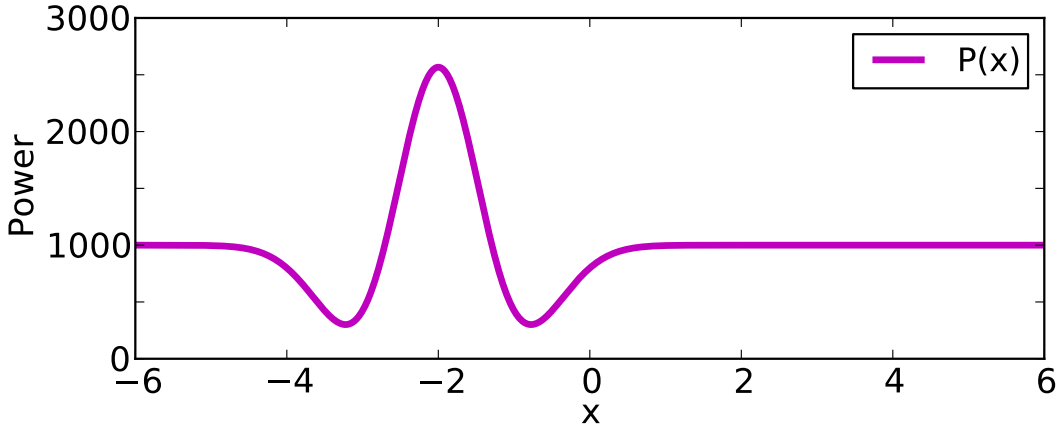

Figure 4.3: The signal is reconstructed on the correct position.

of the peak depends on the start parameter of the mother-wavelet. The width of the mother-wavelet defines the sensitivity for the signal size. The more similar wavelet and signal are, the higher is the power amplitude of the reconstructed peak. This allows the wavelet analysis to be done on multiple scales.

4.3 Spherical analysis

The basic idea of a wavelet analysis on the sphere is working the same way as in the 1-dim case. Whereas, the FFT is replaced by the multipole expansion, which will be explained in more detail in the following subsection. In figure 4.4 the analysis steps are diagrammed. Signal and mother-wavelet have to be converted in their spherical harmonics and then convoluted. The convoluted result is transformed back into the spatial domain to get the filtered result. Anisotropy technique can now be applied on the filtered distribution.

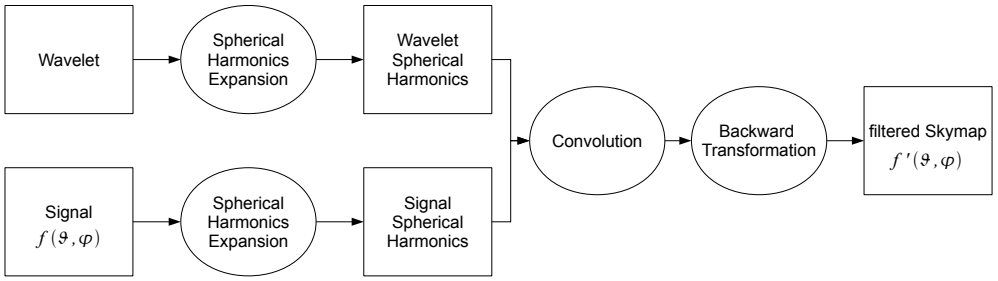

Figure 4.4: Flow diagram of spherical wavelet analysis.

4.3.1 Multipole expansion

The multipole expansion is a mathematical series representing a function that depends on the two angles (θ, φ) on the sphere. Popular examples for application possibilities are in the electrostatic or the magnetostatic theory. The spherical harmonic functions $Y_{lm}(\theta, \varphi)$ need to be computed which are defined as

$$Y_{lm}(\theta,\varphi) = \sqrt{\frac{2l+1}{4\pi}\frac{(l-m)!}{(l+m)!}} P_l^m(cos\theta) e^{im\varphi} \,. \tag{4.6}$$

P_l^m are the associated Legendre polynomials with coefficients $l = 0, 1, 2, ...$ and $m = 0, \pm1, \pm2, ..., \pm l$. The coefficient $l = 0$ describes a monopole, $l = 1$ describes a dipole, $l = 2$ stands for a quadrupole and so on. The distribution of the spherical data $f(\theta, \varphi)$ is converted into the multipole expansion, which is defined as

$$f(\theta,\varphi) = \sum_{l=0}^{\infty} \sum_{m=-l}^{+l} a_{lm} Y_{lm}(\theta,\varphi) \,. \tag{4.7}$$

There a_{lm} denotes the multipole coefficient of the spherical harmonic $Y_{lm}(\theta, \varphi)$. The infinite first sum determines the angular precision of this series and it is necessary to set a maximum multipole moment to reduce the needed computational resources considering the resolution of the dataset. Therefore, only a reasonable range of multipole moments is used for the analysis in this thesis.

4.3.2 Healpix software

The data samples in astrophysics are continuously distributed in spherical coordinates, and so it is suitable to separate the spherical surface into equal size bins. For this purpose the Healpix software is very useful. Healpix stands for 'Hierarchical Equal Area isoLatitude Pixelization' of a sphere [NAS]. The software was written to analyze the temperature differences of the CMB and is able to perform a fast expansion into the spherical harmonics. The pixel structure of the sphere is shown in figure 4.5. The pixels are numbered by the factor k, which is shown in figure 4.6. In the further analysis the factor k always refers to this scheme. The spherical data map is displayed in the Hammer-Aitoff projection, which is an equal-area map projection on an ellipse.

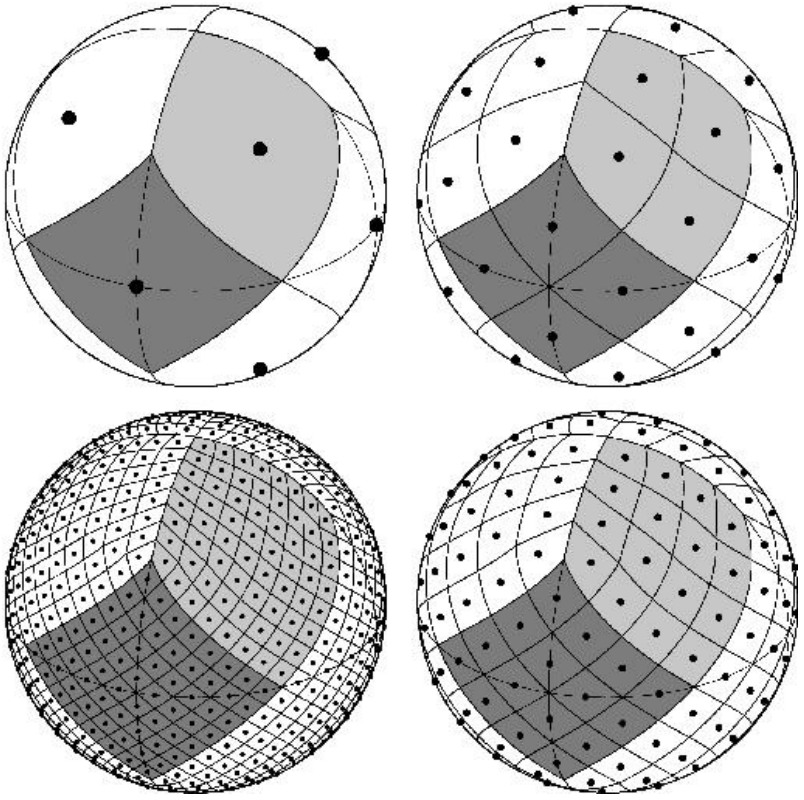

Figure 4.5: Healpix binning structure [NAS].

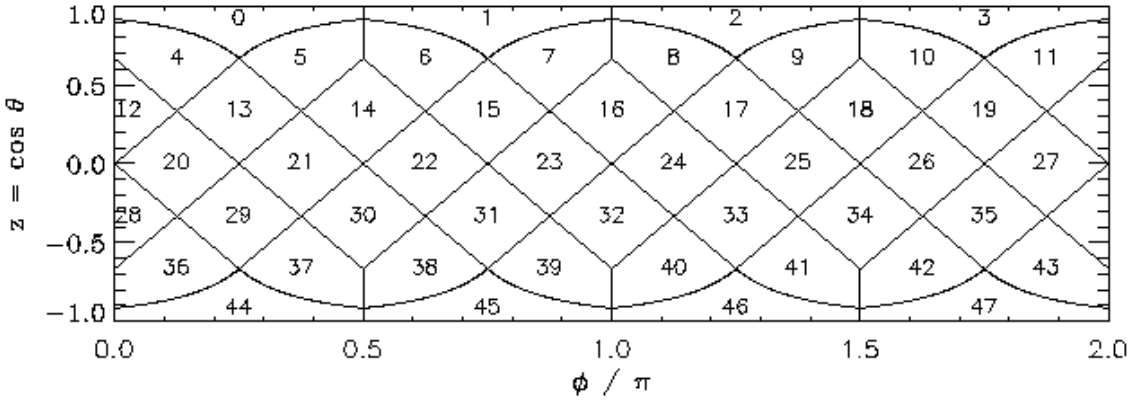

Figure 4.6: Healpix pixel numeration [NAS].

4.4 Wavelet shape

There are many different wavelet designs which can be chosen. Established examples for spherical wavelets are the spherical Mexican hat or the spherical Haar wavelet, which were both used for CMB anisotropy studies. In the following analysis the needlet wavelet will be used for anisotropy search.

4.4.1 Needlet

The needlet is a type of spherical wavelet that was introduced by the CMB community [MPB+07]. It does not rely on any kind of tangent plane approximation,

which is needed for the Spherical Mexican Hat wavelet shown in [CSMG+01]. The needlet possesses a good localization in spatial as well as in frequency domain. Another advantage is that the needlet is exactly localized on a finite number of multipole moments. The range of the needlet is chosen by the input parameters j and B. In the following the parameter j is called needlet scale and the parameter B is called needlet width. The needlet can be adapted to the Healpix pixel scheme very simply. The needlet function in the Healpix pixel scheme is defined as

$$\psi(\theta,\varphi) := \sqrt{\lambda_{jk}} \sum_{l} b(l, B^{-j}) \sum_{m=-l}^{l} \overline{Y}_{lm}(\theta,\varphi) Y_{lm}(\xi_{jk}) \,. \tag{4.8}$$

The factor k is the pixel number on the sphere, which is shown in figure 4.6. The normalization λ_{jk} denotes the cubature weights. In this analysis it can be envisaged as $1/N_{pix}$, where N_{pix} stands for the number of pixels of the sphere. ξ_{jk} denotes coordinates of the pixel center of the Healpix scheme. The needlet can be seen as a convolution of the projection operator $\overline{Y}_{lm}(\theta,\varphi)Y_{lm}(\xi_{jk})$ and a needlet kernel function $b(l, B^{-j})$. The needlet kernel function $b(l, B^{-j})$ corresponds to a filter with values from zero to one, which is based on the multipole moment l, the needlet width B and the needlet scale j for the spherical harmonics. The needlet kernel function for various scales j is shown in figure 4.8 and for different needlet width B is shown in figure 4.7. The detail informations about the kernel function are shown in the appendix A.2 and in [MPB+07]. With increasing needlet scale j larger multipole

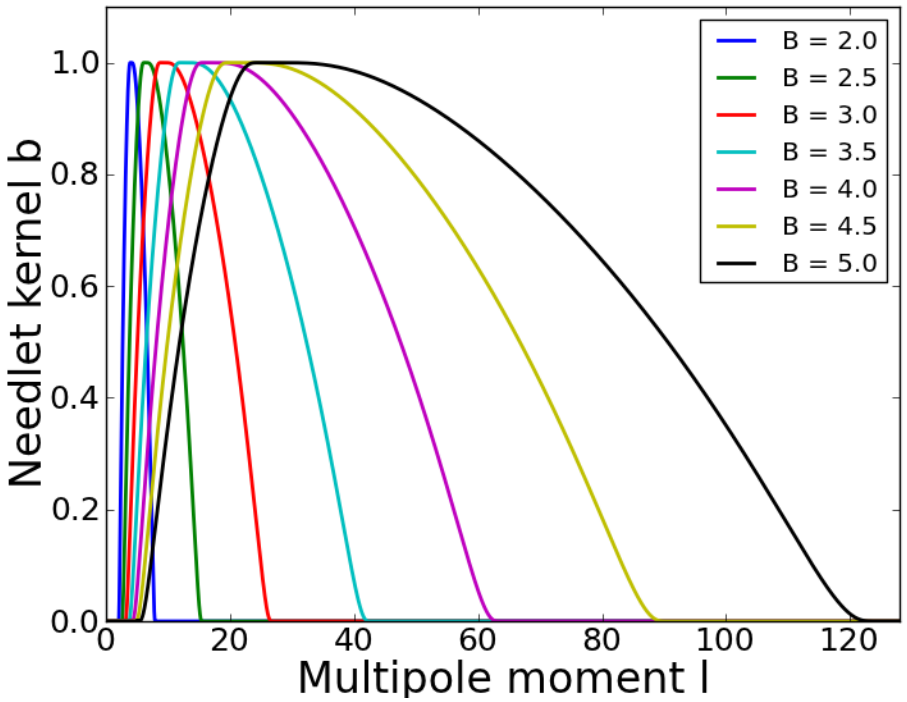

Figure 4.7: Needlet kernel function $b(l, B^{-j})$ against the multipole moment l for various needlet width B with a fixed needlet scale $j = 2$.

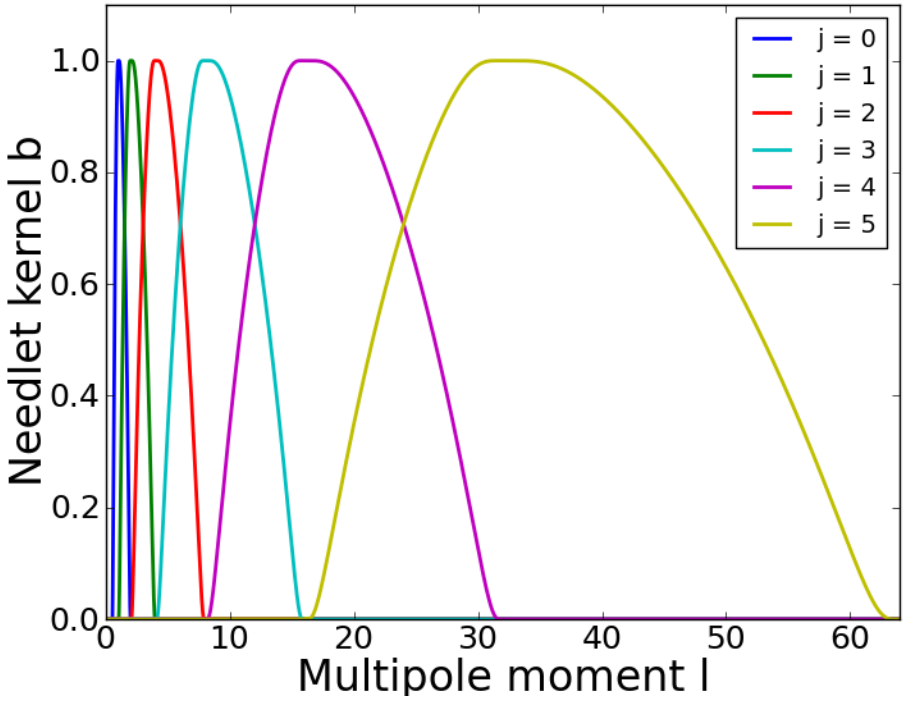

Figure 4.8: Needlet kernel function $b(l, B^{-j})$ against the multipole moment l for various scales j with a fixed needlet width $B = 2.0$.

moments l are implemented. A higher multipole moment corresponds to smaller structures, so larger scale j denotes narrower needlet. With the empirical formula 4.9, the multipole range of the needlet can be transferred into the sensitive angular resolution α of the scale

$$\alpha \approx \frac{180^\circ}{l} \,. \tag{4.9}$$

Figure 4.8 also shows that one needlet scale j has a correlation only to its next neighbors. In this case a data sample can be analyzed at various scales with only a minimal correlation. However, in case of an incomplete dataset, like the unseen or masked area on the sphere, there is a larger correlation between the scales, but it is still in a reasonable scope. For detail information on correlation see [MPB+07]. When the signal distribution $f(\theta, \varphi)$ is expanded into the spherical harmonics coefficient a_{lm} the needlet power value β_{jk} for a pixel k in the Healpix scheme is defined as

$$\beta_{jk} := \sqrt{\lambda_{jk}} \sum_l b(l, B^{-j}) \sum_{m=-l}^{l} a_{lm} Y_{lm}(\xi_{jk}) \,. \tag{4.10}$$

In figure 4.9 lateral projections of needlets with the scale $j = 3$ and $j = 4$ are shown. It shows the needle-like structure with quasi-exponential localization and the different size for various scales. This shows the resolution a specific needlet scale is sensitive to. A Hammer-Aitoff projection of a needlet is shown in figure 4.10. It shows the spherical symmetry of the needlet which is defined rotationally symmetric around the pole-axis of the sphere.

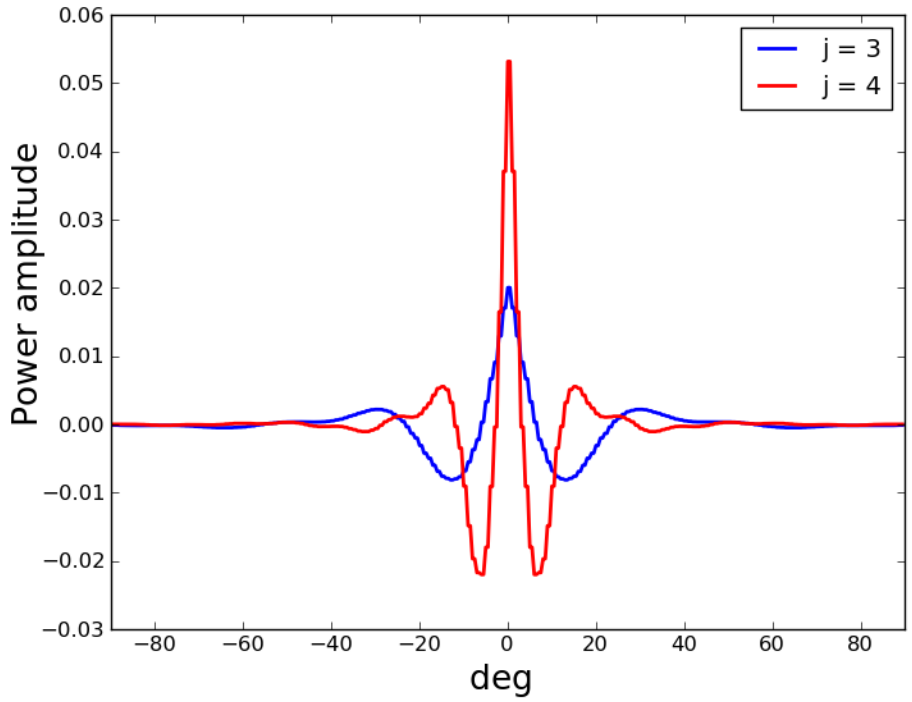

Figure 4.9: Needlet shape for the scale $j = 3$ and $j = 4$ with a needlet width $B = 2.0$.

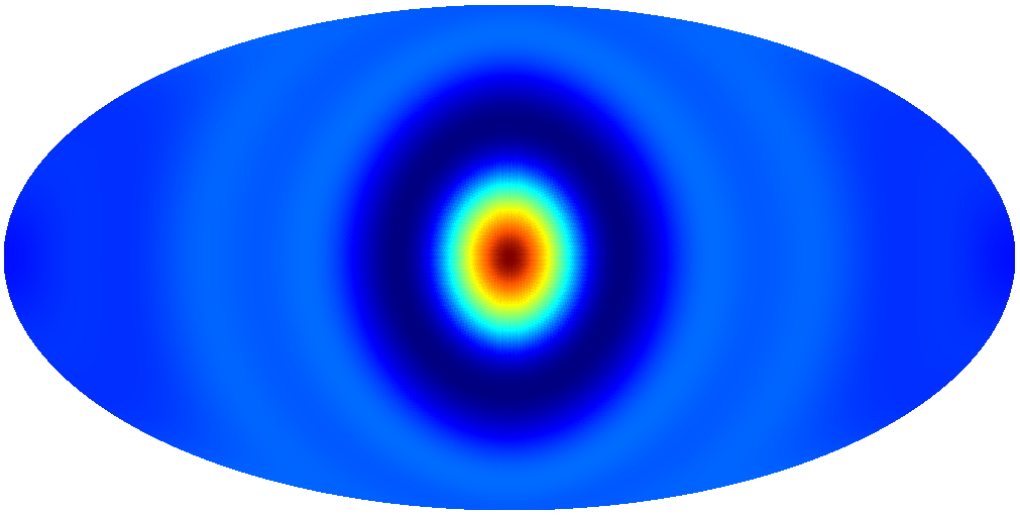

Figure 4.10: Needlet for the scale $j = 2$ in Hammer-Aitoff projection. This shows the spherical symmetry the projection view is centered at the pole.

4.4.2 Needlet and Healpix parameters

The following parameters for the further analysis are kept fixed in all examples and plots. Due to the angular resolution of the SD array the Healpix pixel size is set to the parameters shown in table 4.1. The errors on the angular reconstruction will be neglected for the further analysis.

$Nside$	$= 32$
N_{pix}	$= 12228$
$\rightarrow Pixelsize$	$\approx 1.83^{\circ}$

Table 4.1: Healpix parameters

The pixel size determines the maximal needlet scale j_{max}. Therefore, the needlet kernel function with a needlet width $B = 2.0$ in figure 4.8 shows that the limit l_{max} of the multipole extension can be set to a fixed value to reduce the computational complexity. Higher needlet scales j are only sensitive to the binning structure. The chosen parameters for the needlet analysis are shown in table 4.2.

B	$= 2.0$
j_{max}	$= 5$
$\rightarrow l_{max}$	$= 64$

Table 4.2: Needlet parameters

5. Study of UHECRs arrival direction on simulated data samples with the needlet analysis

In this chapter the application of the needlet analysis is presented, which is tested with various Monte Carlo scenarios of source distributions. It also describes the determination of the significance of the resulting power amplitude value β_{jk} and further analysis methods. As standard number of events for the further Monte Carlo samples 30000 events are taken, because that is the range of statistics later used in the data sample of the Pierre Auger Observatory. In this analysis the equatorial coordinate system is used.

5.1 Monte Carlo simulation on an ideal detector

The needlet analysis returns only a power amplitude value β_{jk} on a skymap in arbitrary units. Therefore, Monte Carlo simulations with isotropic skymaps with various sample sizes need to be done to determine a significance value.
As a first test for this method a 'fullsky' data set is used, which means that the sphere coverage is complete and uniformly weighted. The goal of the test is to reconstruct the position of a single point source. The signal events are randomly distributed based on a Gaussian source density distribution, which is shown in figure 5.1. The parameters for the point source are shown in table 5.1.

Number of events		200
Gaussian smearing σ		10°
Source position	Right ascension	90°
	Declination	−30°

Table 5.1: Fullsky point source parameters

The pure signal test data set is shown in figure 5.2. The signal skymap is filled with isotropic noise, so that the total event count of the test data set is 30000. Figure 5.3 shows the event based skymap, whereupon the needlet analysis is applied. Since, this is a fullsky test, no coverage mask is needed. The result of the needlet analysis for the

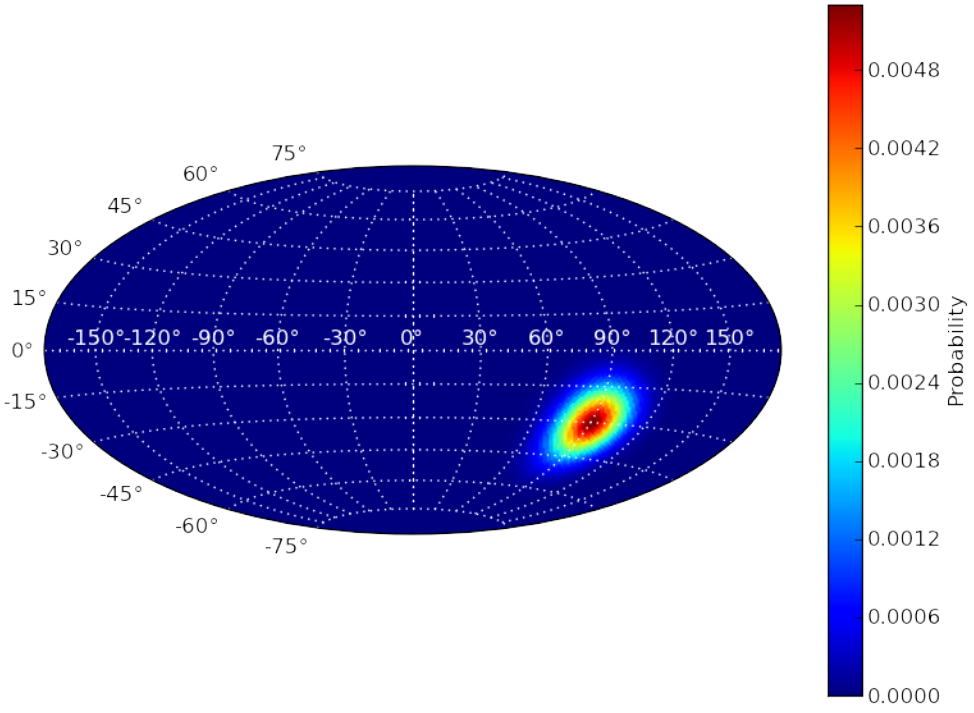

Figure 5.1: Signal density distribution for a point source.

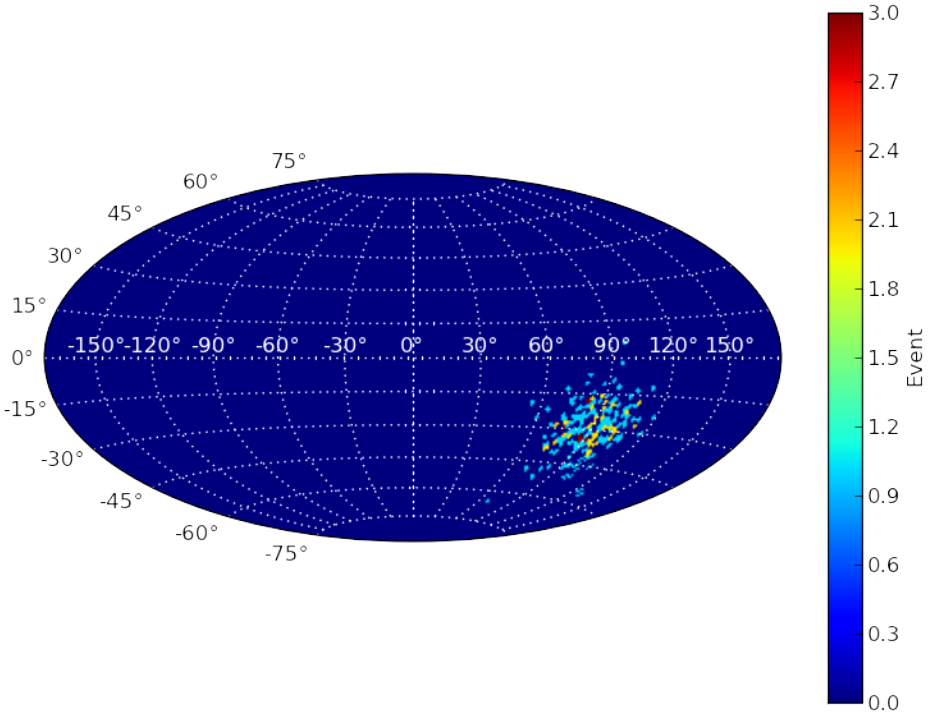

Figure 5.2: Monte Carlo signal skymap with 200 events.

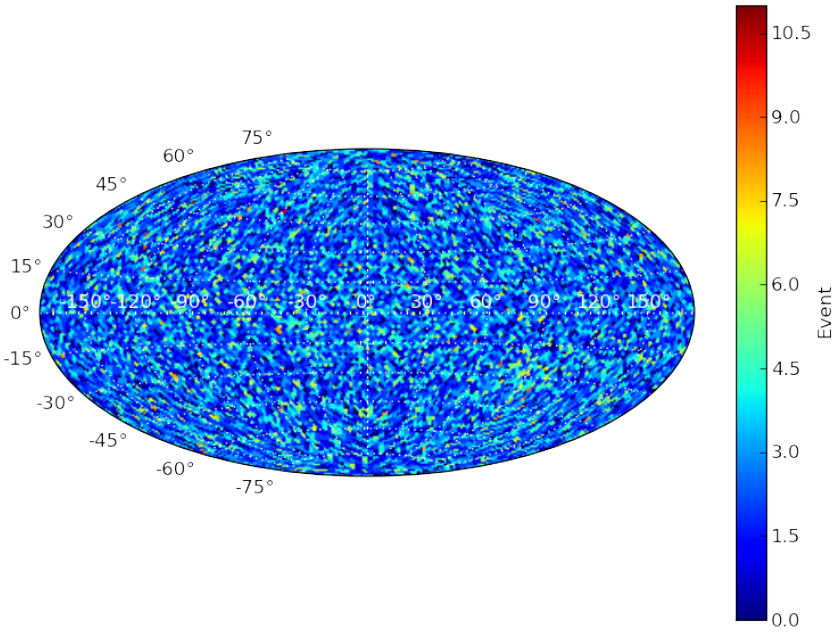

Figure 5.3: Event-based signal skymap with added isotropic noise with 30000 events in total.

different scales j is shown in figure 5.4. The point source of the test data set seems to be visible at the correct position in the resulting plots for the scales $j = 1, 2, 3$. However, there are also large fluctuations, even in scales that are not sensitive to the source like scale $j = 4$ and $j = 5$. This effect was expected because these scales are not sensitive to sources of this size. The scale $j = 0$ is also too insensitive to point sources, because it is mainly sensitive to a dipole. Another important point is, that the power amplitudes of different scales is not directly comparable and if the signal size is unknown no direct selection of the needlet scales can be made for the further analysis.

5.1.1 Power estimation

The significance of the power amplitude can be determined after the needlet analysis. 10000 Monte Carlo samples with only isotropic noise were used. The power amplitude of every pixel in every MC-skymap is investigated. A example for this is shown in figure 5.5 The histogram for each pixel on the skymap has a Gaussian shape. The values for the mean $< \beta_{jk} >$ and the standard deviation σ_{jk} is determined with a Gaussian fit. From this the significance value S_{jk} is defined as

$$S_{jk} = \frac{|\beta_{jk} - < \beta_{jk} >|}{\sigma_{jk}} \,. \tag{5.1}$$

The method to discriminate the power amplitude was also used in the CMB needlet anisotropy analysis [PAB+08]. For a fullsky uniform coverage the Gaussian standard deviation does not depend on the declination, which is shown in figure 5.6. With

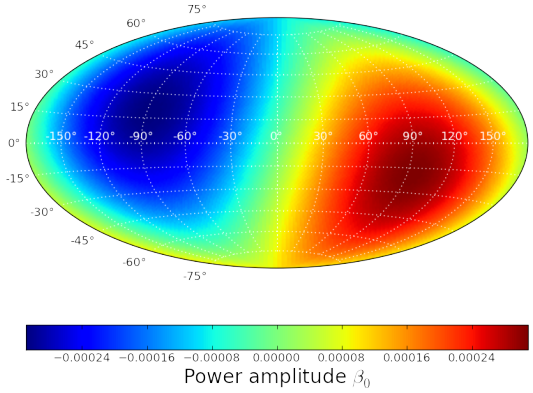

(a) Analysis result at needlet scale $j = 0$

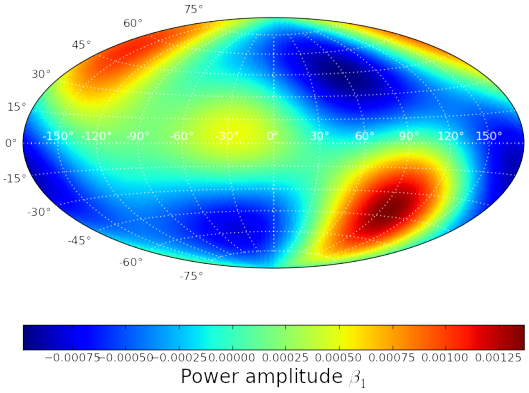

(b) Analysis result at needlet scale $j = 1$

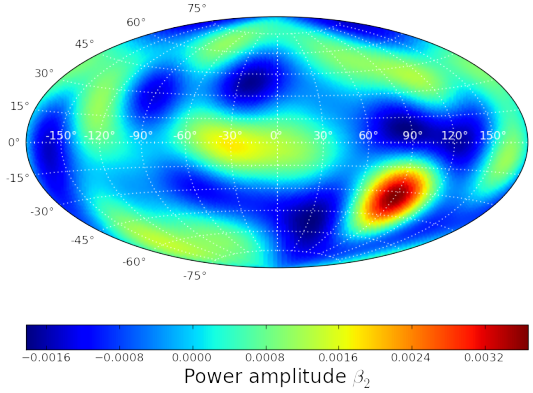

(c) Analysis result at needlet scale $j = 2$

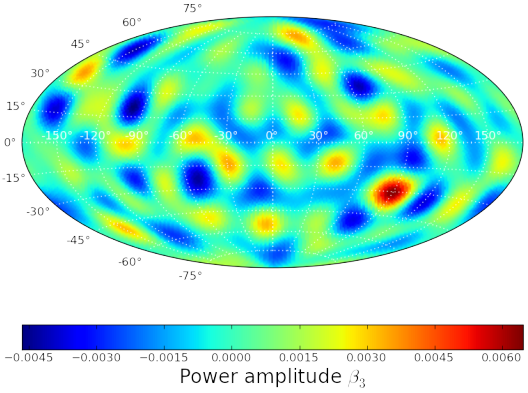

(d) Analysis result at needlet scale $j = 3$

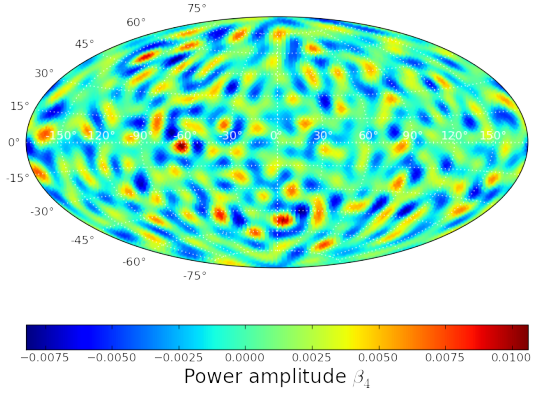

(e) Analysis result at needlet scale $j = 4$

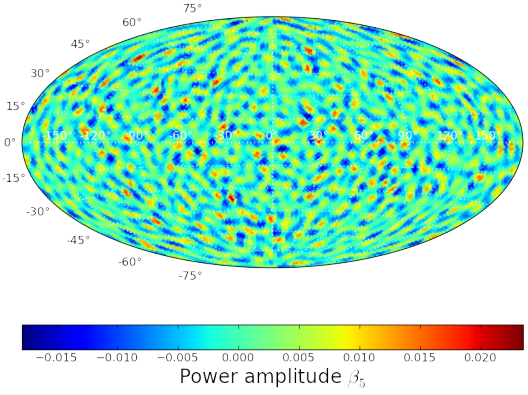

(f) Analysis result at needlet scale $j = 5$

Figure 5.4: Power amplitude β_j of the needlet analysis for a fullsky test data set for different scales j. The point source is visible in the scales $j = 1, 2, 3$ by eye, whereas in the scales $j = 0, 4, 5$ only fluctuations are visible.

these fit values the skymap can be renormalized to a quantity dependent on the standard deviation σ_{jk}.

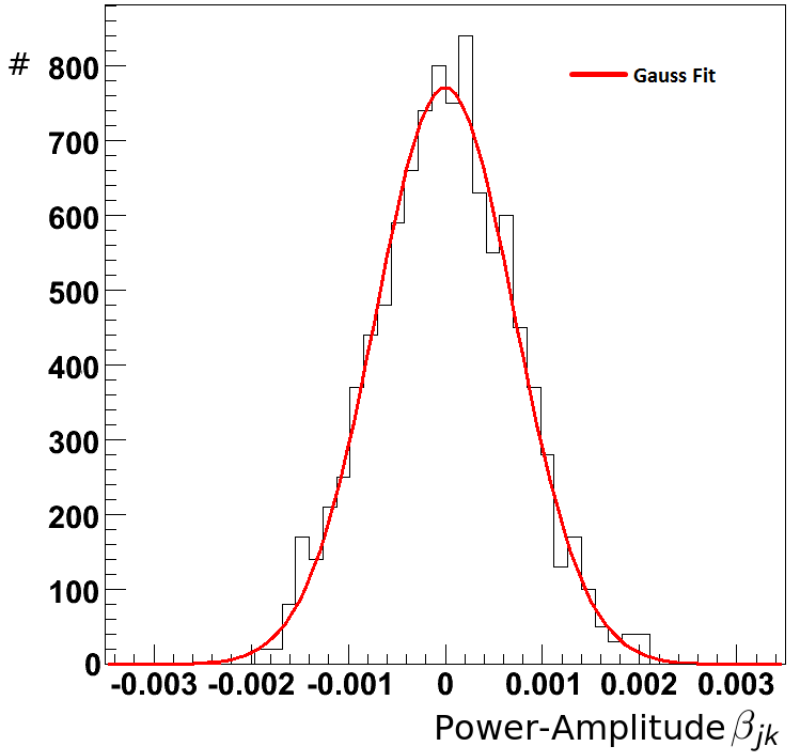

Figure 5.5: Power amplitude β_{jk} distribution for one random pixel k in case of isotropy for needlet scale $j = 2$ and a Gauss fit in red to determine the mean $< \beta_{jk} >$ and the standard deviation σ_{jk}.

5.1.2 Threshold method

As all needlet scales are renormalized to a comparable value, a hard threshold cut on every needlet scale j is applied to determine the significant region of a skymap. The threshold requirement is

$$S^*_{jk} = 0 \quad \text{if} \quad |S_{jk}| < 3 \tag{5.2}$$

$$S^*_{jk} = S_{jk} \quad \text{if} \quad |S_{jk}| \geq 3\,. \tag{5.3}$$

Because of this threshold cut, only regions where the renormalized power amplitude values are above the 3σ-value of isotropy are taken into account for further analysis. This is sensitive to excess as well to deficit in the number of events of the data set. The result of the threshold method is shown in figure 5.7. As the size of signal regions is unknown, there is no way to determine which scale is going to be relevant. Since all j-scales are on the significance level comparable the j-scales can be combined to get one final resulting skymap after the threshold cuts. The combined threshold map is defined as

$$S^*_k = \sum_{j=0}^{j_{max}} S^*_{jk}\,. \tag{5.4}$$

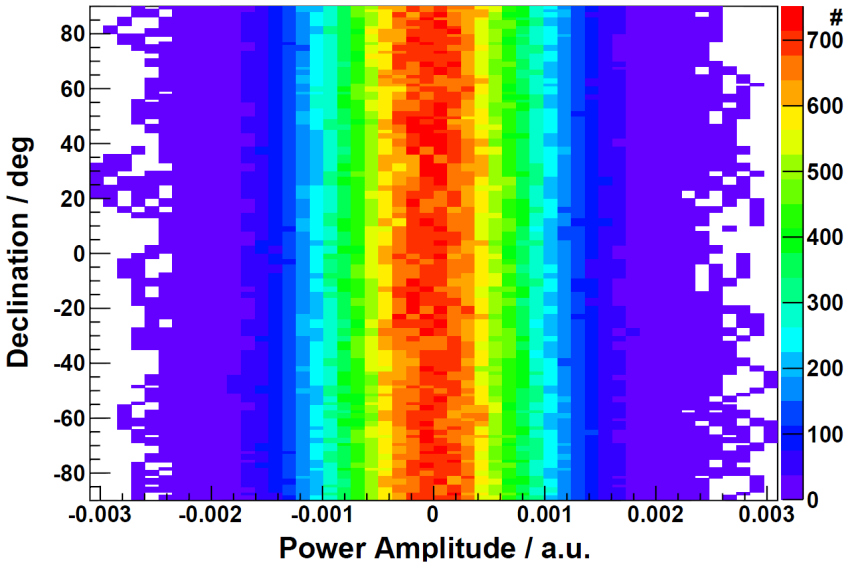

Figure 5.6: Declination vs. power amplitude β_{jk} fluctuations in case of isotropy for needlet scale $j = 2$ with fullsky exposure. The spreading of the power amplitude β_{jk} is independent of the declination in case of an ideal detector.

This method is applied to the fullsky test data set. The result is shown in figure 5.8. A comparison of the combined threshold map and the original source density distribution shown in figure 5.8 shows apparently strong similarity to each other. The pixel with the highest value of S_k^* can be assumed as the equivalent to the center of the point source. Therefore, the accuracy of the reconstruction can be quantified by a simple comparison in table 5.2.

		Set	Reconstructed
Source position	Right ascension	90°	$93 \pm 2°$
	Declination	$-30°$	$-32 \pm 2°$

Table 5.2: Comparison of the set and the reconstructed position of the greatest S_k^* value of the point source center.

These values show, that the point source center was found in the correct region. The error on the reconstructed position is assumed as the width of one pixel of the Healpix scheme. However, there are still regions with false significant signals. Therefore, a global significance value for the whole result needs to be evaluated.

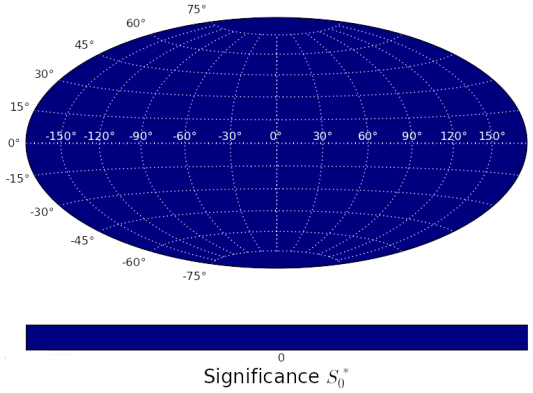

(a) Threshold result at needlet scale $j = 0$

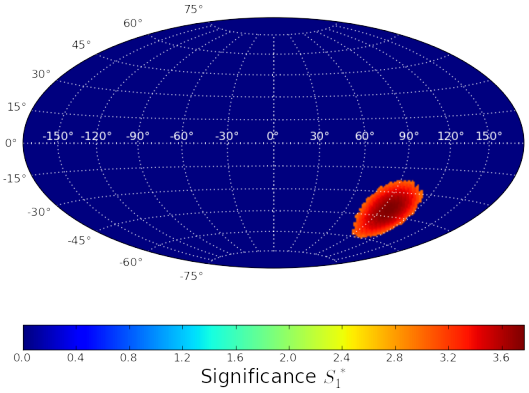

(b) Threshold result at needlet scale $j = 1$

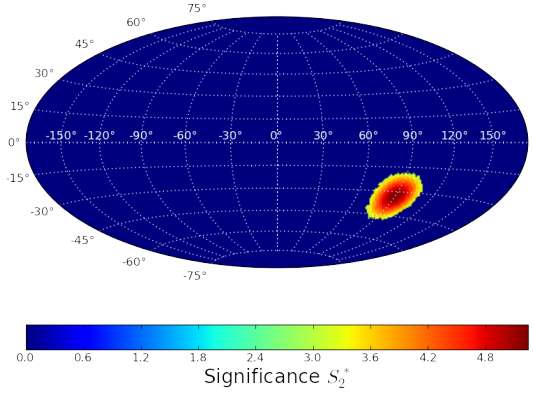

(c) Threshold result at needlet scale $j = 2$

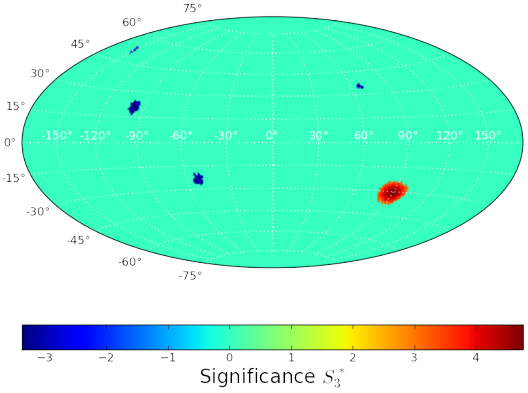

(d) Threshold result at needlet scale $j = 3$

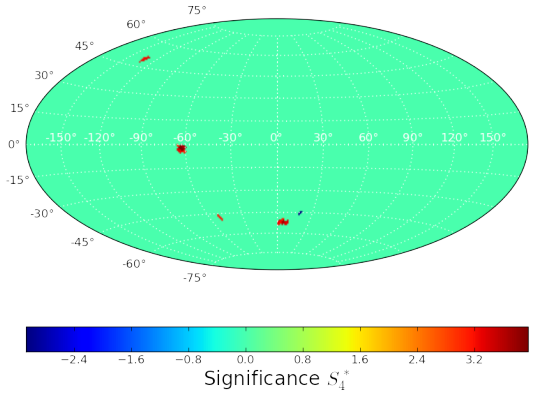

(e) Threshold result at needlet scale $j = 4$

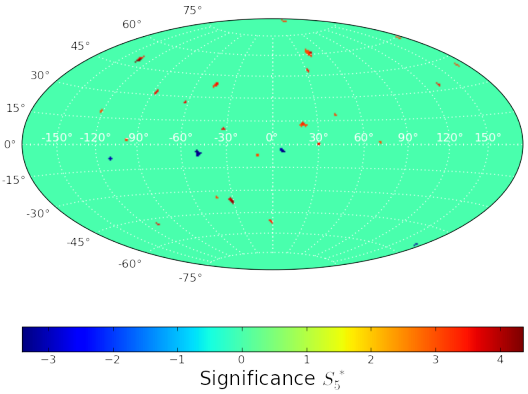

(f) Threshold result at needlet scale $j = 5$

Figure 5.7: Threshold results S_j^* for the fullsky test data set for various scales j. After the threshold cut most of the fluctuations are filtered out and in the scales $j = 1, 2, 3$ the point source is clearly visible. Scale $j = 0$ is now completely empty and in the scales $j = 4, 5$ only a few pixels are kept.

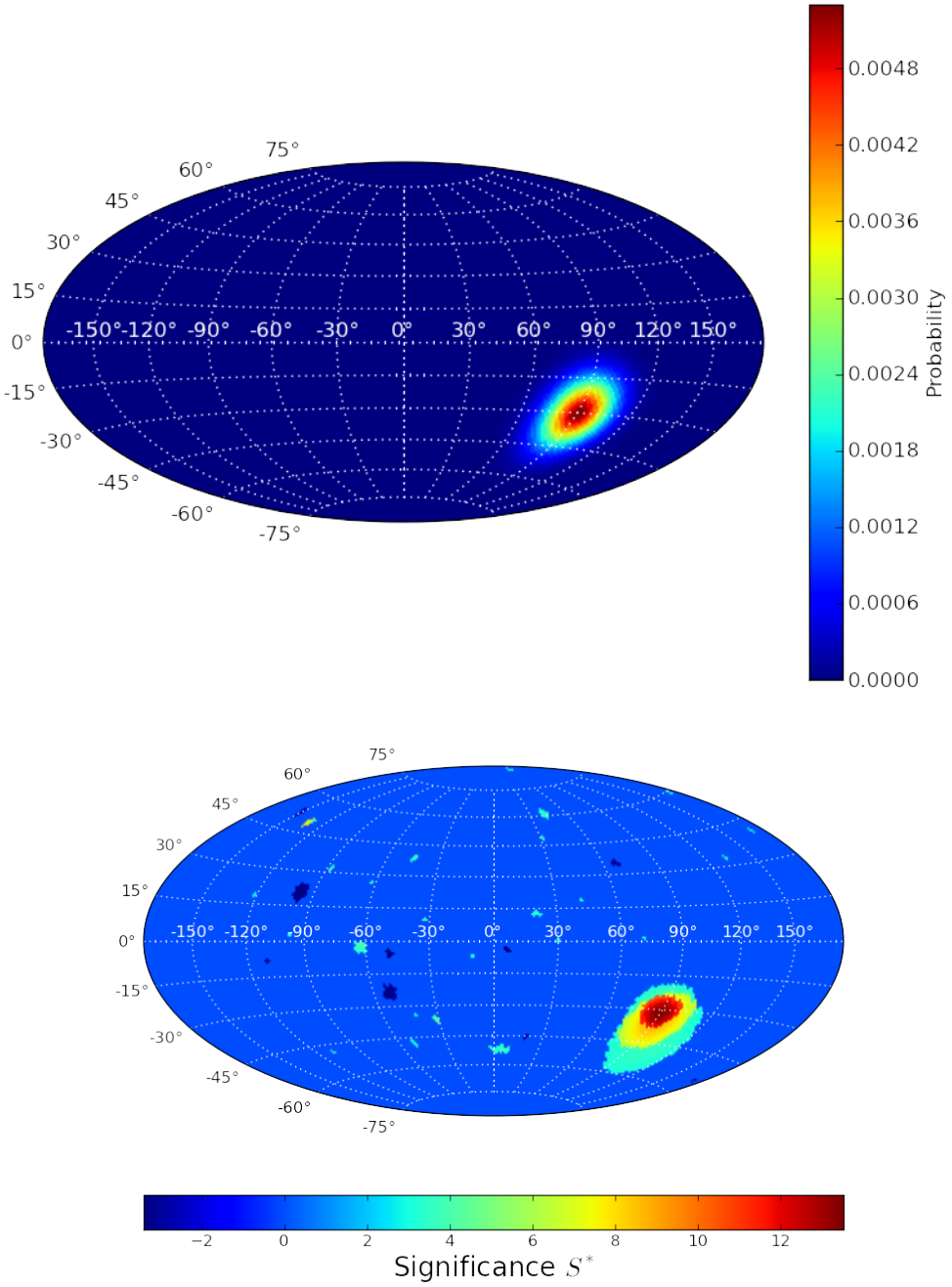

Figure 5.8: Original source density (above) in comparison to the combined threshold map S_k^*(below) for the fullsky test data set. The combined threshold map reflects the correct source distribution.

5.1.3 Significance test

The result of the combined threshold skymaps needs to be investigated to test whether it is compatible with isotropy or not. Therefore, a global significance value D is introduced as

$$D := log\left(\frac{\sum_{k=0}^{N_{Pix}} |S_k^*|}{N_{nonzero}}\right) . \tag{5.5}$$

The value consists of the sum over the absolute value of S_k^*. This value is divided by $N_{nonzero}$, which is the number of pixels with non-zero entries. This is meant to weight the sum, which can be understood by the following example. A dipole would create a larger value of the sum than a small point source. In this way the weight makes the value D sensitive to signals of different scales. The logarithm is used in this case to stretch the distribution of this value. To use this value as global significance test, the D value is tested with 10000 isotropy skymaps with 30000 events each. The fullsky test data set was finalized by computing the D value for this test. The resulting global significance value D is shown in figure 5.9 in comparison to the values D of 10000 isotropic Monte Carlo data sets. It shows that the probability of this example to be compatible with isotropy is clearly below 0.0001% and that the reconstructed point source is a clear sign for anisotropy.

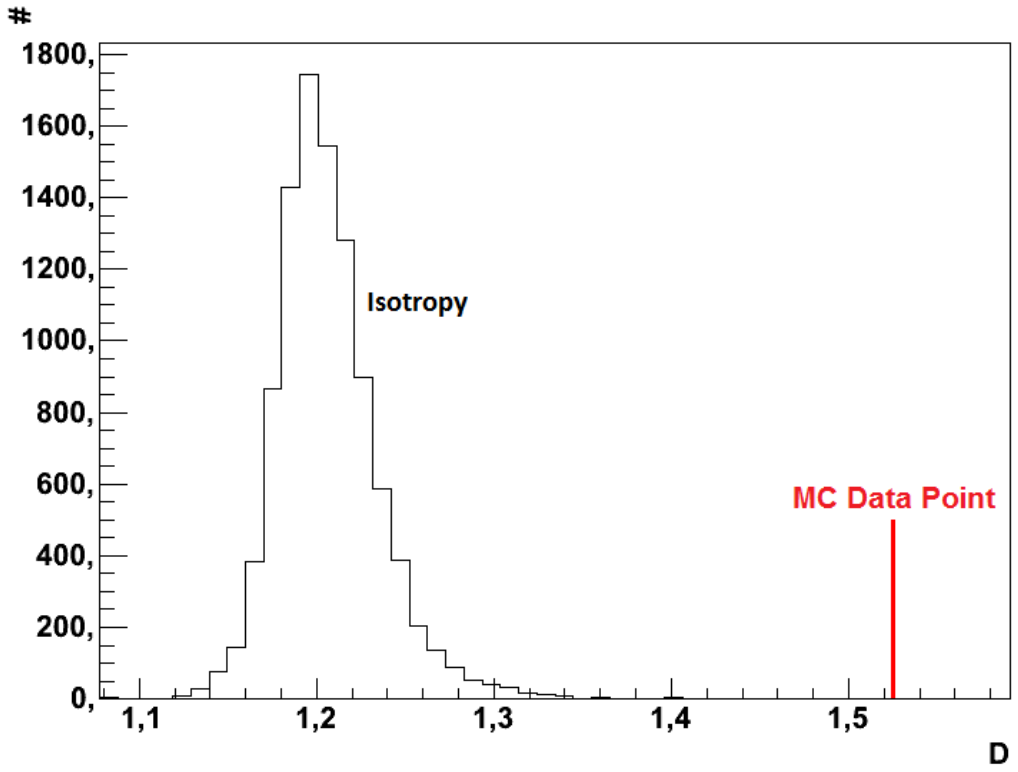

Figure 5.9: Global significance value D of the combined threshold result ($D = 1.5253$) from the fullsky test compared to the values of 10000 isotropic Monte Carlo data sets. The probability to be compatible with isotropy is clearly below 0.0001%.

5.1.4 Comparison of needlet analysis to a multipole analysis

The great advantage of the wavelet analysis compared to a simple multipole analysis is finding local features and anisotropy. The multipole analysis was used in many astrophysical analysis, especially in the analysis of the CMB. In this example a fullsky multipole analysis is performed. In case of a non uniform exposure of the spherical data, there are correlations in the angular power spectrum.
The multipole analysis converts the spherical data into their spherical harmonics with equation 4.7. As the next step the angular power spectrum C_l for every multipole moment l is calculated with the multipole coefficients a_{lm} by

$$C_l = \frac{1}{2l+1} \sum_{m=-l}^{+l} |a_{lm}|^2 \,. \tag{5.6}$$

The angular power spectrum is calculated for 10000 isotropic Monte Carlo data sets. The values of every isotropic skymap are plotted together in one histogram, which is shown in figure 5.10. In this plot the z value for each multipole moment l is renormalized to an integral value of 1, so that the probability for C_l is shown. With

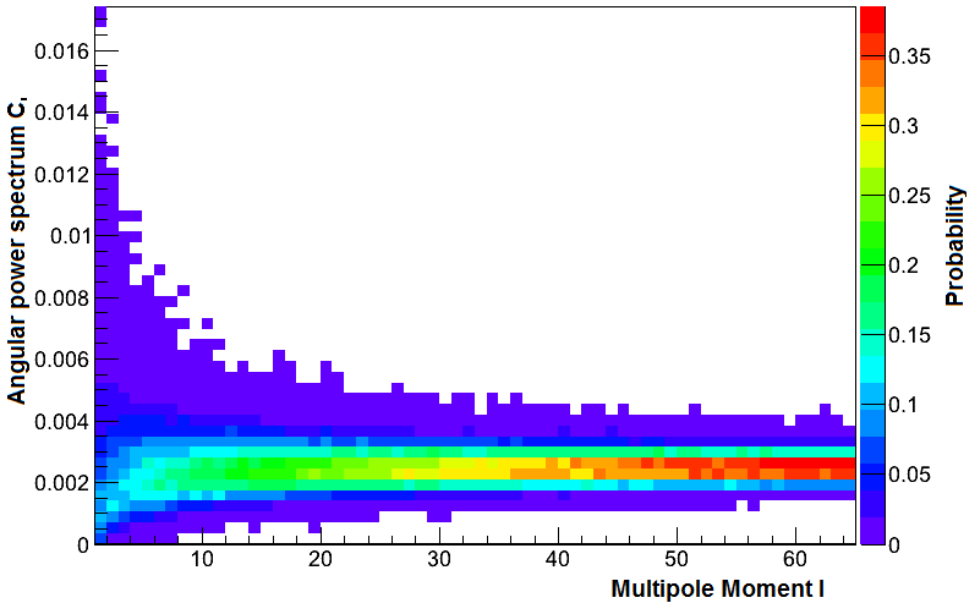

Figure 5.10: Angular power spectrum C_l for 10000 isotropic Monte Carlo data sets. In this plot the z value for each multipole moment l is renormalized to an integral value of 1, so that the probability for C_l is shown.

this probability map a negative Log-Likelihood-Test is performed to check if the test data set's angular power spectrum is compatible with isotropy. The negative Log-Likelihood value L is given by

$$L = -2 \sum_{i=l}^{l_{max}} ln(P_{Poisson}(x_{i,data}|x_{i,MC})) \tag{5.7}$$

where l_{max} is the range of the multipole moments and $P_{Poisson}(x_{i,data}|x_{i,MC})$ is the probability of one data point $x_{i,data}$ to be compatible with the isotropic data $x_{i,MC}$. The value L is calculated for 10000 isotropic skymap. This is shown in figure 5.11. The plot shows that the probability to be compatible with isotropy is below 0.0001%.

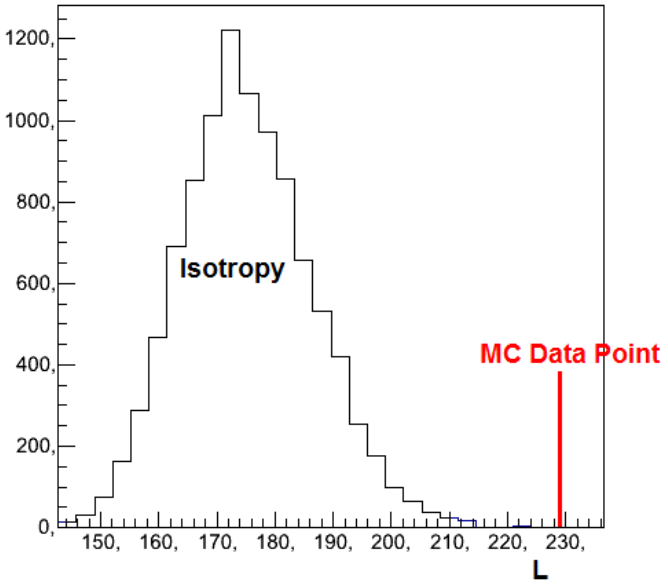

Figure 5.11: Log-Likelihood values L for 10000 isotropic skymaps in comparison to the Log-Likelihood value of the fullsky test data set.

Therefore, both methods are able to determine, if a data set is compatible with isotropy. However, the needlet analysis also gives an additional information about the regions, which cause the anisotropy. Therfore, it is also possible to find point sources and large scale structures.

5.2 Anisotropy search in Monte Carlo data

In the further analysis two Monte Carlo scenarios are tested with the needlet analysis and the threshold method. One scenario consists of a large scale structure of smeared cosmic ray sources based on an astrophysics catalog PSCz, which consists of galaxies. The other scenario is based on an artificial point source distribution containing 4 point sources with different numbers of events and smearing. As background again isotropically distributed events were used. In both scenarios the exposure of the Pierre Auger Observatory (seen in figure 5.12) is applied. The goal of this analysis step is to filter the skymap for point sources and large scale structures and to reconstruct the positions of the sources in the original source density distribution.

5.2.1 Auger exposure

Due to the fact, that the Pierre Auger Observatory is located on the southern hemisphere and EAS with a zenith angle $\geq 60°$ are not used in this thesis, the sky exposure for the data is partial and non uniform. For the Monte Carlo skymaps this effect has to be taken into account. In the simplest case, with an ideal detector the geometrical exposure, shown in figure 5.12, is used as probability density for isotropic Monte Carlo studies. A weighted mask is used during the multipole expansion to

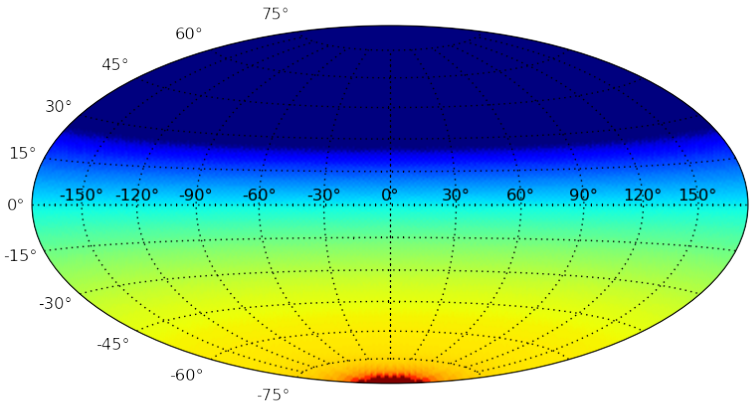

Figure 5.12: Partial and non uniform sky coverage of Pierre Auger Observatory in equatorial coordinates.

analyze a skymap with the Auger exposure. The Monte Carlo data sample of the arrival directions is first inverse weighted with the calculated exposure. During the multipole expansion, the geometrical Auger exposure is used as 'mask'. After that a monopole removing fit is performed. The monopole removing is necessary to use the weighted coverage in Healpix. The removed monopole value is not interesting for the further analysis, so these data can be neglected. To determine the significance of the power value β_{jk} in case of the Auger exposure the mean $< \beta_{jk} >$ and the

standard deviation σ_{jk} for every declination needs to be determined. The result is shown in figure 5.13. The declination has to be taken into account for applying the threshold criteria in case of the Auger exposure.

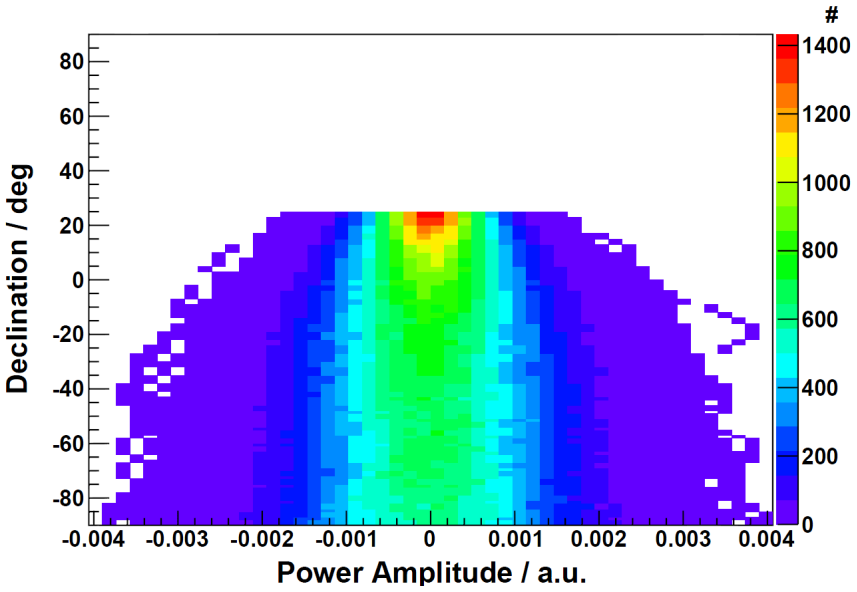

Figure 5.13: Power amplitude β_{jk} fluctuations vs. declination in case of isotropy for needlet scale $j = 2$ with Pierre Auger Observatory exposure.

5.2.2 Large scale structures test

The following Monte Carlo test sample is based on the source density distribution according to the PSCz catalog [SSM+00], which is based on the measurement of the 'Infrared Astronomical Satellite' (IRAS). The source distribution of the galaxies is shown in figure 5.14. The catalog sources are smeared with a Gaussian width 10° and convoluted with the geometric exposure of the Pierre Auger Observatory. The resulting source density distribution is shown in figure 5.15.

The skymap for this Monte Carlo sample consists of 3000 signal events and 27000 isotropic events. The PSCz Monte Carlo skymap is shown in figure 5.16. The needlet analysis is applied on this map considering the geometrical Pierre Auger Observatory exposure. The results are shown in figure 5.17. In contrast to the single point source test sample there is by eye no clear structure visible. This shows the need for further filtering. As the next step the threshold method is applied on the needlet results. The result is shown in figure 5.18. The original source density distribution in comparison to the combined threshold results of the needlet scale $j = [0, 5]$ is shown in figure 5.19. The result shows strong similarity with the underlying source density distribution. However, to determine, if this result is compatible with isotropy the D value is computed and compared to the values D of 10000 isotropic Monte Carlo data sets. This is shown in figure 5.20. The D value for this scenario shows, that the probability to be compatible with isotropy is below 0.0001%. So it can be stated,

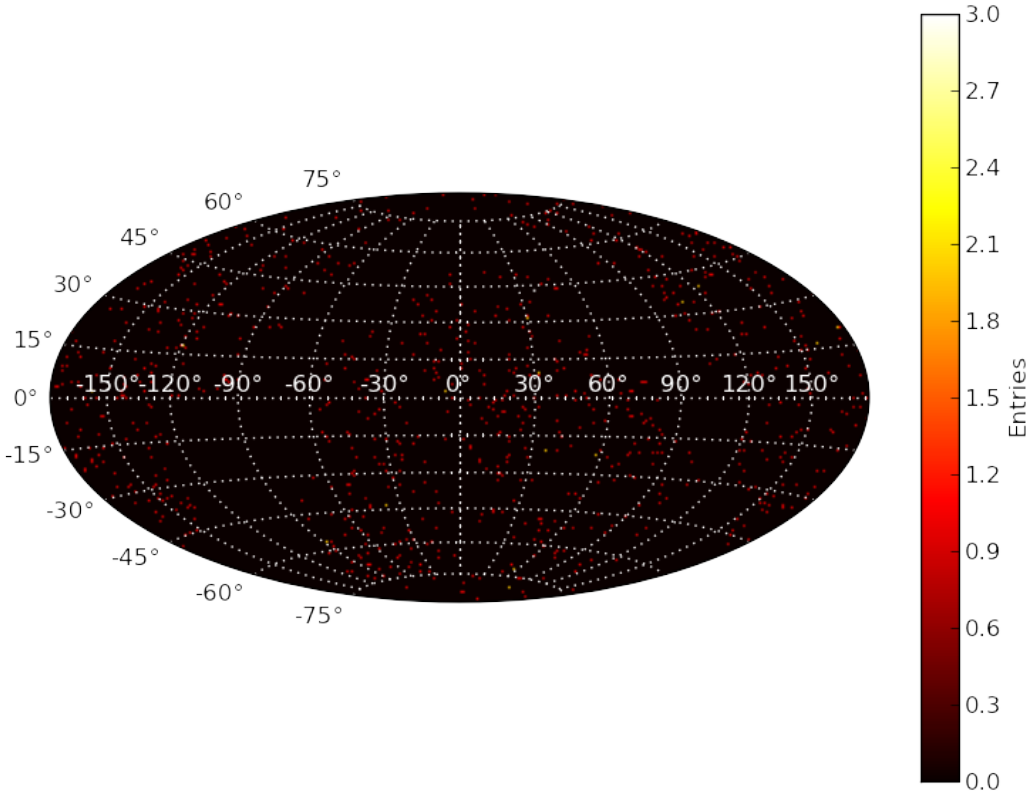

Figure 5.14: The source map based on the PSCz catalog with 12879 point sources.

that this test sample is clearly anisotropic and that the result shown in figure 5.19 shows the source distribution. This result shows, that the needlet analysis is suited also for an anistropy analysis with large scale structures.

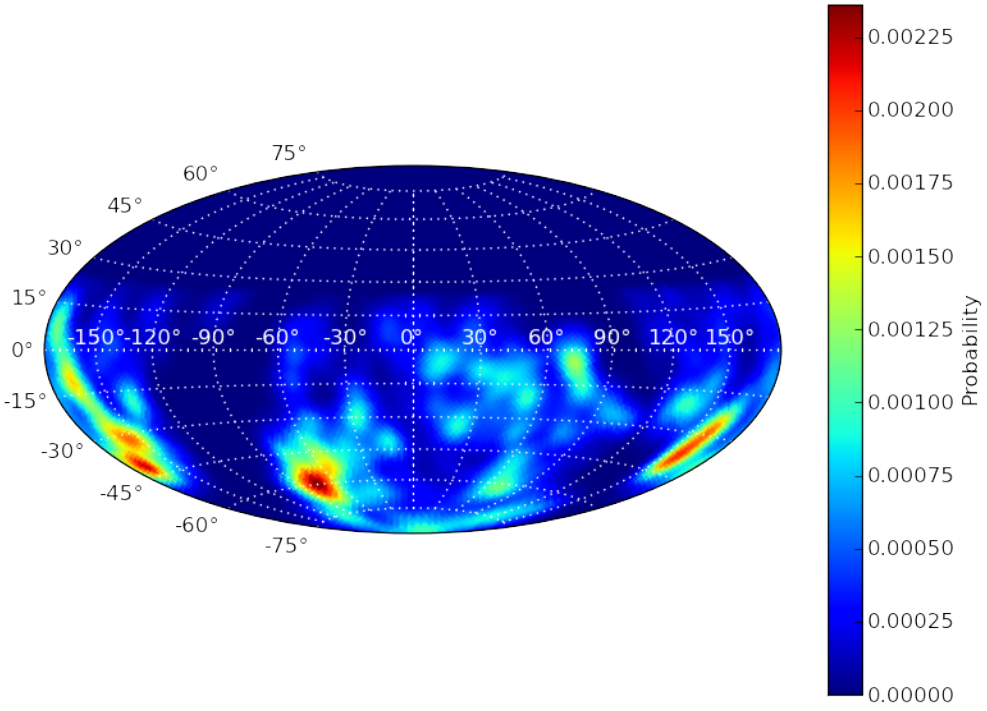

Figure 5.15: The source density distribution based on the PSCz catalog smeared with a Gaussian and convoluted with the Auger exposure.

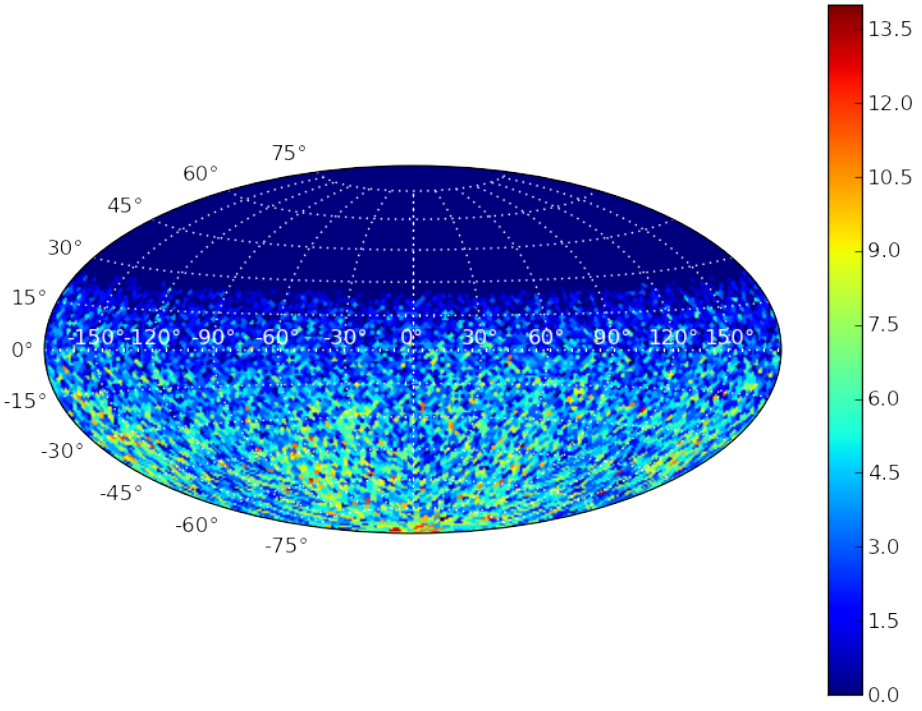

Figure 5.16: Event-based skymap based on the PSCz catalog with additional isotropic noise.

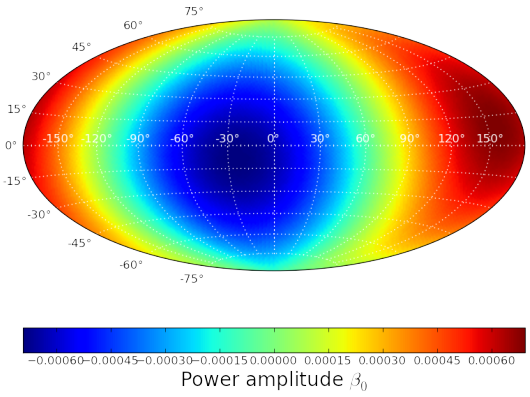

(a) Analysis result at needlet scale $j = 0$

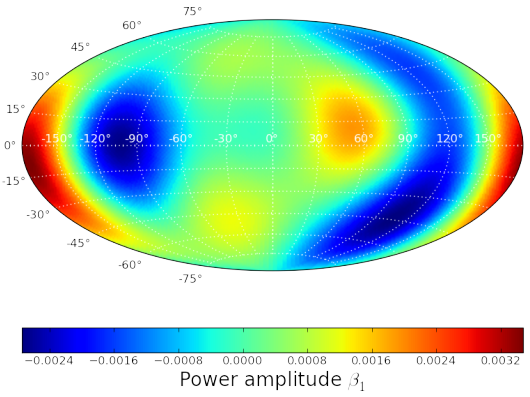

(b) Analysis result at needlet scale $j = 1$

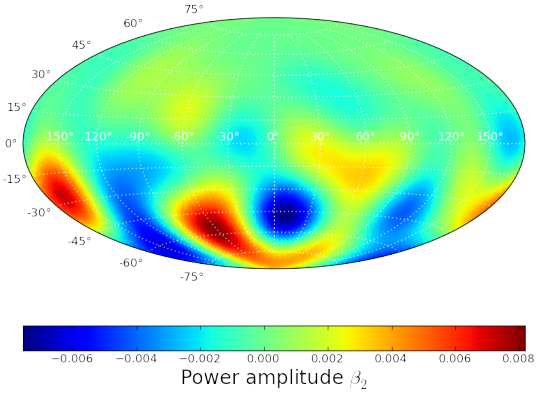

(c) Analysis result at needlet scale $j = 2$

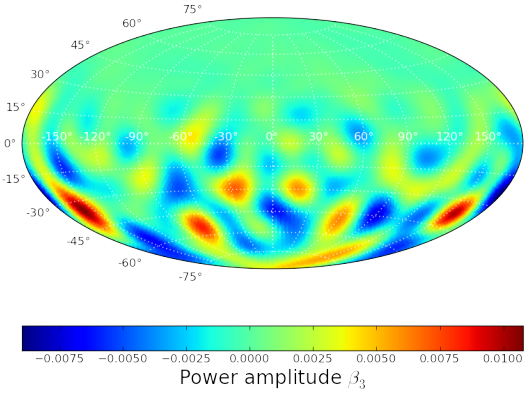

(d) Analysis result at needlet scale $j = 3$

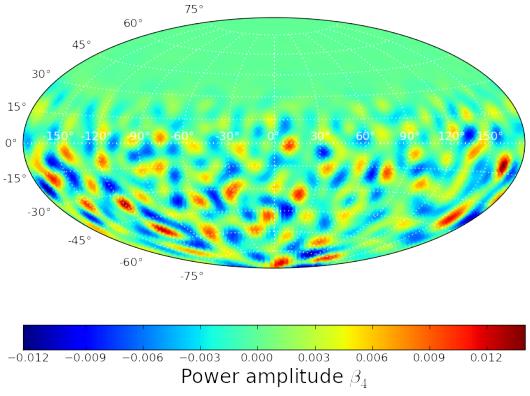

(e) Analysis result at needlet scale $j = 4$

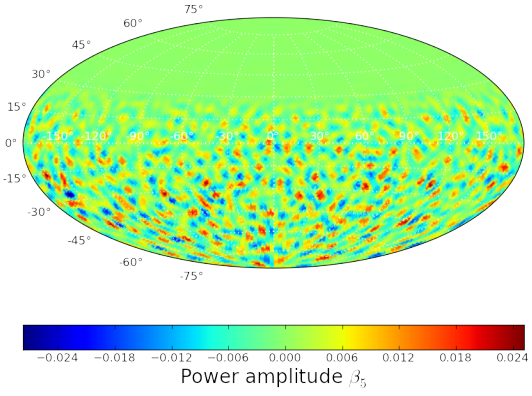

(f) Analysis result at needlet scale $j = 5$

Figure 5.17: Power amplitude β_j of the needlet analysis for a PSCz test sample for different scales j. There is no clear structure visible, so further filtering needs to be done.

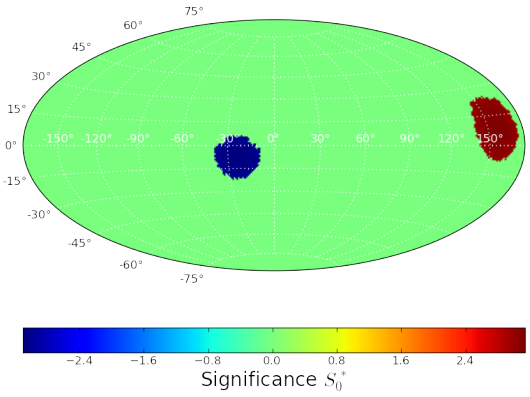

(a) Threshold result at needlet scale $j = 0$

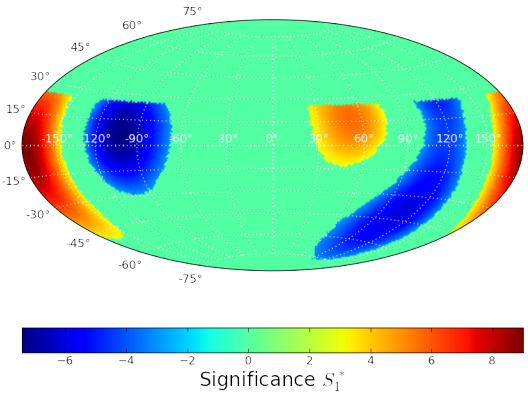

(b) Threshold result at needlet scale $j = 1$

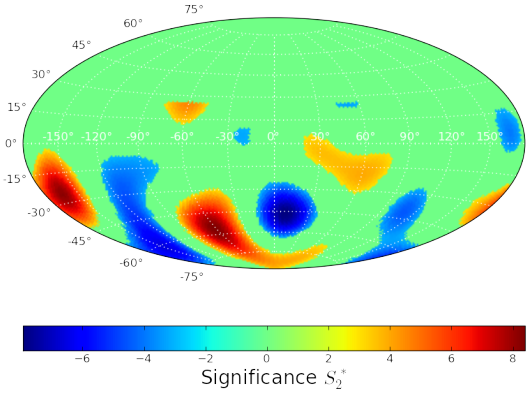

(c) Threshold result at needlet scale $j = 2$

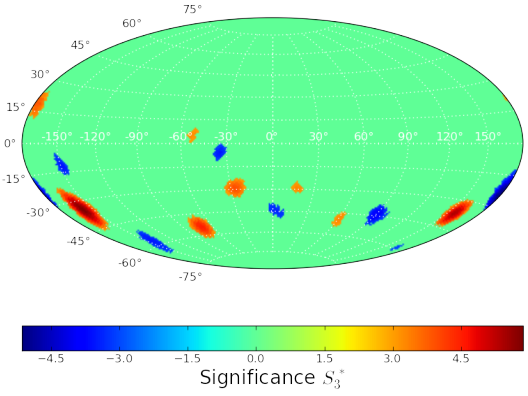

(d) Threshold result at needlet scale $j = 3$

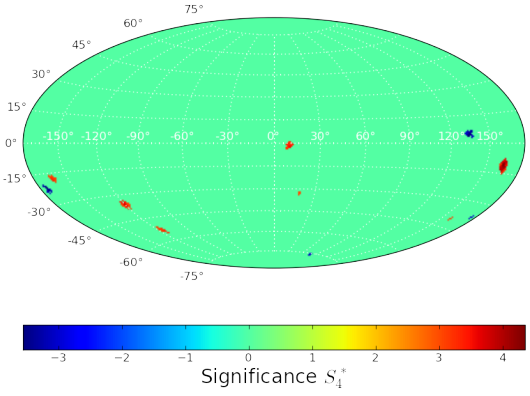

(e) Threshold result at needlet scale $j = 4$

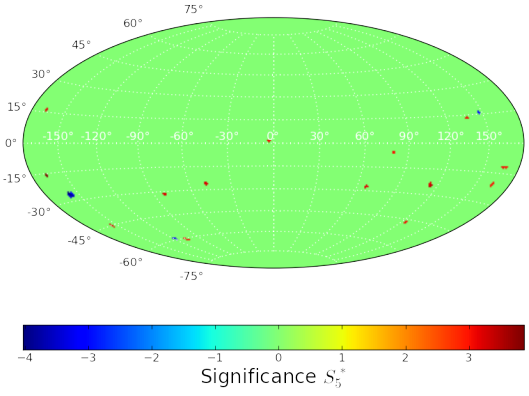

(f) Threshold result at needlet scale $j = 5$

Figure 5.18: Threshold results S_j^* for a PSCz test sample for various scales j. After the threshold cut most of the fluctuations are filtered out and structures become visible.

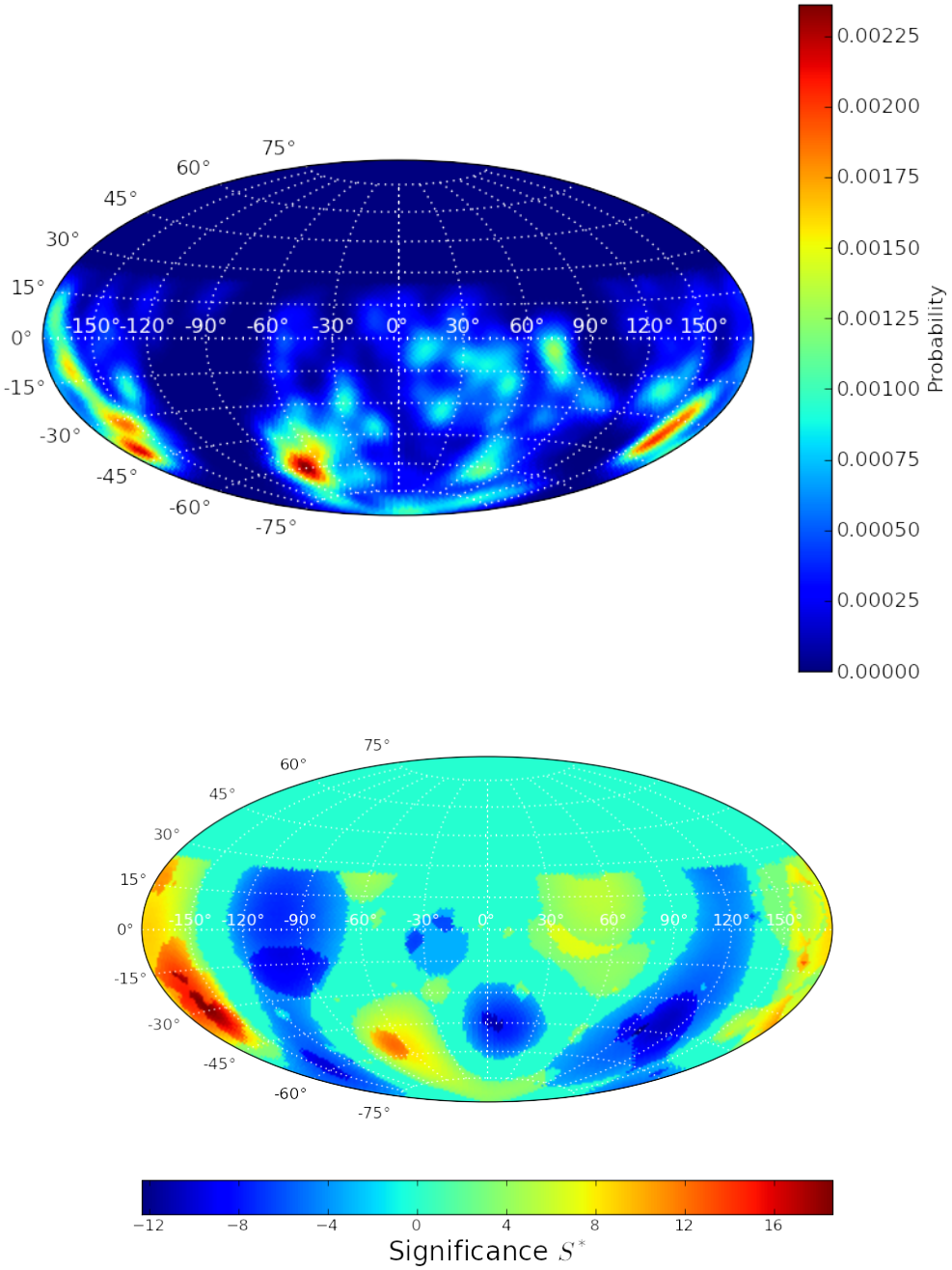

Figure 5.19: Comparison of original source density distribution (top) and the combined threshold result S^* of the needlet scale $j = [0, 5]$ (bottom) shows strong similarity.

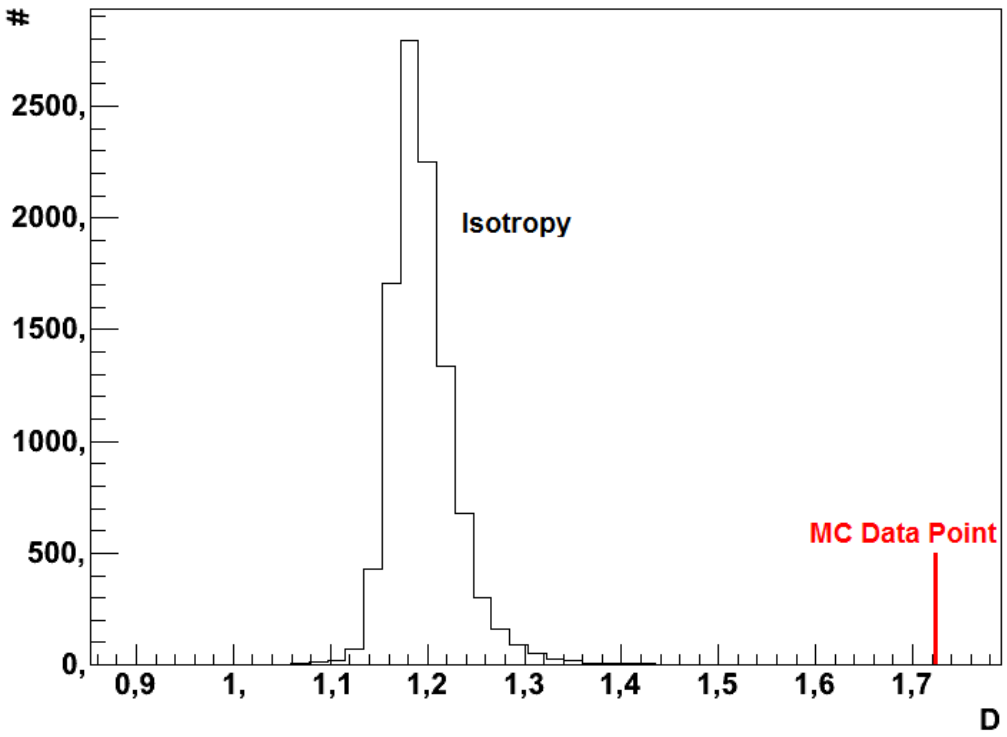

Figure 5.20: Global significance value D for PSCz based ($D = 1.72$) skymap shows that the probability to be compatible with 10000 isotropic Monte Carlo data sets is below 0.0001%.

5.2.3 Point source test

This Monte Carlo point source data set is based on an artificial point source distribution, shown in figure 5.21. In this Monte Carlo sample 4 sources with different smearing and number of events are spread over the southern hemisphere to test the needlet analysis to find multiple sources in case of a weighted exposure. The parameters used for the sources in this analysis are summarized in table 5.3.

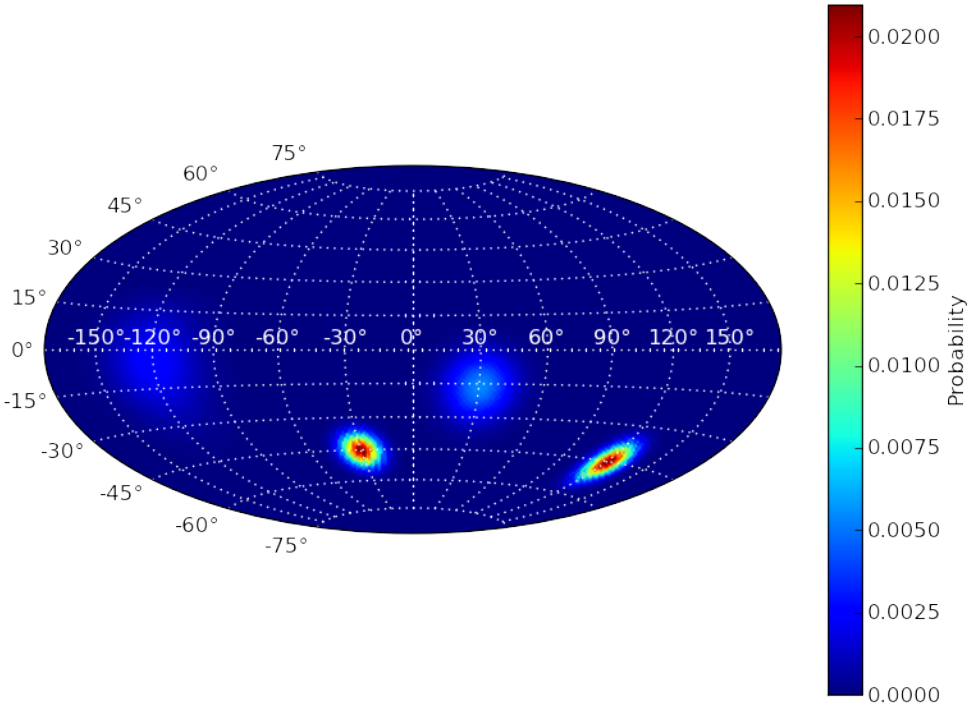

Figure 5.21: Artificial point source distribution used as probability density.

		Source 1	Source 2	Source 3	Source 4
Number of events		100	200	300	100
Smearing		5°	10°	15°	5°
Source position	Right ascension	120°	30°	−120°	−30°
	Declination	−45°	−15°	0°	−45°

Table 5.3: Point source parameters for the artificial point source distribution.

The event-based skymap following from these parameters is completed with additional isotropic noise. The map is shown in figure 5.22. The needlet analysis is applied on this map. The needlet analysis results are shown in figure 5.23 and the results show that only one point source in the scale $j = 1, 2, 3$ is visible. So further filtering is needed to find the other point sources. As the next analysis step the threshold method is applied on the needlet results. In figure 5.24 the results of the

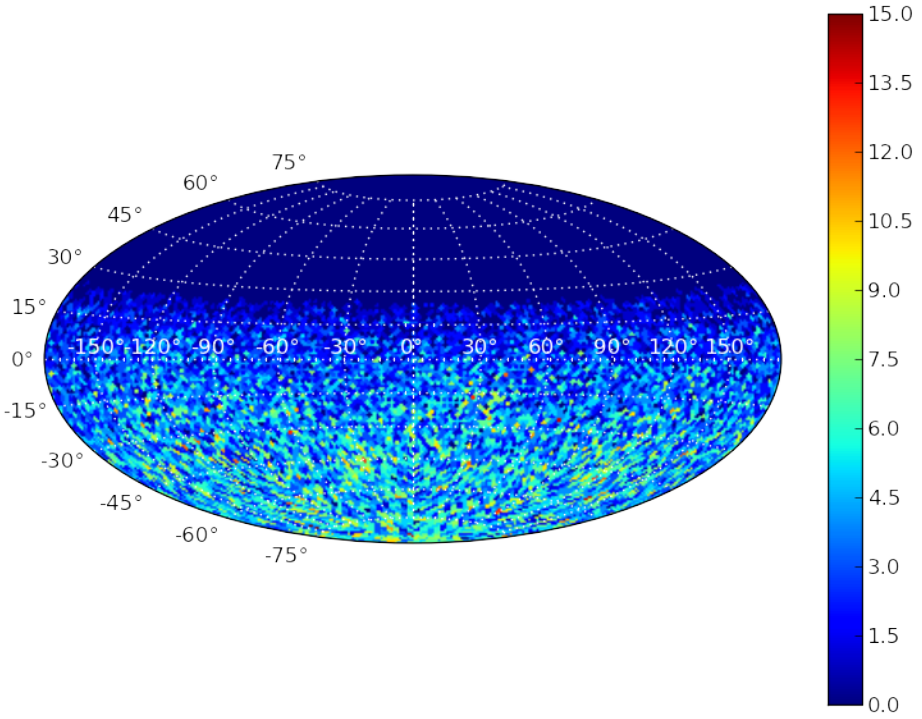

Figure 5.22: Event-based skymap based on an artificial point source distribution with additional isotropic noise (total 30000 events).

threshold method are shown. There the four point sources become visible. The combination of all threshold results is shown in figure 5.25. One can clearly see by eye, that the point sources were found. The accuracy of the reconstruction can be quantified by a simple comparison shown in table 5.4. The pixel with the highest value of S_k^* can be assumed as the equivalent to the center of the point sources. The error of the pixel center derives from the pixel size in the Healpix scheme. However, the global significance still needs to be evaluated. The D value for this scenario shows, that the probability to be compatible with isotropy is below 0.0001%. This value shows, that this point source test sample most certainly is anisotropic and that the significant regions mark the point sources of the Monte Carlo sample. The result of this test example shows, that the needlet analysis is suitable for point source detection and finding anisotropy out of a noise-dominated event sample.

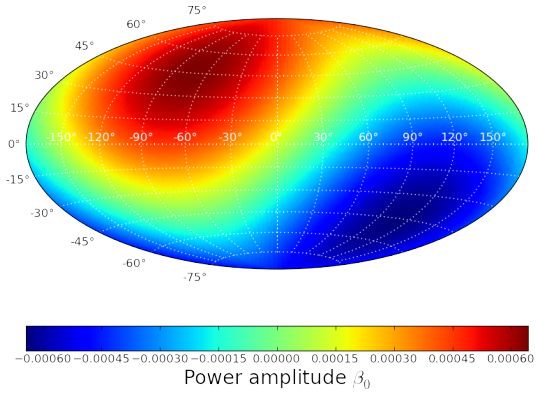

(a) Analysis result at needlet scale $j = 0$

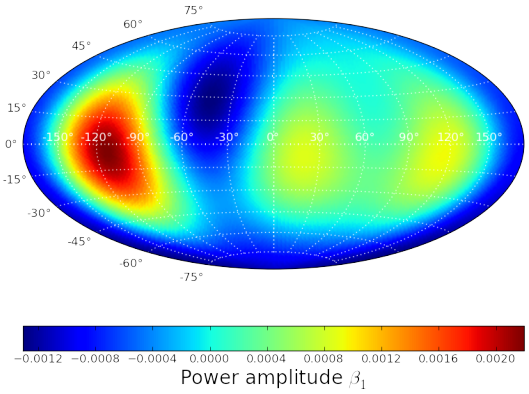

(b) Analysis result at needlet scale $j = 1$

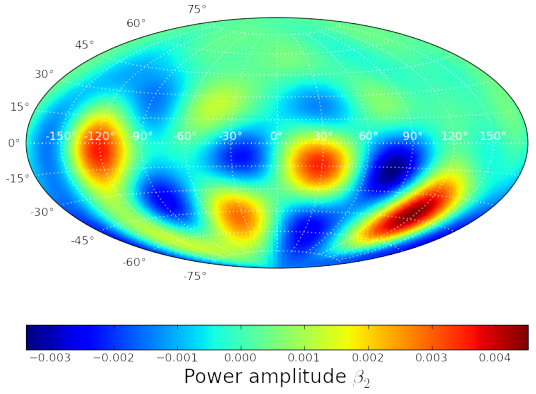

(c) Analysis result at needlet scale $j = 2$

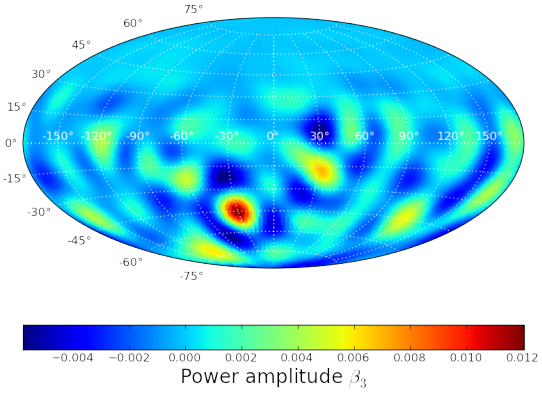

(d) Analysis result at needlet scale $j = 3$

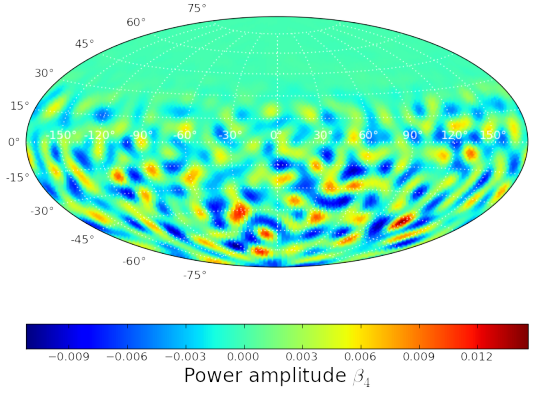

(e) Analysis result at needlet scale $j = 4$

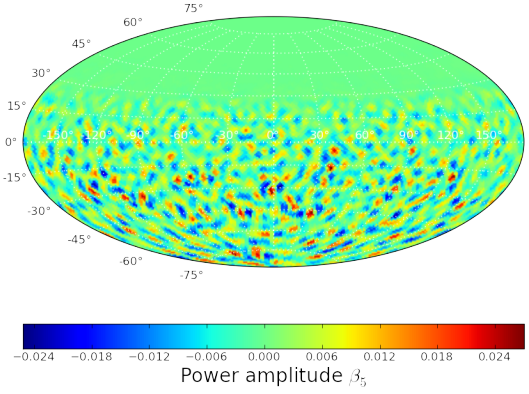

(f) Analysis result at needlet scale $j = 5$

Figure 5.23: Needlet analysis results β_j of artificial point source distribution for various scales j. Further filtering is needed to find the other point sources.

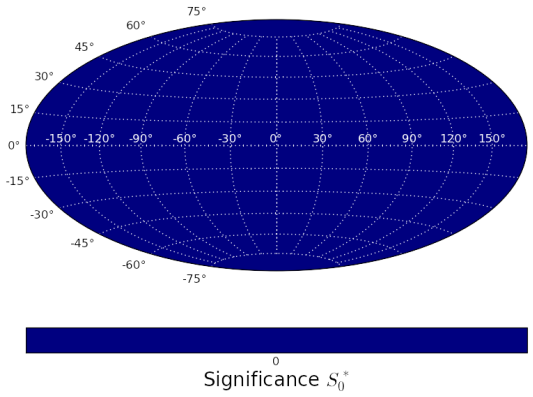

(a) Analysis result at needlet scale $j = 0$

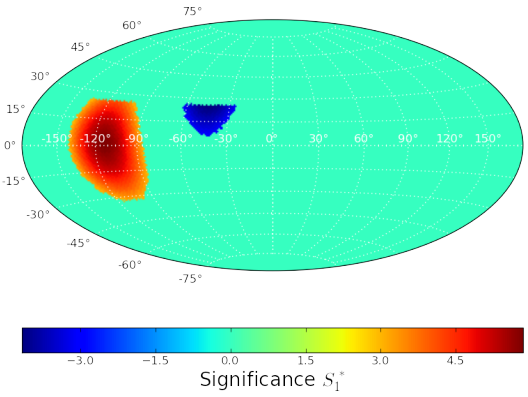

(b) Analysis result at needlet scale $j = 1$

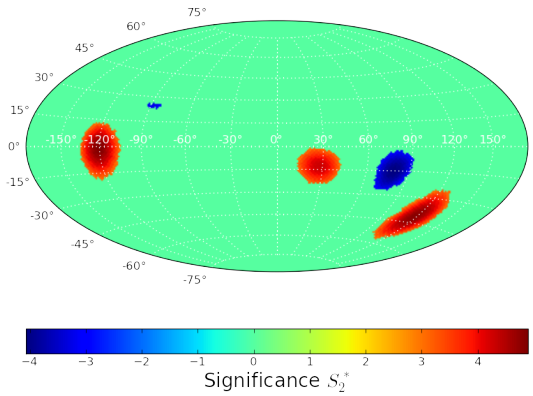

(c) Analysis result at needlet scale $j = 2$

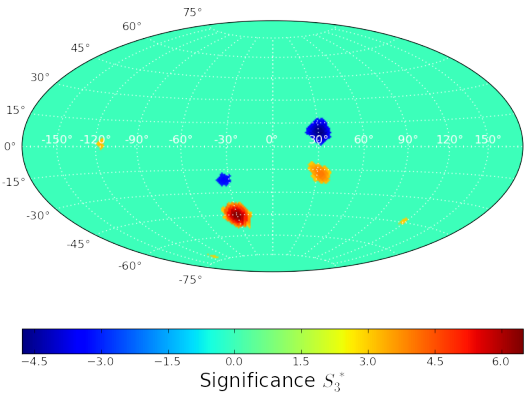

(d) Analysis result at needlet scale $j = 3$

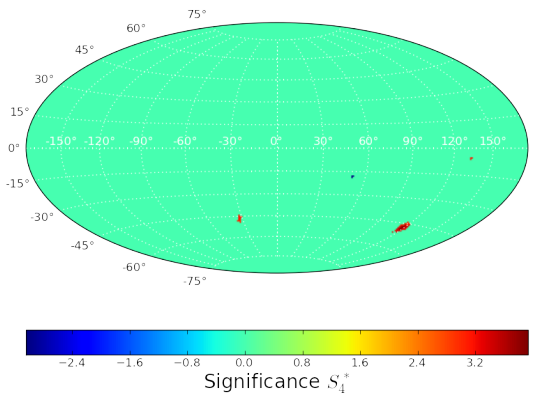

(e) Analysis result at needlet scale $j = 4$

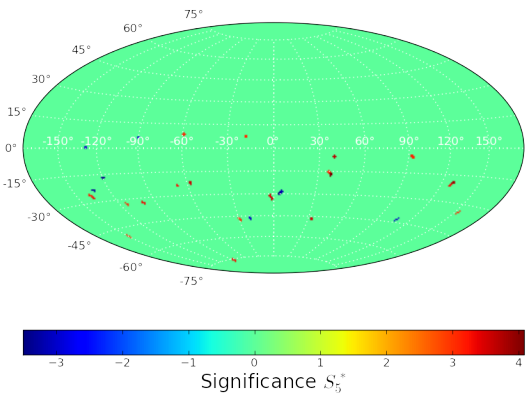

(f) Analysis result at needlet scale $j = 5$

Figure 5.24: Threshold results S_j^* for the artificial point source sample for various scales j. After the threshold cut most of the fluctuations are filtered out and the point sources become visible.

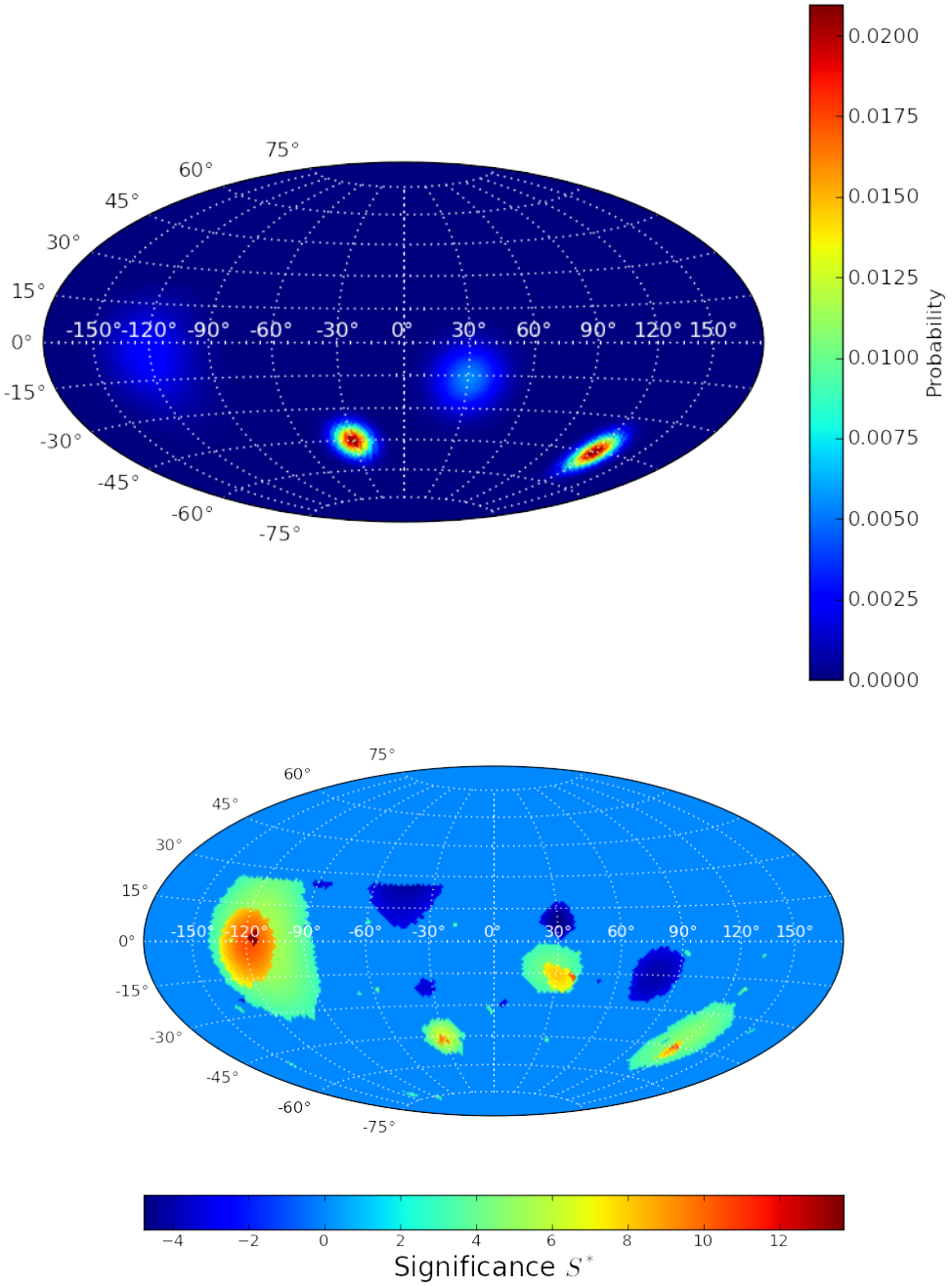

Figure 5.25: Comparison of original source density distribution (top) and the combined threshold result S^* of the needlet scales $j = [0, 5]$ (bottom) shows that all four point sources are found in the correct regions.

Source 1		Set	Reconstructed
Source position	Right ascension	120°	$119 \pm 2°$
	Declination	−45°	$-45 \pm 2°$
Source 2		Set	Reconstructed
Source position	Right ascension	30°	$40 \pm 2°$
	Declination	−15°	$-17 \pm 2°$
Source 3		Set	Reconstructed
Source position	Right ascension	−120°	$-117 \pm 2°$
	Declination	0°	$4 \pm 2°$
Source 4		Set	Reconstructed
Source position	Right ascension	−30°	$-31 \pm 2°$
	Declination	−45°	$-46 \pm 2°$

Table 5.4: Comparison of set point source positions with the reconstructed positions.

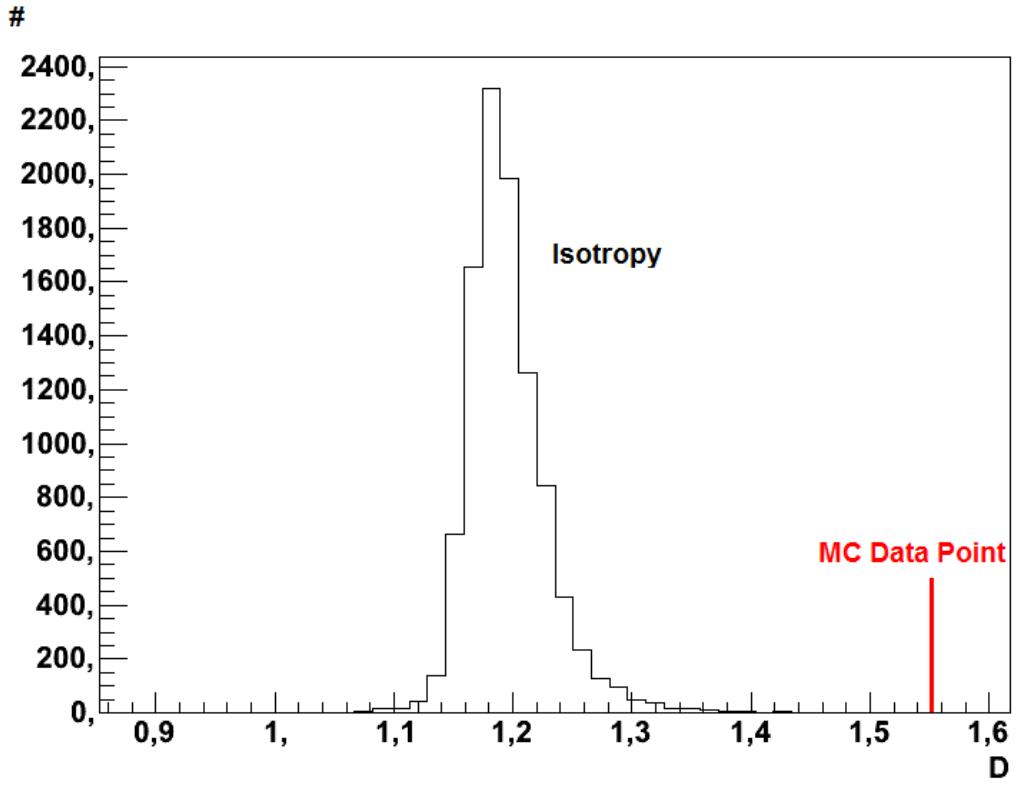

Figure 5.26: Global significance value D for the point source Monte Carlo sample ($D = 1.553$) shows, that the probability to be compatible with the 10000 isotropic Monte Carlo data sets is below 0.0001%.

6. Applying the anisotropy study on the arrival directions of UHECRs measured by the Pierre Auger Observatory

In this chapter the analysis described in the previous chapter is applied to air shower data measured by the Pierre Auger Observatory to determine whether there is an anisotropy in the arrival direction of UHECR. The data sample selection will be described and also corrections on the reconstructed data will be applied. These corrections are necessary to eliminate false anisotropy effects, before the needlet analysis is preformed.

6.1 Local effects

The local detector effects considered in this thesis are the effects of the atmospheric conditions at the Pierre Auger Observatory, which are the seasonal effect on the event trigger rate and the influence of the Earth's magnetic field on the development of an EAS, which cause a declination dependent effect on the energy estimator.

6.1.1 Atmospheric condition correction

The development of an air shower depends on the atmospheric condition at the ground detector. The impact of these conditions on the energy estimator $S(1000)$ of the SD array was shown in [AP09]. The signal $S(1000)$ measured with the SD at 1 km from the shower core impact position is correlated with local values of pressure P and air density ρ. Using the average values $P_0 = 862\,\mathrm{hPa}$ and $\rho_0 = 1.06\,\mathrm{kgm}^{-3}$ at the location of the observatory as a reference, the signal $S^0(1000)$ that would have been measured at these reference values can be calculated by

$$S^0(1000) = [1 - \alpha_P(\theta)(P - P_0) - \alpha_\rho(\theta)(\rho_d - \rho_0) - \beta_\rho(\theta)(\rho_d - \rho_0)]S(1000)\,, \quad (6.1)$$

where ρ_d is the daily average air density at the time of the measurement of the air shower and θ is the zenith angle. The correlation coefficients α_P, α_ρ and β_ρ are reported in [AP09]. A comparison of the event trigger rate of the corrected and uncorrected data with a minimal energy cut $E_{min} > 3\,\mathrm{EeV}$ is shown in figure 6.1. In this case the trigger rate for this analysis is depending on the right ascension.

This systematic effect needs to be corrected in the exposure of the Pierre Auger Observatory, otherwise there will be a false dipole shaped anisotropy, caused by the seasonal changes of the atmosphere.

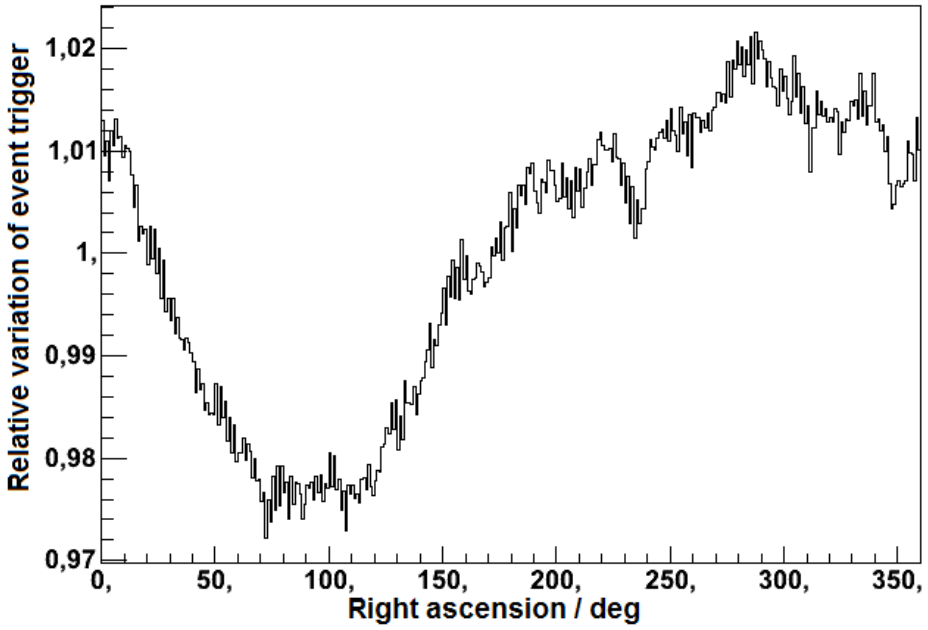

Figure 6.1: Relative trigger-rate at the PAO from the correction for atmospheric parameters against the right ascension.

6.1.2 Geomagnetic field effect

The charged secondary particles of a cosmic ray air shower are deflected by the magnetic field of the Earth. Therefore, the lateral footprint measured by the SD array is changed and so the energy estimator $S(1000)$. A scheme of the effect is shown in figure 6.2. This effect causes an overestimation of the energy for showers, coming from the south, whereas shower from the north are reconstructed with a lower energy. This causes a chance of the event trigger rate of the order of $\approx 2\%$ depending on the declination, and so will induce a false anisotropy, if an energy cut is applied. Therefore, the reconstructed energy of an air shower needs to be corrected for this effect. The correction is according to [Gri11] given by

$$S_{off} = S_{on}\left(1 + R_B \frac{sin^2(\Omega_B)\cdot cos^n(\theta_B)}{cos^n(\theta)}\right), \tag{6.2}$$

with the fitted parameters R_B and n reported in [Gri11], the angle $\Omega_B = \angle(\mathbf{S}, \mathbf{B})$ between the shower direction $\mathbf{S}$ and the local direction of the B-field $\mathbf{B}$ and the angle θ_B, which denotes the zenith angle of the geomagnetic field and the zenith angle of the shower θ. The effect is constant in time and so it does not affect the right ascension distribution.

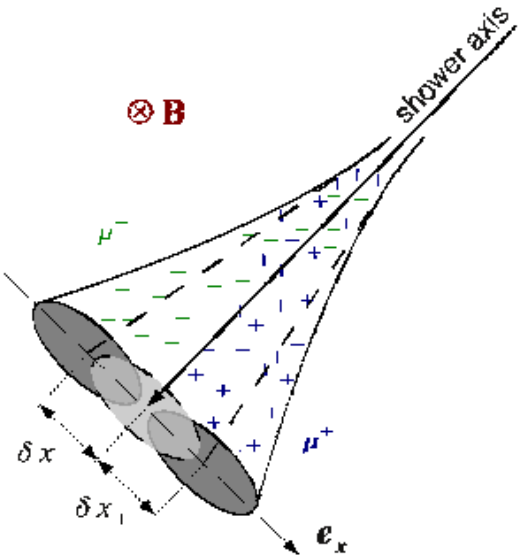

Figure 6.2: Separation of charged air shower particles in the Earth's magnetic field B: Muons $\mu^{\pm}$ are deflected by δx on average according to their respective charge, the originally circular footprint of the lateral particle densities in the shower front becomes distorted. [Gri11]

6.1.3 Data selection

The data used for this thesis were reconstructed with the Offline-Software-Reconstruction version v2r7p4. The data taking period includes all available continuously reconstructed data. The minimal energy and the maximal zenith angle denote the full trigger efficiency for the Pierre Auger Observatory. The T5 trigger denotes a high quality SD reconstruction, with at least 5 working stations around the tank with the highest signal. Bad periods are time intervals, when the detector can not reconstruct air showers, due to maintenance or detector failure (for details see [Gri11]).
The data selection used in this thesis are shown in table 6.1 with the uncorrected energy estimator and in table 6.2 with the corrected energy estimator.

Data taking period	01. January 2004 - 28. February 2011
Minimal energy	3 EeV
Maximal zenith	60°
T5 trigger	True
Exclude bad periods	True
→	43383 Events

Table 6.1: Auger data selection with the uncorrected energy estimator.

Data taking period	01. January 2004 - 28. February 2011
Minimal energy	3 EeV
Maximal zenith	60°
T5 trigger	True
Exclude bad periods	True
→	38340 Events

Table 6.2: Auger data selection with the correction of the energy estimator.

Another corrected data sample is selected with an additional 10 EeV minimal energy cut to look for anisotropy in the arrival directions of the highest energy cosmic rays. The data selection for this high energy sample is shown in table 6.3.

Data taking period	01. January 2004 - 28. February 2011
Minimal energy	10 EeV
Maximal zenith	60°
T5 trigger	True
Exclude bad periods	True
→	4919 Events

Table 6.3: Auger data selection with the correction of the energy estimator with an additional 10 EeV minimal energy cut.

6.2 Applying the needlet analysis on the data taken by the Pierre Auger Observatory

The three selected data sets are now converted into data skymaps. The arrival directions of the UHECRs are given in the equatorial coordinates system. For a better orientation in the skymap an overlay with the position of four possible UHECR sources is added to all skymap plots. These point sources are AGN Centaurus A, Sagittarius A*, which is a radio source in the galactic center, the Virgo Cluster, which is a cluster of galaxies, and the Crab Nebula, which is a supernovae remnant.

6.2.1 Data sample with uncorrected energy estimator

The first data set consists of the arrival directions of the UHECRs with the uncorrected energy estimator. The data skymap is shown in figure 6.3. The needlet

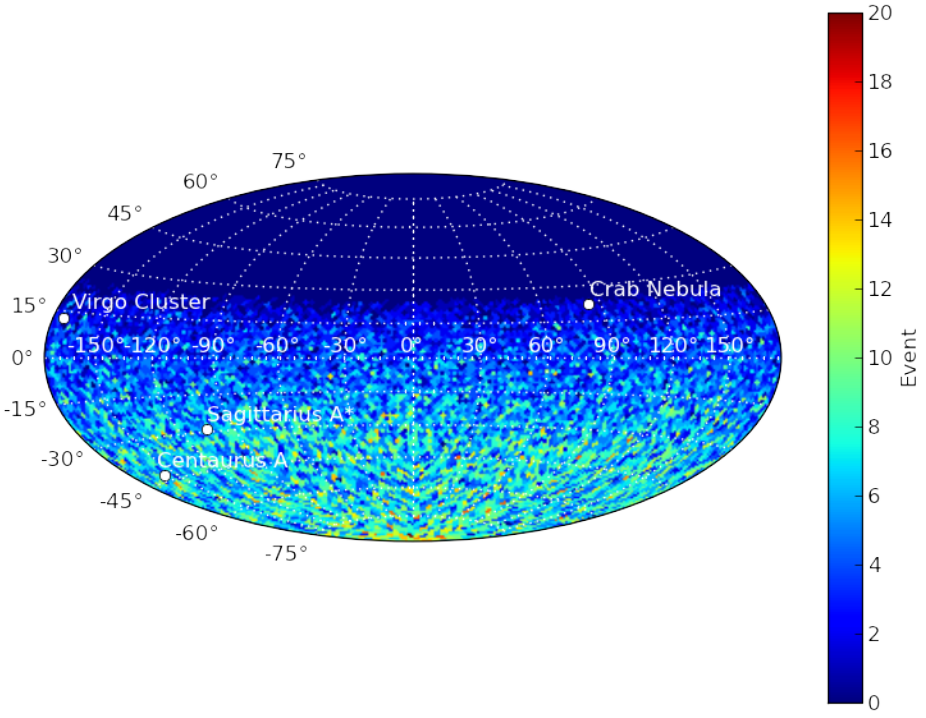

Figure 6.3: Arrival directions of the Auger data set with the uncorrected energy estimator are plotted in the Healpix scheme. The number of events is 43383.

analysis is applied on the data skymap considering the geometrical exposure of the Pierre Auger Observatory. The results for the power amplitude β_{jk} are shown in figure 6.4. The results need more filtering to determine the significant structures. As the next step the threshold method is applied on the needlet analysis results. 10000 isotropic Monte Carlo skymaps with the same number of events as the Auger data set are used to determine the significance of each pixel. The isotropic source density distribution is based on the geometrical exposure. The threshold method results are shown in figure 6.5. There are large scale structures in the needlet scale

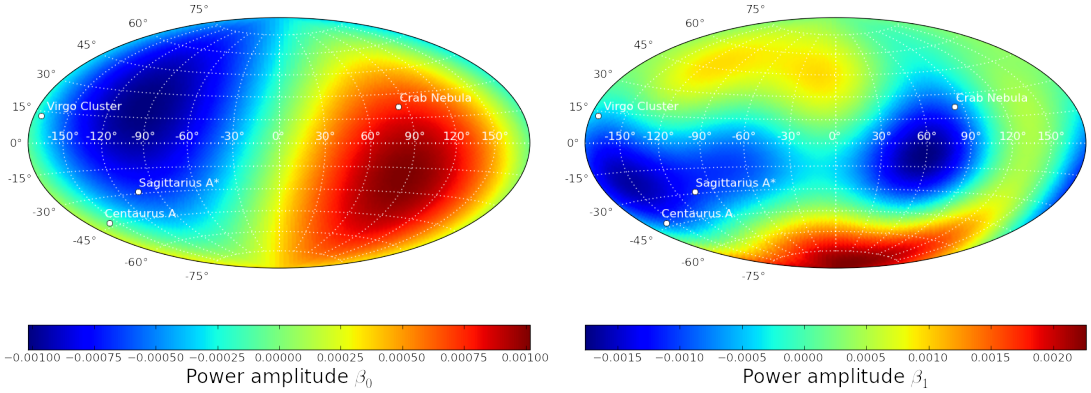

(a) Result at needlet scale $j = 0$

(b) Result at needlet scale $j = 1$

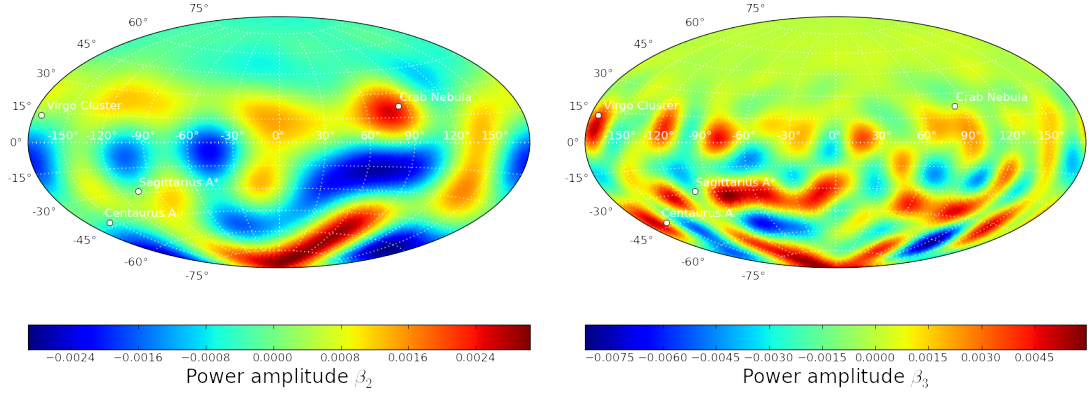

(c) Result at needlet scale $j = 2$

(d) Result at needlet scale $j = 3$

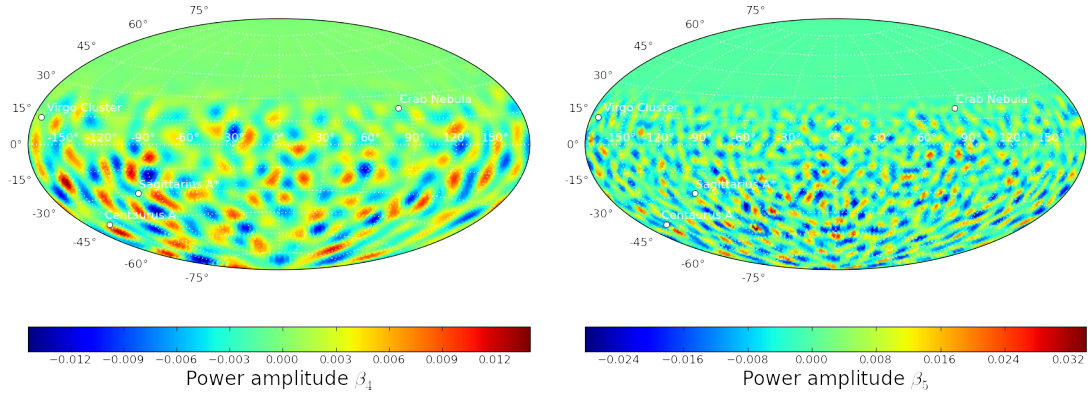

(e) Result at needlet scale $j = 4$

(f) Result at needlet scale $j = 5$

Figure 6.4: The power amplitude β_j of the needlet analysis on the arrival directions of the UHECRs of the Pierre Auger Observatory is shown for different needlet scales j.

$j = 0$, that are marked as significant and a structure similar to a point source in the needlet scale $j = 2$ at the position of the Crab Nebula. In the needlet scale $j = 1$ there is a large structure at the south pole visible and also 2 regions with under

fluctuation. In the needlet scale $j = 3$ there is a small structure in the region of the Virgo Cluster and a small under fluctuation. In the threshold results S^*_{jk} of needlet scales $j = 4, 5$ no structures are visible. In the next step the threshold results S^*_j are summed to get the combined threshold result S^*, which is shown in figure 6.6. The combined threshold result S^* shows the features of the each needlet scale j, but no strong point source or large scale structures, like in the MC test scenarios of the previous chapter. As the last step of this analysis the global significance value D is computed. The D value is shown in figure 6.7 in comparison to the D value of 10000 isotropic Monte Carlo data sets. The result of the global significance value $D = 1.158$ shows, that the Auger data sample is very good compatible with isotropy. This data set is compatible with 92.52% of the 10000 isotropic MC data sets and so no clear evidence of anisotropy was found. However, the small and large structures should be investigated, if they still exists in the corrected energy data sample. Therefore, the next step is the analysis of the energy corrected data sample.

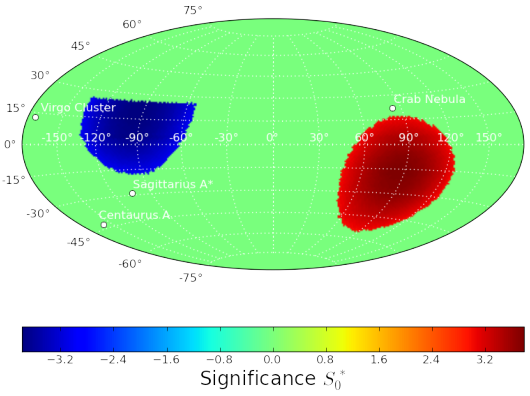

(a) Threshold result at needlet scale $j = 0$

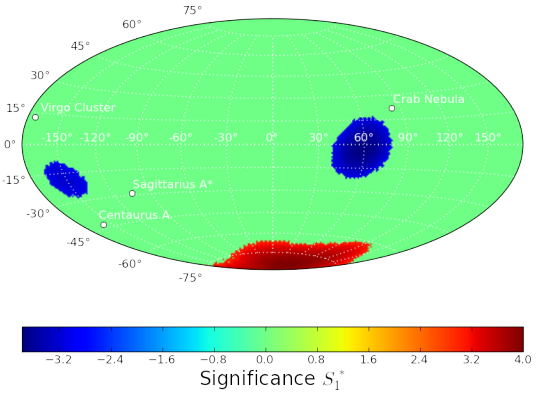

(b) Threshold result at needlet scale $j = 1$

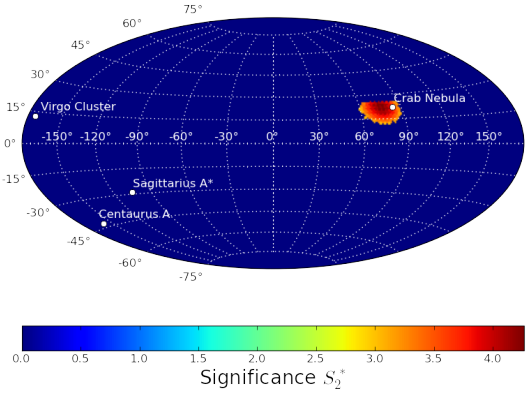

(c) Threshold result at needlet scale $j = 2$

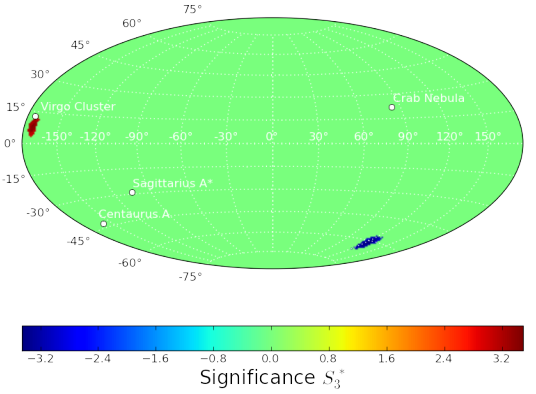

(d) Threshold result at needlet scale $j = 3$

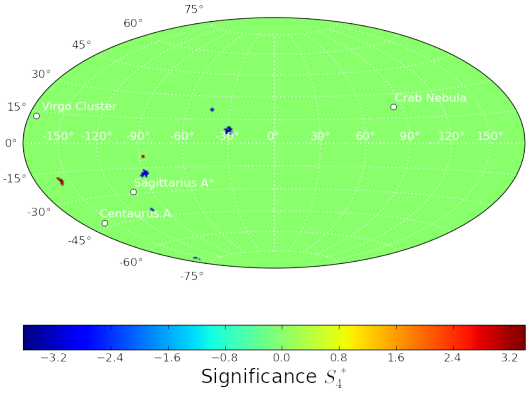

(e) Threshold result at needlet scale $j = 4$

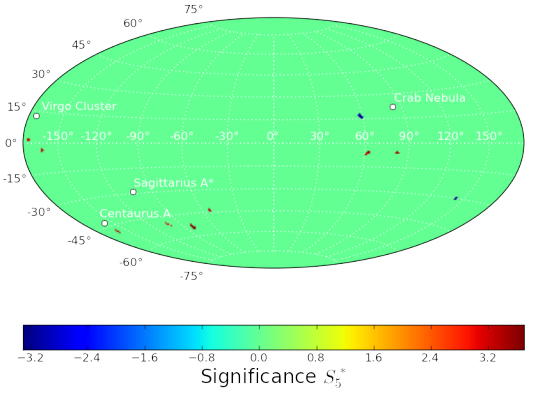

(f) Threshold result at needlet scale $j = 5$

Figure 6.5: The threshold results S^*_{jk} are shown for the needlet analysis result. There are a large scale structures in the needlet scale $j = 0$, that are marked as significant and a structure similar to a point source in the needlet scale $j = 2$ at the position of the Crab Nebula. In the needlet scale $j = 1$ there is a large structure at the south pole visible and also 2 regions with under fluctuation. In the needlet scale $j = 3$ there is a small structure in the region of the Virgo Cluster and a small under fluctuation.

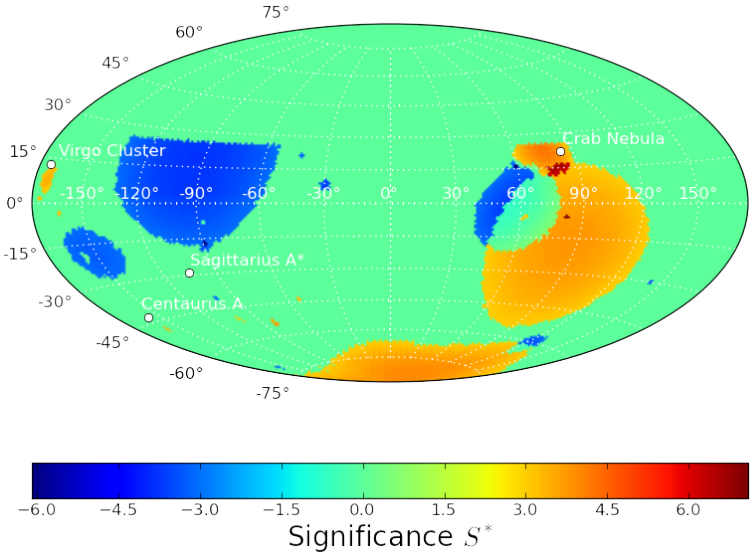

Figure 6.6: Combined threshold result S^* shows the features of the each needlet scale j, but no strong point source or large scale structures.

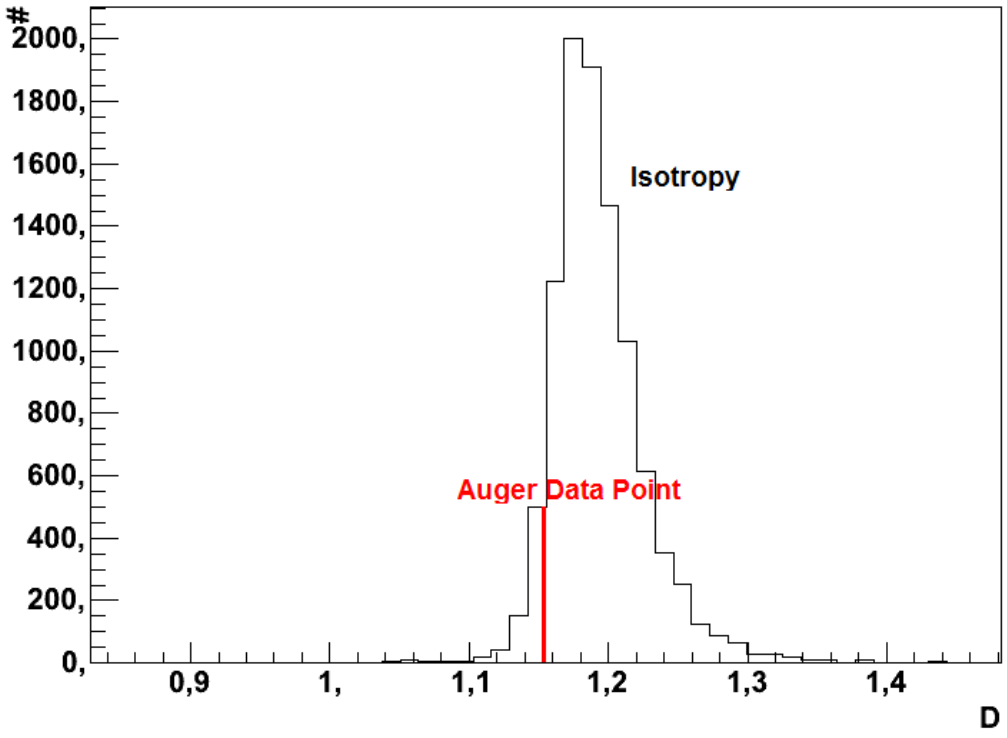

Figure 6.7: Global significance value $D = 1.158$ of the combined threshold result S^* in comparison to the D value of 10000 isotropic Monte Carlo data set. This data set is compatible with 92.52% of the 10000 isotropic MC data sets. So no clear evidence of anisotropy was found.

6.2.2 Data sample with corrected energy estimator

The second data set consists of the arrival directions of the UHECRs with the corrected energy estimator. The data skymap is shown in figure 6.8. The needlet

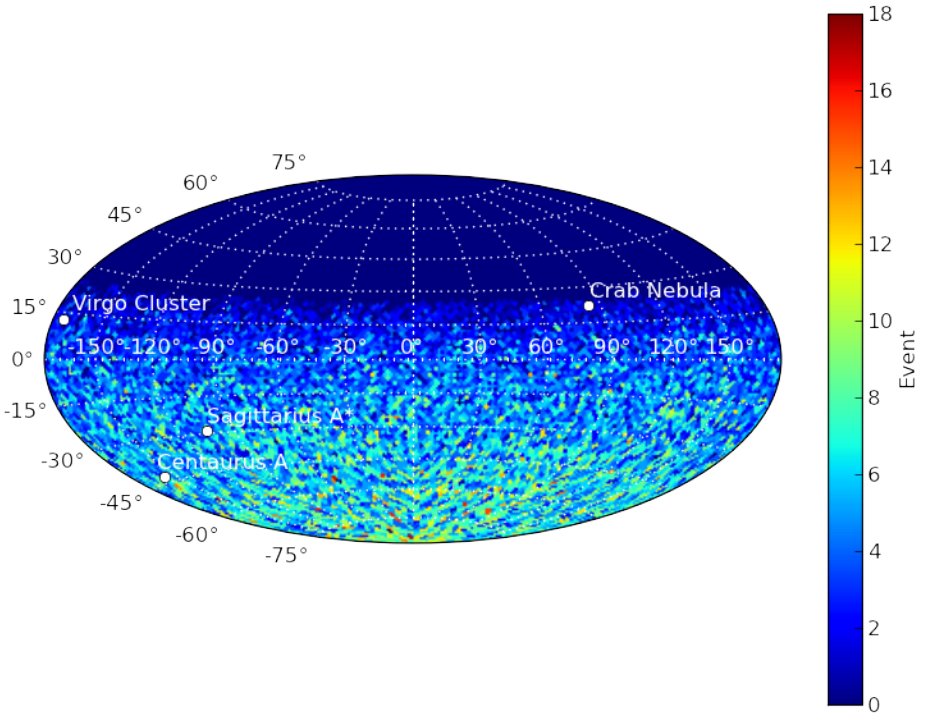

Figure 6.8: Arrival directions of the Auger data set with the corrected energy estimator are plotted in the Healpix scheme. The number of events is 38340.

analysis is applied to this skymap considering the geometrical exposure of the Pierre Auger observatory and the right ascension depending local effects. The results for the power amplitude β_{jk} are shown in figure 6.9. The results need more filtering to determine the significant structures. As the next step the threshold method is applied on the needlet analysis results. 10000 isotropic Monte Carlo skymaps with the same number of events as the Auger data set are used to determine the significance of each pixel. The isotropic source density distribution is based on the geometrical exposure and the right ascension depending local effects of the atmospheric correction. The threshold method results S_j^* are shown in figure 6.10. The threshold results S_{jk}^* of the needlet scale $j = 1$ shows a large structure in the south pole region and also a under fluctuation. The threshold results S_{jk}^* of the needlet scale $j = 2$ shows 3 structures and a under fluctuation. The significant structures are in the south pole region, near the Crab Nebula and the other is near the equator. There are no significant regions in the needlet scale $j = 0$ and in the threshold results S_{jk}^* of needlet scales $j = 3, 4, 5$ no structures are visible. In the next step the threshold results S_j^* are summed to get the combined threshold result S^*, which is shown in figure 6.11. The structures in the south pole region and at the equator can be a hint for an excess in the cosmic ray arrival directions. As the last step of this analysis

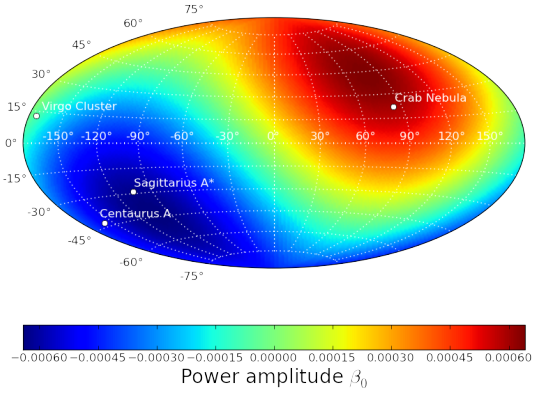

(a) Result at needlet scale $j = 0$

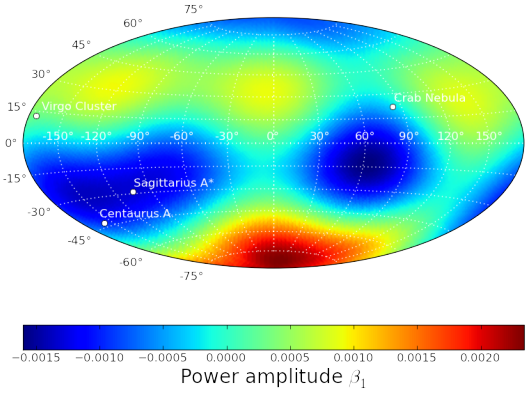

(b) Result at needlet scale $j = 1$

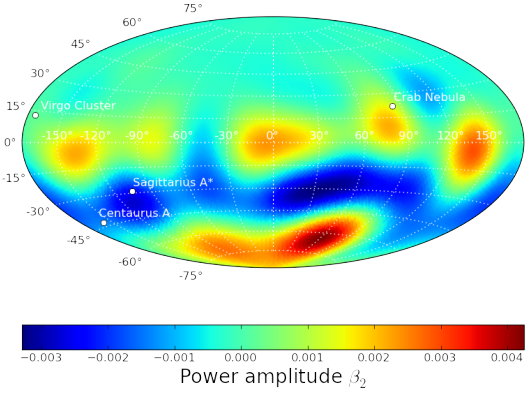

(c) Result at needlet scale $j = 2$

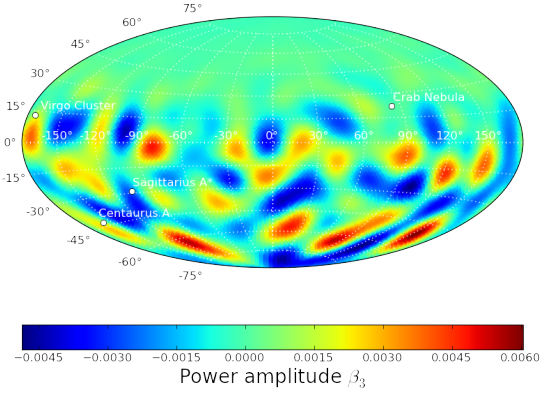

(d) Result at needlet scale $j = 3$

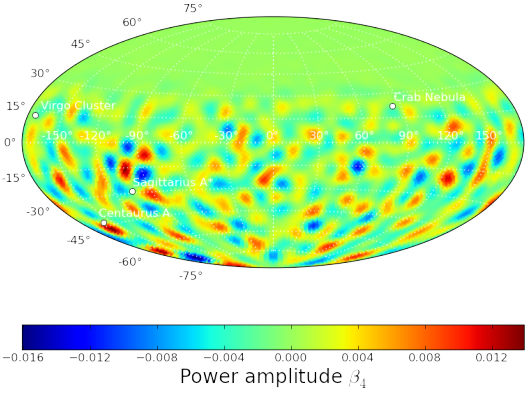

(e) Result at needlet scale $j = 4$

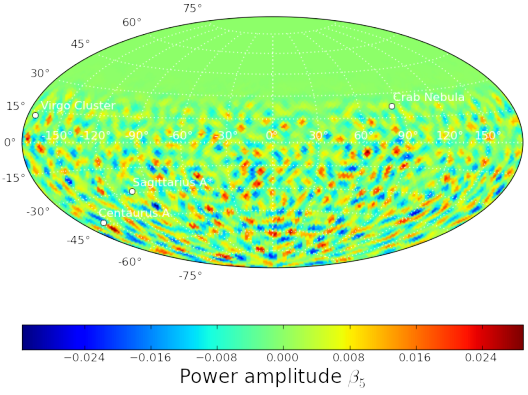

(f) Result at needlet scale $j = 5$

Figure 6.9: The power amplitude β_j of the needlet analysis on the arrival directions of the UHECRs of the Pierre Auger Observatory is shown for different needlet scales j. The results needed more filtering to determine the significant structures.

the global significance value D is computed. The D value is shown in figure 6.12 in comparison to the D value of 10000 isotropic Monte Carlo data sets. The result of the global significance value D shows, that the probability of this data set to be

compatible with isotropy is 1.72% and so no clear evidence of anisotropy was found. However, there is a sign of an excess of events, coming from the south and 2 point source regions one near the equator the other one near the Crab Nebula, so this needs futher investigations and verification. In the next step the data sample with the 10 EeV minimal energy cut is analyzed.

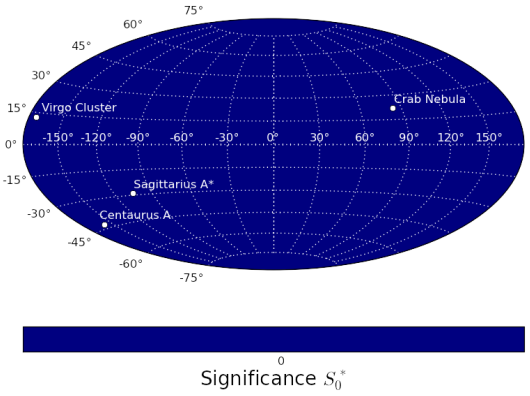

(a) Threshold result at needlet scale $j = 0$

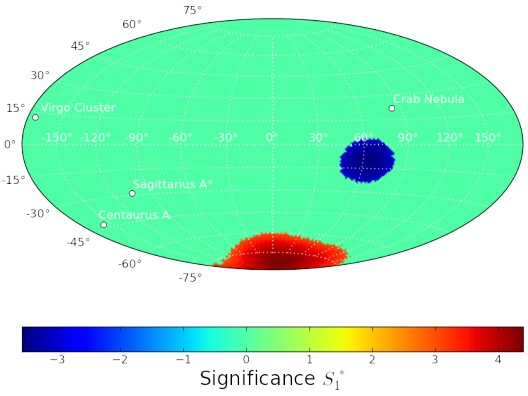

(b) Threshold result at needlet scale $j = 1$

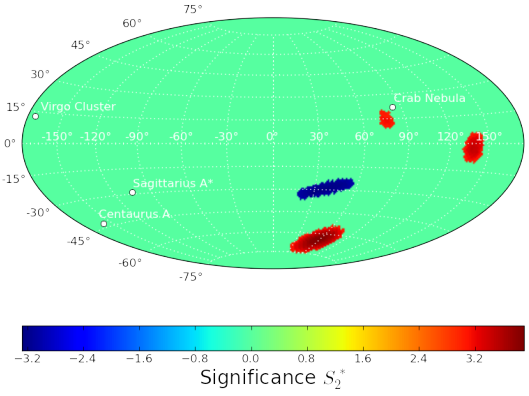

(c) Threshold result at needlet scale $j = 2$

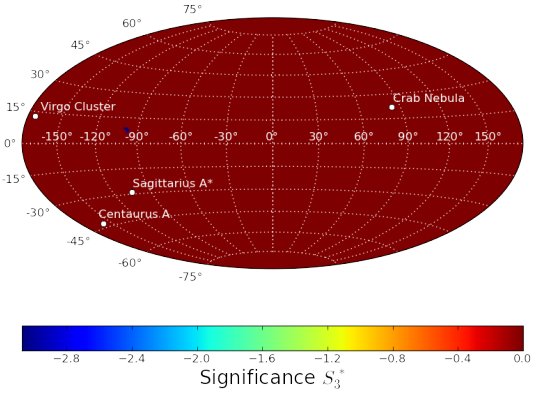

(d) Threshold result at needlet scale $j = 3$

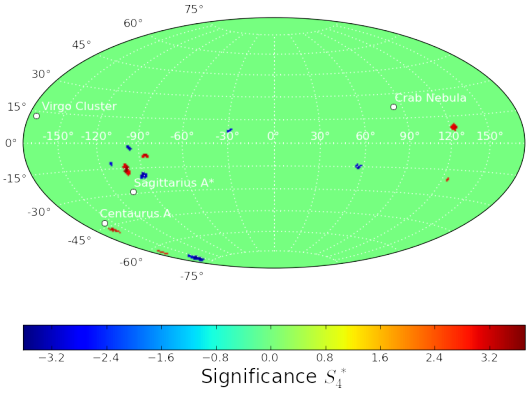

(e) Threshold result at needlet scale $j = 4$

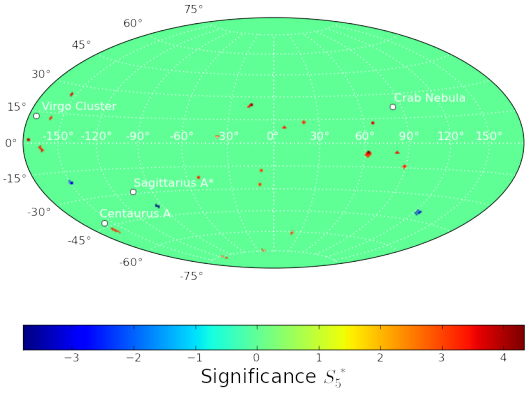

(f) Threshold result at needlet scale $j = 5$

Figure 6.10: The threshold results S^*_{jk} of the needlet scale $j = 1$ shows a large structure in the South pole region and also a under fluctuation. The threshold results S^*_{jk} of the needlet scale $j = 2$ shows 3 structures and a under fluctuation. The significant structures are in the South pole region, near the Crab Nebula and the other is near the equator. There are no significant regions in the needlet scale $j = 0$ and in the threshold results S^*_{jk} of needlet scales $j = 3, 4, 5$ no structures are visible.

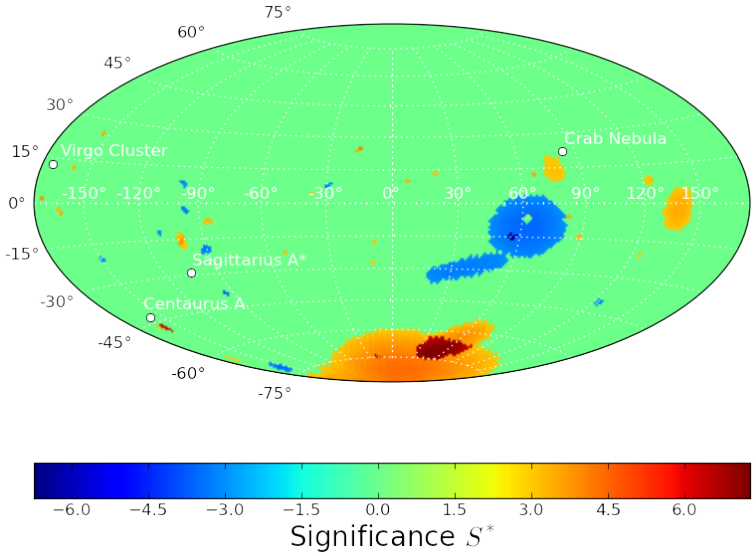

Figure 6.11: Combined threshold result S^* from the data with the corrected energy estimator. The structures in the south pole region and at the equator can be a hint for an excess in the cosmic ray arrival directions.

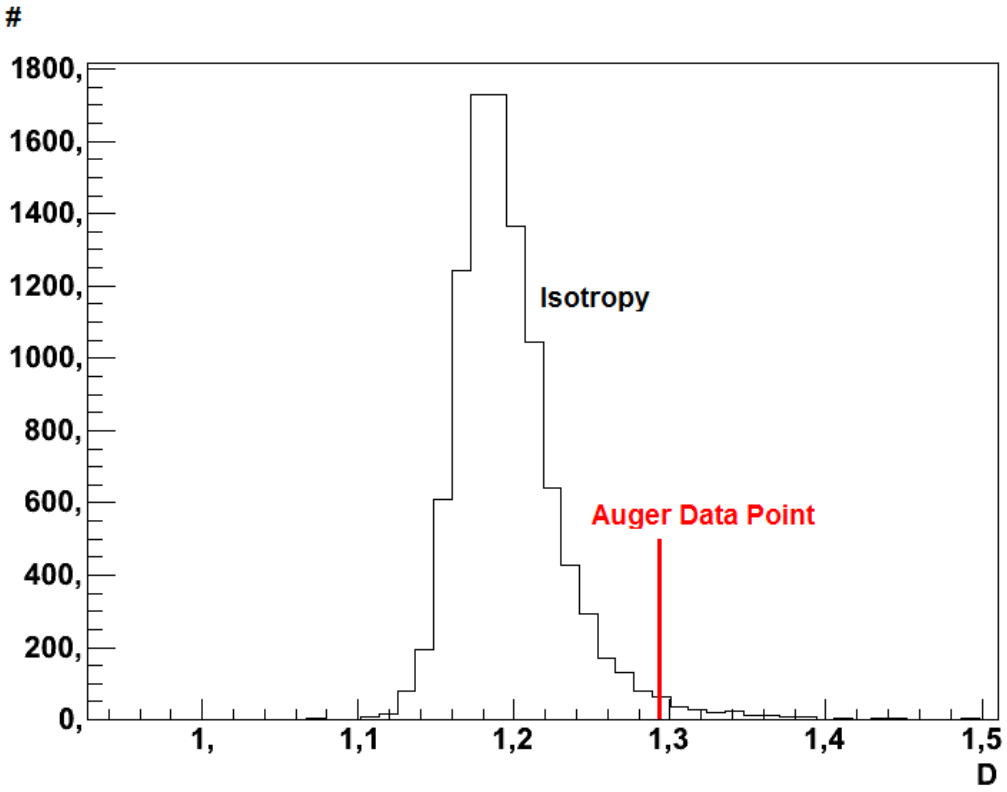

Figure 6.12: Significance value D of the threshold result ($D = 1.293$) from the data compared to the D value of 10000 isotropic Monte Carlo data sets. The probability of this data set to be compatible with isotropy is 1.72%.

6.2.3 Data sample with corrected energy estimator and an additional minimal energy cut of 10 EeV

The last data set consists of the arrival directions of the UHECRs with the corrected energy estimator and an additional minimal energy cut of 10 EeV. In this data the UHECRs are less deflected by the galactic and the extragalactic magnetic field. So in this data sample the UHECRs should nearly point back to the source regions. However, the statistic is in comparison to the first two data sample low due to the power law of the energy spectrum. The data skymap is shown in figure 6.13. The needlet analysis is applied on this skymap considering the geometrical exposure

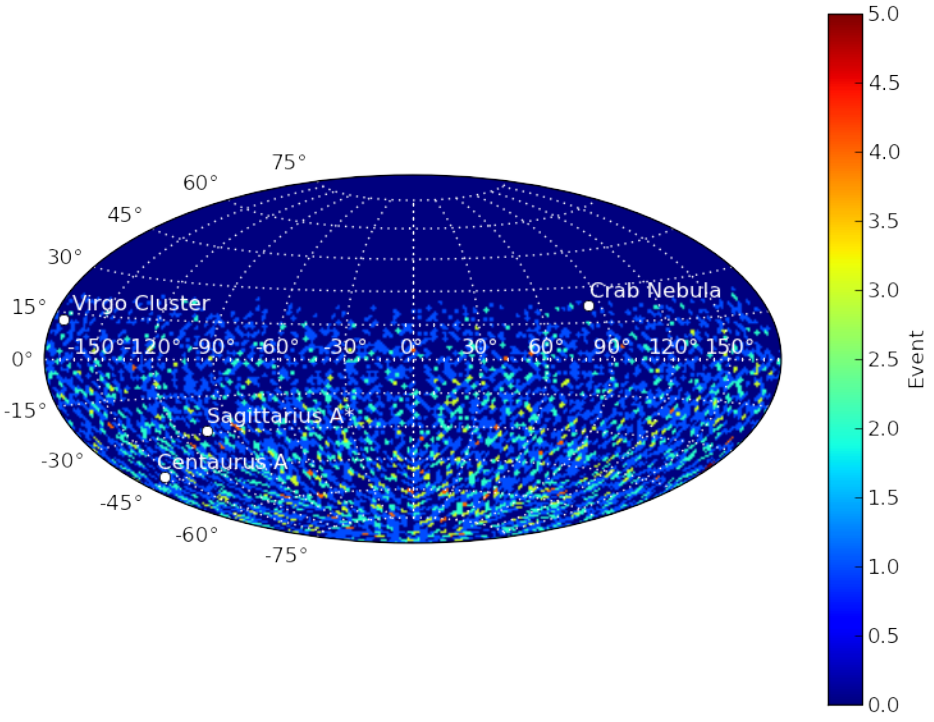

Figure 6.13: Arrival directions of the Auger data set with the uncorrected energy estimator are plotted in the Healpix scheme. The number of events is 4919.

of the Pierre Auger observatory and the right ascension depending local effects.. The results are shown in figure 6.14. The results need more filtering to determine the significant structures. As the next step the threshold method is applied on the needlet analysis results. 10000 isotropic Monte Carlo skymaps with the same number of events as the Auger data set are used to determine the significance of each pixel. The isotropic source density distribution is based on the geometrical exposure and the right ascension depending local effects of the atmospheric correction. The threshold method results S_j^* are shown in figure 6.15. There are no significant regions in the threshold results S_{jk}^* of the needlet scale $j = 0, 1, 2$ and in the threshold results S_{jk}^* of needlet scales $j = 3, 4, 5$ no structures are visible. In the next step the threshold results S_j^* are summed to get the combined threshold result S^*, which is shown in figure 6.16. No significant regions were found. As the last step of this

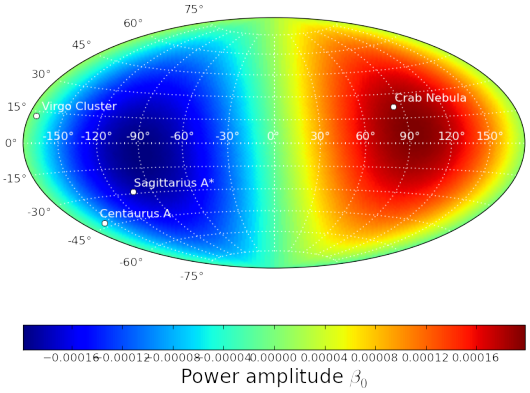

(a) Result at needlet scale $j = 0$

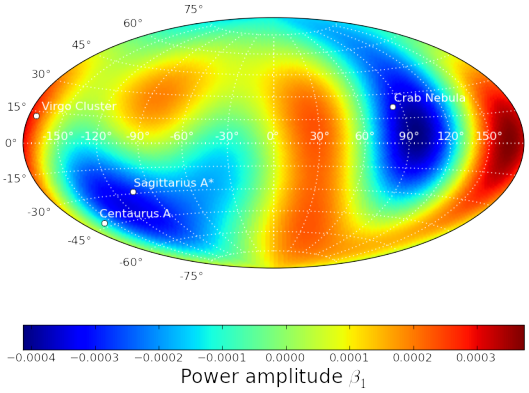

(b) Result at needlet scale $j = 1$

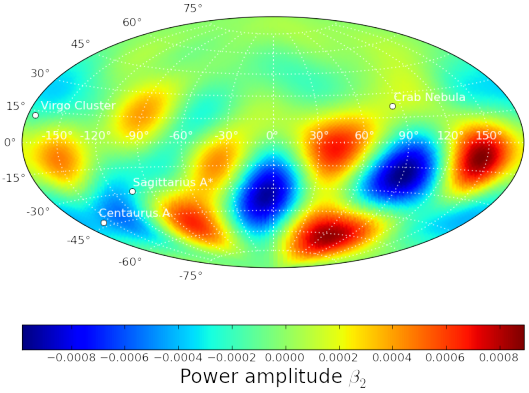

(c) Result at needlet scale $j = 2$

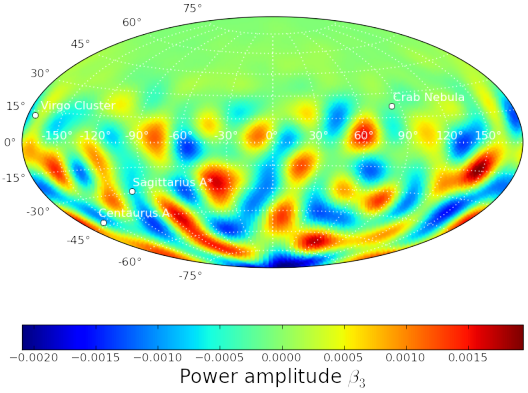

(d) Result at needlet scale $j = 3$

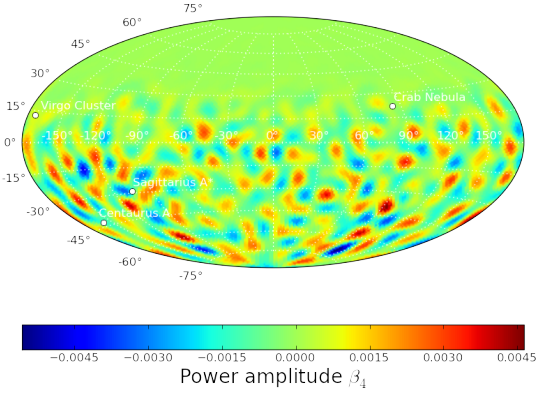

(e) Result at needlet scale $j = 4$

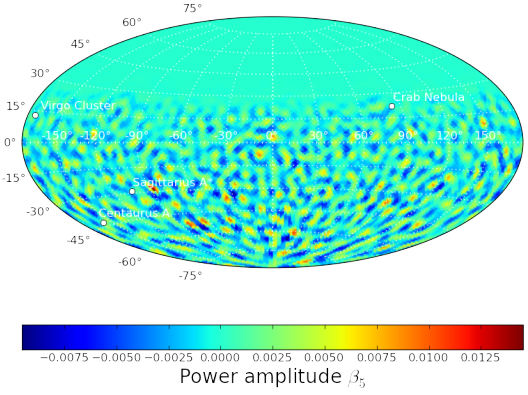

(f) Result at needlet scale $j = 5$

Figure 6.14: The power amplitudes β_j of the needlet analysis on the arrival directions of the UHECRs of the Pierre Auger Observatory are shown for different needlet scales j.

analysis the global significance value D is computed. The D value is shown in figure 6.17 in comparison to the D value of 10000 isotropic MC data sets. The global significance value D shows that the result of the combined threshold result S^* is

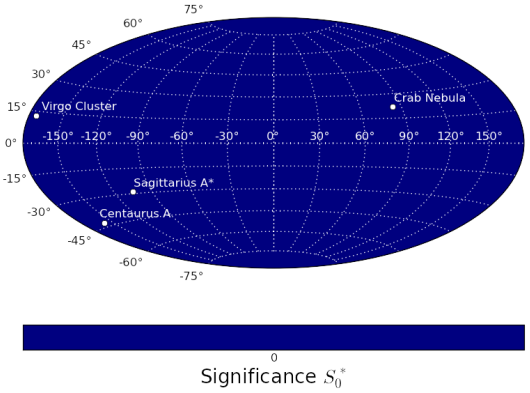

(a) Threshold result at needlet scale $j = 0$

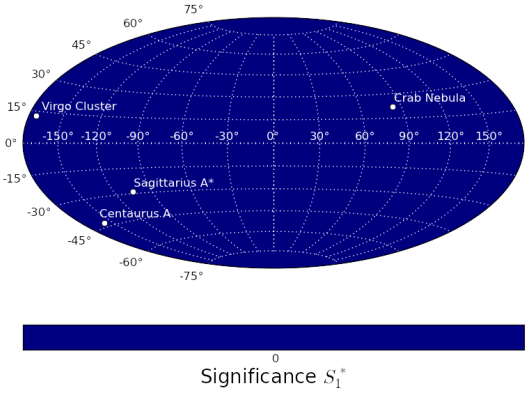

(b) Threshold result at needlet scale $j = 1$

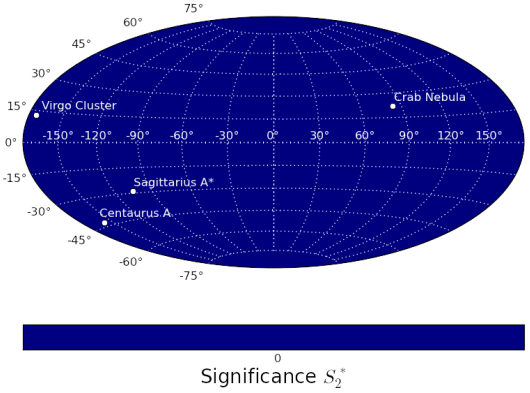

(c) Threshold result at needlet scale $j = 2$

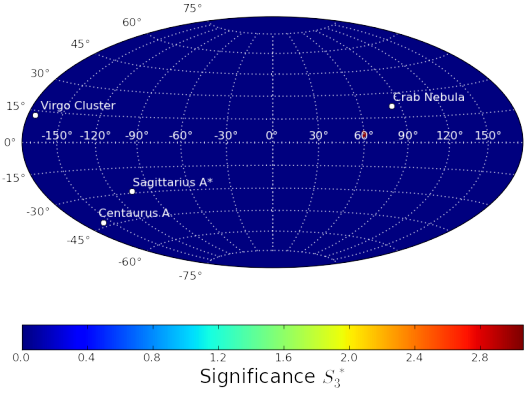

(d) Threshold result at needlet scale $j = 3$

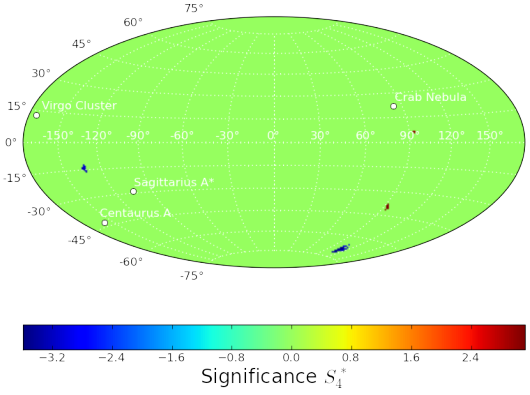

(e) Threshold result at needlet scale $j = 4$

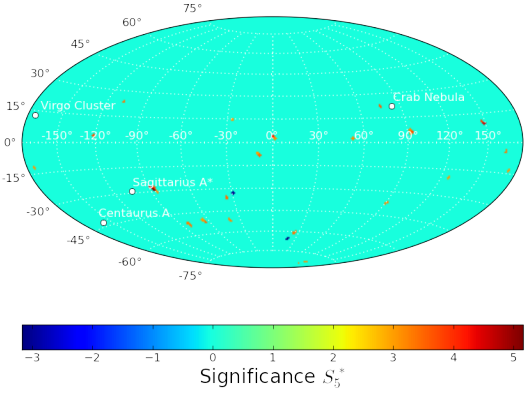

(f) Threshold result at needlet scale $j = 5$

Figure 6.15: The threshold results S^*_{jk} of the needlet scale $j = 0, 1, 2$ show no significant regions and in the threshold results S^*_{jk} of needlet scales $j = 3, 4, 5$ no structures are visible.

compatible with isotropy very good. This data set is compatible with 46.72% of the 10000 isotropy MC data sets. So no clear evidence of anisotropy was found.

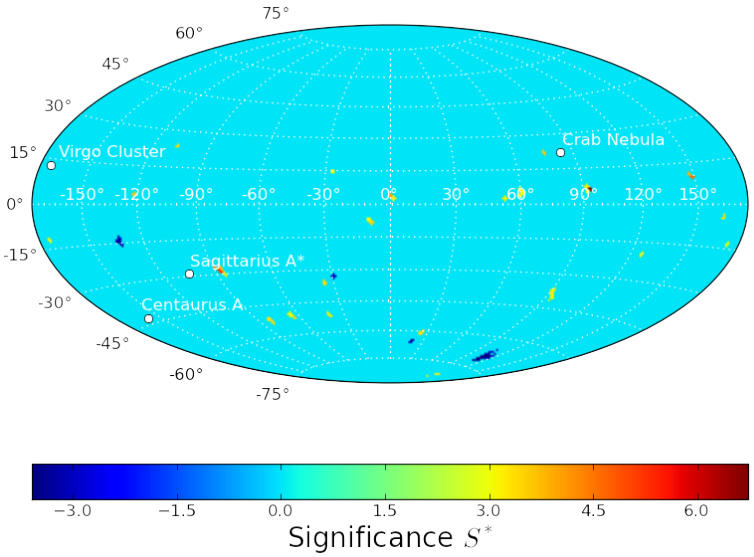

Figure 6.16: Combined threshold result S^* from the data with the corrected energy estimator and an additional minimal energy cut of 10 EeV. No significant regions were found.

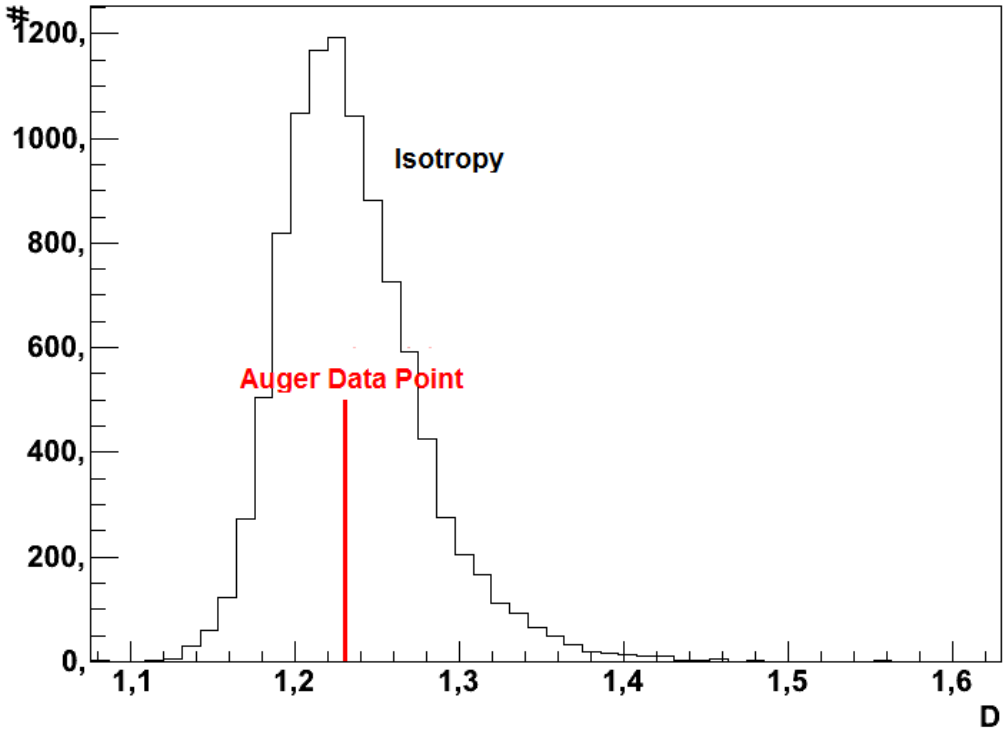

Figure 6.17: Global significance value $D = 1.215$ of the combined threshold result S^* in comparison to the D value of 10000 isotropic Monte Carlo data set. This data set is compatible with 46.72% of the 10000 isotropy MC data sets. So no clear evidence of anisotropy was found.

7. Summary and outlook

The wavelet analysis with the needlet was successfully applied to data of the arrival directions of ultra high energy cosmic rays. It was shown, that the needlet is capable to perform a multiscale analysis on an event based binned skymap. The methods were tested on Monte Carlo samples. It was shown, that the needlet analysis is capable of performing anisotropy analyses. A MC data set of an ideal fullsky detector was analyzed as well as MC data sets with the weighted exposure of the Pierre Auger Observatory. The needlet analysis described in this thesis is able to search for large scale structures, which was shown based on an astrophysical catalog, as well as point sources, which was shown with an arbitrary point source distribution.

The resulting power amplitude β_{jk} of the needlet analysis was successfully transformed into a significance value S_{jk} for every needlet scale j to make it comparable for further analysis. The threshold method S^*_{jk} was introduced and applied to the needlet results to filter for significant structures and it was successfully tested on the Monte Carlo test samples. The combined threshold results S^*_k of each test sample showed, that the needlet analysis has great potential in reconstructing the original source density distribution in the various Monte Carlo simulations. To determine the magnitude of an anisotropy signal found in the combined threshold signal S^*_k of the tested data sample a global significance value D was introduced. It was shown, that the value D can determinate successfully the probability to be compatible with isotropy.

It was shown that the needlet analysis compared to a simple multipole analysis has a great advantage in finding the location of local features and anisotropy.

After the successful test of the needlet analysis on Monte Carlo data sets the analysis was applied to the SD data measured by the Pierre Auger Observatory. The energy estimator was corrected for local effects induced by the atmospheric conditions and the geomagnetic field of the Earth. The needlet analysis described in this thesis was successfully applied to the arrival directions of the air shower data measured by the Pierre Auger Observatory and the global significance value D was computed. Three data sets were analyzed. A uncorrected data sample, a corrected data sample and a corrected data sample with a 10 EeV energy cut. All data sets are compatible with isotropy. Therefore, no significant large scale structures or point sources were identified.

The data set with the uncorrected energy estimator is clearly compatible with 92.52% of the isotropic MC data sets. So there was no significant anisotropy found. The probability for data set with the corrected energy estimator to be compatible with the

isotropic scenario was calculated to 1.72%, whereas the data set with the corrected energy estimator and an additional 10 EeV minimal energy cut is clearly compatible with 46.72% of the isotropic MC data set is very interesting. It could be a sign for some low energy effects. This needs further investigation.

It is also possible to perform a needlet analysis on an event based skymap, with a much smaller number of events, for example only the 100 highest energy particles, however this analysis will be different from the one performed in this thesis, due to the limited statistic. This needs also further investigation.

It was shown, that the this analysis works on every cosmic ray data sample, so this analysis could also be useful in gamma astronomy, as well as in neutrino detectors.

A. Appendix

A.1 List of abbreviations

AERA	Auger Engineering Radio Array
AGN	Active Galactic Nucleus
AMIGA	Auger Muon detectors and Infill for the Ground Array
CMB	Cosmic Microwave Background
DFT	Discrete Fourier Transform
EAS	Extensive Air Shower
FD	Fluorescence Detector
FFT	Fast Fourier Transform
GPS	Global Positioning System
GRB	Gamma Ray Burst
GZK-cutoff	Greisen-Zatsepin-Kuzmin-cutoff
HEALPIX	Hierarchical Equal Area iso-Latitude Pixelization of Sphere
HEAT	High Elevated Auger Telescopes
iFFT	inverse Fast Fourier Transform
IRAS	Infrared Astronomical Satellite
PAO	Pierre Auger Observatory
PMT	Photomultiplier Tube
SD	Surface Detector
UHECR	Ultra High Energy Cosmic Ray

A.2 Needlet kernel function

Underlying formulae of the needlet kernel function b taken from [MPB$^+$07]:

$$f(t) := \begin{cases} exp(-\frac{1}{1-t^2}) & -1 \leq t \leq 1 \\ 0 & \text{otherwise} \end{cases} . \tag{A.1}$$

$$\psi(u) := \frac{\int_{-1}^{u} f(t)dt}{\int_{-1}^{1} f(t)dt} . \tag{A.2}$$

$$\phi(t,B) := \begin{cases} 1 & \text{if } 0 \leq t \leq \frac{1}{B} \\ \psi(1 - \frac{2B}{B-1}(t - \frac{1}{B})) & \text{if } \frac{1}{B} \leq t \leq 1 \\ 0 & \text{if } t > 1 \end{cases} . \tag{A.3}$$

$$b^2(\xi,B) := \phi\left(\frac{\xi}{B}, B\right) - \phi(\xi,B) . \tag{A.4}$$

Only the positive root is kept:

$$b(\xi,B) := \left(\phi\left(\frac{\xi}{B}, B\right) - \phi(\xi,B)\right)^{\frac{1}{2}} \geq 0 . \tag{A.5}$$

Bibliography

[AEM+39] Pierre Auger, P. Ehrenfest, R. Maze, J. Daudin, and Robley A. Fréon. Extensive cosmic-ray showers. *Rev. Mod. Phys.*, 11(3-4):288–291, Jul 1939.

[All75] O. C. Allkofer. Introduction to cosmic radiation. *NASA STI/Recon Technical Report A*, 75:46929–+, 1975.

[AP08] J. Aberham and Pierre Auger Collaboration. Observation of the suppression of the flux of cosmic rays above 4×10^{19} eV. *Physical Review Letter*, 101:061101–+, Aug 2008.

[AP09] J. Aberham and Pierre Auger Collaboration. Atmospheric effects on extensive air showers observed with the Surface Detector of the Pierre Auger Observatory. *Astroparticle Physics*, 32(10):89–99, 2009.

[AP10] J. Aberham and Pierre Auger Collaboration. The Fluorescence Detector of the Pierre Auger Observatory. *Nucl. Instr. Meth.*, A620:227–251, 2010.

[ASP07] J. Aberham, Gregory Snow, and Pierre Auger Collaboration. Correlation of the Highest-Energy Cosmic Rays with Nearby Extragalactic Objects. *Science*, 318:938–943, Nov 2007.

[BEH09] J. Blümer, R. Engel, and J. R. Hörandel. Cosmic rays from the knee to the highest energies. *Progress in Particle and Nuclear Physics*, 63:293–338, 2009.

[Bré02] Pierre Brémaud. *Mathematical principles of signal processing: Fourier and wavelet analysis*. Springer, 2002.

[CSMG+01] L. Cayon, J. L. Sanz, E. Martinez-Gonzalez, A. J. Banday, F. Argueso, J. E. Gallegos, K. M. Gorski, and G. Hinshaw. Spherical mexican hat wavelet: an application to detect non-gaussianity in the cobe-dmr maps. *MON.NOT.ROY.ASTRON.SOC.*, 326:1243, 2001.

[Dem09] Hans Dembinski. *Measurement of the flux of ultra high energy cosmic ray flux using data from very inclined air showers at the Pierre Auger Observatory*. PhD thesis, RWTH Aachen University, 2009.

[DNW05] J. Knapp D. Newton and A. Watson. The Optimum Ground Parameter, $S(r_{opt})$. *GAP-Note 2005-013*, 2005. internal report, not for public display.

[Fer49] Enrico Fermi. On the Origin of the Cosmic Radiation. *Phys. Rev.*, 75(8):1169–1174, Apr 1949.

[Gri11] Marius Grigat. *Large Scale Anisotropy Studies of Ultra High Energy Cosmic Rays Using Data Taken with the Surface Detector of the Pierre Auger Observatory*. PhD thesis, RWTH Aachen University, 2011.

[Han] William Hanlon. Website. `http://www.physics.utah.edu/~whanlon/spectrum.html`, visited 08.11.2011.

[Hes12] Victor Franz Hess. Über Beobachtungen der durchdringenden Strahlung bei sieben Freiballonfahrten. *Z. Phys.*, 13:1084, 1912.

[HMHH71] A. M. Hillas, D. J. Marsden, J. D. Hollows, and H. W. Hunter. Measurement of Primary Energy of Air Showers in the Presence of Fluctuations. In *International Cosmic Ray Conference*, volume 3 of *International Cosmic Ray Conference*, pages 1001–+, 1971.

[Lab] Laboratoire de Physique Subatomique et de Cosmologie Grenoble. Website. `http://lpsc.in2p3.fr/DRAC/corinne/Communication/CB-images/uhecr/HillasPlot.jpg`, visited 09.18.2011.

[Lon11] Malcolm S. Longhair. *High Energy Astrophysics*. Cambrige University Press, third edition, 2011.

[MPB+07] D. Marinucci, D. Pietrobon, A. Balbi, P. Baldi, P. Cabella, G. Kerkyacharian, P. Natoli, D. Picard, and N. Vittorio. Spherical Needlets for CMB Data Analysis. *MONTHLY NOTICES OF THE ROYAL ASTRONOMICAL SOCIETY*, 383:539, 2007.

[MTKM07] G. Medina-Tanco and A.G.O. Krone-Martins. The Galactic Center as a point source of neutrons at EeV energies. *Nuclear Physics B - Proceedings Supplements*, 165(0):280 – 286, 2007.

[NAS] NASA Jet Propulsion Laboratory. Website. `http://healpix.jpl.nasa.gov`, visited 07.18.2011.

[PAB+08] Davide Pietrobon, Alexandre Amblard, Amedeo Balbi, Paolo Cabella, Asantha Cooray, and Domenico Marinucci. Needlet detection of features in the WMAP CMB sky and the impact on anisotropies and hemispherical asymmetries. *Phys. Rev. D*, 78(10):103504, Nov 2008.

[Piea] Pierre Auger Collaboration. Website. `http://www.auger.org.ar/survey/Ozi/sd-array-full-1673-SD-20041116.jpg`, visited 07.15.2011.

[Pieb] Pierre Auger Collaboration. Website. `http://www.auger.de/images/AugerEvent_200718601091.gif`, visited 07.15.2011.

[Piec] Pierre Auger Collaboration. Website. `http://www.auger.org/media/images/quadriple.jpg`, visited 08.11.2011.

[Plu] Matthias Plum. Picture taken in March 2011.

[PP03] P. Privitera and Pierre Auger Collaboration. The Angular Reconstruction and Angular Resolution of Air Showers Detected at the Auger Observatory. *Proc. ICRC 2003*, 2003.

[RBRD08] Frank M. Rieger, Valentí Bosch-Ramon, and Peter Duffy. Fermi acceleration in astrophysical jets. In Josep M. Paredes, Olaf Reimer, and Diego F. Torres, editors, *The Multi-Messenger Approach to High-Energy Gamma-Ray Sources*, pages 119–125. Springer Netherlands, 2008.

[RS98] M. V. S. Rao and B. V. Streekantan. *Extensive Air Showers*. World Scientific Publishing Co. Pte. Ltd., 1998.

[SSM+00] W. Saunders, W. J. Sutherland, S. J. Maddox, O. Keeble, S. J. Oliver, M. Rowan-Robinson, R. G. McMahon, G. P. Efstathiou, H. Tadros, S. D. M. White, C. S. Frenk, A. Carramiñana, and M. R. S. Hawkins. The PSCz catalogue. *MONTHLY NOTICES OF THE ROYAL ASTRONOMICAL SOCIETY*, 317:55–63, September 2000.

[TC98] Christopher Torrence and Gilbert P. Compo. A Practical Guide to Wavelet Analysis. *Bulletin of the American Meteorological Society*, 79:61–78, 1998.

List of Figures

2.1 Cosmic ray energy spectrum measured by various experiments [Han]. The flux of the cosmic rays against the energy of the particles shows the power law behavior of the spectrum. The positions of the features 'knee' and 'ankle' are shown. At these points the value of the power law index changes. 5

2.2 Hillas Plot of astrophysical objects in which cosmic rays could be accelerated [Lab]. The magnetic field strength against the size of the source region is shown. 6

2.3 Left: Schematic view of the extensive air shower components. Right: Geometrical shape of an extensive air shower [All75]. 7

3.1 The Pierre Auger Observatory[Piea]. The picture shows the surface detector array (small dots) over an area of 3000 km^2 and four fluorescence detector buildings located around the array. 9

3.2 Scheme of a SD station [Dem09]. The power is provided by a solar panel and a battery system. The data is transferred via a wireless communication system. Each station is filled with 10 tons of pure water and equipped with three PMTs. The inner surface of the station is encased with a reflecting layer called Tyvek. The time information for the PMT signals is provided by a GPS receiver. 10

3.3 Picture of a surface detector station [Plu]. 11

3.4 Event display of a SD event, where the color code contains the timing information and the size of the station corresponds to the PMT signal strength [Pieb]. 11

3.5 Schematic of the angular reconstruction of SD assuming a plane shower front [Gri11]. 12

3.6 Schema of the fluorescence detector [AP10] 13

3.7 A multi fluorescence detector event, seen by all four FD telescopes and SD reconstruction [Piec]. 14

4.1 1-dim analysis example with a Gaussian signal $S(x)$ in red and the Mexican hat wavelet $\psi_{MH}(x)$ in blue. 16

4.2 FFT of Gaussian signal $X(\nu)$ in red, the Mexican hat wavelet $\psi(\nu)$ in blue and the result of the convolution $P(\nu)$ in magenta. 17

4.3 The signal is reconstructed on the correct position. 17

4.4 Flow diagram of spherical wavelet analysis. 18

4.5 Healpix binning structure [NAS]. 19

4.6 Healpix pixel numeration [NAS]. 19

4.7 Needlet kernel function $b(l, B^{-j})$ against the multipole moment l for various needlet width B with a fixed needlet scale $j = 2$. 20

4.8 Needlet kernel function $b(l, B^{-j})$ against the multipole moment l for various scales j with a fixed needlet width $B = 2.0$. 21

4.9 Needlet shape for the scale $j = 3$ and $j = 4$ with a needlet width $B = 2.0$. 22

4.10 Needlet for the scale $j = 2$ in Hammer-Aitoff projection. This shows the spherical symmetry the projection view is centered at the pole. . 22

5.1 Signal density distribution for a point source. 26

5.2 Monte Carlo signal skymap with 200 events. 26

5.3 Event-based signal skymap with added isotropic noise with 30000 events in total. 27

5.4 Power amplitude β_j of the needlet analysis for a fullsky test data set for different scales j. The point source is visible in the scales $j = 1, 2, 3$ by eye, whereas in the scales $j = 0, 4, 5$ only fluctuations are visible. . 28

5.5 Power amplitude β_{jk} distribution for one random pixel k in case of isotropy for needlet scale $j = 2$ and a Gauss fit in red to determine the mean $< \beta_{jk} >$ and the standard deviation σ_{jk}. 29

5.6 Declination vs. power amplitude β_{jk} fluctuations in case of isotropy for needlet scale $j = 2$ with fullsky exposure. The spreading of the power amplitude β_{jk} is independent of the declination in case of an ideal detector. 30

5.7 Threshold results S_j^* for the fullsky test data set for various scales j. After the threshold cut most of the fluctuations are filtered out and in the scales $j = 1, 2, 3$ the point source is clearly visible. Scale $j = 0$ is now completely empty and in the scales $j = 4, 5$ only a few pixels are kept. 31

5.8 Original source density (above) in comparison to the combined threshold map S_k^*(below) for the fullsky test data set. The combined threshold map reflects the correct source distribution. 32

5.9 Global significance value D of the combined threshold result ($D = 1.5253$) from the fullsky test compared to the values of 10000 isotropic Monte Carlo data sets. The probability to be compatible with isotropy is clearly below 0.0001%. 33

5.10 Angular power spectrum C_l for 10000 isotropic Monte Carlo data sets. In this plot the z value for each multipole moment l is renormalized to an integral value of 1, so that the probability for C_l is shown. . . . 34

5.11 Log-Likelihood values L for 10000 isotropic skymaps in comparison to the Log-Likelihood value of the fullsky test data set. 35

5.12 Partial and non uniform sky coverage of Pierre Auger Observatory in equatorial coordinates. 36

5.13 Power amplitude β_{jk} fluctuations vs. declination in case of isotropy for needlet scale $j = 2$ with Pierre Auger Observatory exposure. . . . 37

5.14 The source map based on the PSCz catalog with 12879 point sources. 38

5.15 The source density distribution based on the PSCz catalog smeared with a Gaussian and convoluted with the Auger exposure. 39

5.16 Event-based skymap based on the PSCz catalog with additional isotropic noise. 39

5.17 Power amplitude β_j of the needlet analysis for a PSCz test sample for different scales j. There is no clear structure visible, so further filtering needs to be done. 40

5.18 Threshold results S_j^* for a PSCz test sample for various scales j. After the threshold cut most of the fluctuations are filtered out and structures become visible. 41

5.19 Comparison of original source density distribution (top) and the combined threshold result S^* of the needlet scale $j = [0, 5]$ (bottom) shows strong similarity. 42

5.20 Global significance value D for PSCz based ($D = 1.72$) skymap shows that the probability to be compatible with 10000 isotropic Monte Carlo data sets is below 0.0001%. 43

5.21 Artificial point source distribution used as probability density. 44

5.22 Event-based skymap based on an artificial point source distribution with additional isotropic noise (total 30000 events). 45

5.23 Needlet analysis results β_j of artificial point source distribution for various scales j. Further filtering is needed to find the other point sources. 46

5.24 Threshold results S_j^* for the artificial point source sample for various scales j. After the threshold cut most of the fluctuations are filtered out and the point sources become visible. 47

5.25 Comparison of original source density distribution (top) and the combined threshold result S^* of the needlet scales $j = [0, 5]$ (bottom) shows that all four point sources are found in the correct regions. . . 48

5.26 Global significance value D for the point source Monte Carlo sample ($D = 1.553$) shows, that the probability to be compatible with the 10000 isotropic Monte Carlo data sets is below 0.0001%. 49

6.1 Relative trigger-rate at the PAO from the correction for atmospheric parameters against the right ascension. 52

6.2 Separation of charged air shower particles in the Earth's magnetic field B: Muons $\mu^{\pm}$ are deflected by δx on average according to their respective charge, the originally circular footprint of the lateral particle densities in the shower front becomes distorted. [Gri11] 53

6.3 Arrival directions of the Auger data set with the uncorrected energy estimator are plotted in the Healpix scheme. The number of events is 43383. 55

6.4 The power amplitude β_j of the needlet analysis on the arrival directions of the UHECRs of the Pierre Auger Observatory is shown for different needlet scales j. 56

6.5 The threshold results S^*_{jk} are shown for the needlet analysis result. There are a large scale structures in the needlet scale $j = 0$, that are marked as significant and a structure similar to a point source in the needlet scale $j = 2$ at the position of the Crab Nebula. In the needlet scale $j = 1$ there is a large structure at the south pole visible and also 2 regions with under fluctuation. In the needlet scale $j = 3$ there is a small structure in the region of the Virgo Cluster and a small under fluctuation. 58

6.6 Combined threshold result S^* shows the features of the each needlet scale j, but no strong point source or large scale structures. 59

6.7 Global significance value $D = 1.158$ of the combined threshold result S^* in comparison to the D value of 10000 isotropic Monte Carlo data set. This data set is compatible with 92.52% of the 10000 isotropic MC data sets. So no clear evidence of anisotropy was found. 59

6.8 Arrival directions of the Auger data set with the corrected energy estimator are plotted in the Healpix scheme. The number of events is 38340. 60

6.9 The power amplitude β_j of the needlet analysis on the arrival directions of the UHECRs of the Pierre Auger Observatory is shown for different needlet scales j. The results needed more filtering to determine the significant structures. 61

6.10 The threshold results S^*_{jk} of the needlet scale $j = 1$ shows a large structure in the South pole region and also a under fluctuation. The threshold results S^*_{jk} of the needlet scale $j = 2$ shows 3 structures and a under fluctuation. The significant structures are in the South pole region, near the Crab Nebula and the other is near the equator. There are no significant regions in the needlet scale $j = 0$ and in the threshold results S^*_{jk} of needlet scales $j = 3, 4, 5$ no structures are visible. 63

6.11 Combined threshold result S^* from the data with the corrected energy estimator. The structures in the south pole region and at the equator can be a hint for an excess in the cosmic ray arrival directions. 64

6.12 Significance value D of the threshold result ($D = 1.293$) from the data compared to the D value of 10000 isotropic Monte Carlo data sets. The probability of this data set to be compatible with isotropy is 1.72%. 64

6.13 Arrival directions of the Auger data set with the uncorrected energy estimator are plotted in the Healpix scheme. The number of events is 4919. 65

6.14 The power amplitudes β_j of the needlet analysis on the arrival directions of the UHECRs of the Pierre Auger Observatory are shown for different needlet scales j. 66

6.15 The threshold results S^*_{jk} of the needlet scale $j = 0, 1, 2$ show no significant regions and in the threshold results S^*_{jk} of needlet scales $j = 3, 4, 5$ no structures are visible. 67

6.16 Combined threshold result S^* from the data with the corrected energy estimator and an additional minimal energy cut of 10 EeV. No significant regions were found. 68

6.17 Global significance value $D = 1.215$ of the combined threshold result S^* in comparison to the D value of 10000 isotropic Monte Carlo data set. This data set is compatible with 46.72% of the 10000 isotropy MC data sets. So no clear evidence of anisotropy was found. 68

List of Tables

2.1 Muon production and decay of charged mesons. 8

4.1 Healpix parameters 23

4.2 Needlet parameters 23

5.1 Fullsky point source parameters 25

5.2 Comparison of the set and the reconstructed position of the greatest S_k^* value of the point source center. 30

5.3 Point source parameters for the artificial point source distribution. . . 44

5.4 Comparison of set point source positions with the reconstructed positions. 49

6.1 Auger data selection with the uncorrected energy estimator. 54

6.2 Auger data selection with the correction of the energy estimator. . . . 54

6.3 Auger data selection with the correction of the energy estimator with an additional 10 EeV minimal energy cut. 54

Acknowledgements

I would like to thank Prof. Dr. Thomas Hebbeker, who offered me this interesting topic for my diploma thesis and gave me the chance to work for the Pierre Auger Observatory. His knowledge and his support were motivating and made this year a great time. I would also like to thank Prof. Dr. Martin Erdmann, who agreed to review this thesis as second referee.
Special thanks to Marius Grigat and Stephan Schulte. You helped me very much with the creation of this physics analysis. Thanks for the discussions and advices. Furthermore, I would like to thank all collaboration members I met and had fruitful discussions with, e.g. during the collaboration meetings in Argentina. Also thanks to all the people of the Auger group from the Physics Institute IIIA of the RWTH Aachen.
Special thanks to Larissa, for your incredible patience and helpful advices. Finally, I would like to thank my parents and my whole family, who gave me the opportunity to study physics.

Erklärung

Hiermit versichere ich, dass ich diese Arbeit einschließlich beigefügter Zeichnungen, Darstellungen und Tabellen selbstständig angefertigt und keine anderen als die angegebenen Hilfsmittel und Quellen verwendet habe. Alle Stellen, die dem Wortlaut oder dem Sinn nach anderen Werken entnommen sind, habe ich in jedem einzelnen Fall unter genauer Angabe der Quelle deutlich als Entlehnung kenntlich gemacht.

Aachen, den 04.10.2011

Matthias Plum